# A Holistic View of Unstable Dark Matter: Spectral and Anisotropy Signatures in Astrophysical Backgrounds

**Dissertation**

**zur Erlangung des Doktorgrades**

**des Department Physik**

**der Universität Hamburg**

**vorgelegt von**

**Le Zhang**

**aus Shaanxi, China**

**Hamburg**

**2010**

| | |
|---|---|
| Gutachter der Dissertation | Prof. Dr. G. Sigl |
| | Prof. Dr. D. Horns |
| Gutachter der Disputation: | Prof. Dr. G. Sigl |
| | Prof. Dr. W. Buchmüller |
| Datum der Disputation: | 26.11.2010 |
| Vorsitzender des Prüfungsausschusses: | Prof. Dr. C. Hagner |
| Vorsitzender des Promotionsausschusses: | Prof. Dr. J. Bartels |
| Dekan der Fachbereichs Physik: | Prof. Dr. H. Graener |

# Zusammenfassung

Die Natur der dunklen Materie ist eines der wichtigsten Probleme sowohl der Elementarteilchen- als auch der Astrophysik. Sollte dunkle Materie zerfallen oder annihilieren, könnten diese Prozesse in der Astrophysik gemessene diffuse Strahlungshintergründe verändern. In dieser Arbeit stellen wir eine neue, allgemeinere Methode vor, um Schranken für beliebige Modelle dunkler Materie zu berechnen. Für zerfallenden dunkle Materie können Schranken für Masse und Lebensdauer berechnet indem das Zerfallsspektrum eines gegebenen Modells mit einer response Funktion gefaltet wird. Wir leiten die response Funktion aus Himmelsdurchmusterungen im Radiobereich, aus Gammastrahlungs-Messungen des Fermi-LAT Satelliten und aus den vom PAMELA Satellitenexperiment gemessenen Positron Flüssen ab und wenden sie auf einige spezielle Modelle dunkler Materie an. Außerdem betrachten wir den Einfluss astrophysikalischer Unsicherheiten auf die response Funktion, insbesondere Unsicherheiten der Propagations-Modelle und der räumlichen Verteilung der dunkler Materie.

Desweiteren analysieren wir die Anisotropie der im Radio- und Gamma-Strahlungsbereich gemessenen Himmelskarten im Hinblick auf mögliche Signaturen annihilierender dunkler Materie. Dazu berechnen wir winkelabhängige Leistungsspektren der von Annihilation dunkler Materie in Elektron-Positron Paare erzeugten Synchrotronstrahlung. Wir vergleichen diese Leistungsspektren mit der Anisotropie astrophysikalischer und kosmologischer Radio-Hintergründe von normalen und Radio-Galaxien und von Akkretions-Schocks in Galaxienhaufen, sowie mit der Anisotropie des kosmischen Mikrowellenhintergrundes und des galaktischen Vordergrunds. Zusätzlich haben wir ein numerisches Programmpaket entwickelt, um die Gammastrahlungs-Emission dieser im galaktischen Halo und in sub-Halos der dunklen Materie mit Masse bis hinab zu $10^{-6} M_{\odot}$ diffundierenden Elektronen und Positronen zu berechnen. Wir zeigen daß im Gegensatz zum von Fermi-LAT beobachteten winkelabhängigen Leistungsspektrum das von der inversen Compton-Streuung verursachte Leistungsspektrum unterhalb einer von der Diffusionslänge der Elektronen und Positronen bestimmten Skala exponentiell unterdrückt ist.

# Abstract

The nature of dark matter is one of the key outstanding problems in both particle and astrophysics. If dark matter decays or annihilates into electrons and positrons, it can affect diffuse radiation backgrounds observed in astrophysics. In this thesis, we propose a new, more general analysis of constraints on dark matter models. For any decaying dark matter model, constraints on mass and lifetime can be obtained by folding the specific dark matter decay spectrum with a response function. We derive these response functions from full-sky radio surveys and Fermi-LAT gamma-ray observations as well as from the local positron fluxes mesured by the PAMELA satellite experiment and apply them to place constraints on some specific dark matter decay models. We also discuss the influence of astrophysical uncertainties on the response function, such as the uncertainties from propagation models and from the spatial distribution of the dark matter.

Moreover, an anisotropy analysis of full-sky emission gamma-ray and radio maps is performed to identify possible signatures of annihilating dark matter. We calculate angular power spectra of the cosmological background of synchrotron emission from dark matter annihilations into electron positron pairs. We compare the power spectra with the anisotropy of astrophysical and cosmological radio backgrounds, from normal galaxies, radio-galaxies, galaxy cluster accretion shocks, the cosmic microwave background and Galactic foregrounds. In addition, we develop a numerical tool to compute gamma-ray emission from such electrons and positrons diffusing in the smooth host halo and in substructure halos with masses down to $10^{-6} M_{\odot}$. We show that, unlike the total gamma-ray angular power spectrum observed by Fermi-LAT, the angular power spectrum from the inverse Compton scattering is exponentially suppressed below an angular scale determined by the diffusion length of electrons and positrons.

*To my parents ...*

# Contents

# List of Figures

# List of Tables

# Chapter 1

# Introduction

In the last decades, the existence of nonbaryonic dark matter in modern cosmology is strongly supported by several independent signatures [1], including the cosmic microwave background (CMB), gravitational lensing and large scale structure (LSS) surveys. However, the nature of dark matter remains a mystery – we only know that dark matter does not participate in the electromagnetic or strong interactions and that it has behaved as a non-relativistic fluid during the formation of the large scale structure of the Universe. Many extensions of the Standard Model of particle physics generally predict new dynamics between the electroweak and the Planck scales together with a number of new particles, sometimes with the required properties to be dark matter. To reproduce the correct relic density, it is naturally assumed that dark matter is composed of weakly interacting massive particles (WIMPs) such as the supersymmetric neutralino, one of the most popular candidates [2]. There also exists a number of interesting and theoretically well motivated dark matter models that predict the decay of dark matter on cosmological time scales, which are typically required to be not in conflict with current observational limits [3, 4, 5].

Dark matter can be detected directly in dedicated experiments searching for nuclear recoils from the scattering of dark matter particles, or produced in particle accelerators such as the LHC. It can also reveal its existence indirectly [1]. Dark matter decays or annihilations can give rise to significant fluxes of gamma-rays, electrons, positrons, neutrinos, and even some antimatter such as anti-protons and positrons. The energies of the secondary particles that can reach up to the dark matter particle mass can be of order a few hundred GeV. Secondary electrons and positrons can annihilate and give rise to a 511 keV line emission, and they emit synchrotron radiation in the magnetic fields of galaxies which can be detected in the radio band. These electrons and positrons also produce gamma-rays through inverse Compton scattering (ICS) off the low energy background photons in an interstellar radiation field (ISRF) and through bremsstrahlung emissions due to the interaction with an ionized interstellar medium (ISM). Therefore, cosmic-ray and gamma-ray detectors, radio telescopes and even neutrino telescopes, can be used for indirect dark matter detection as well.

Interestingly, multiple experiments have recently announced results which have

been interpreted as possible products of dark matter annihilation or decay. In particular, in July 2008, the PAMELA (Payload for Antimatter Exploration and Light-nuclei Astrophysics) experiment reported an unexpected excess in the positron fraction above 10 GeV [6], but antiproton measurements are consistent very well with the expected values [7]. Soon after the publication of the PAMELA data, in November 2008, the ATIC balloon experiment [8] revealed a sharp bump between 300-800 GeV in the cosmic ray $e^+e^-$ spectrum, with a maximum of 600 GeV. However, the Fermi-LAT (Large Area Telescope) also published relevant data which does not confirm the ATIC excess [9]. At the same time, the HESS collaboration [10, 11] reported a power-law spectrum in the $e^+e^-$ spectrum at energies larger than 340 GeV up to several TeV, in agreement with the Fermi-LAT result.

Apart from cosmic-ray data, in the radio band, the WMAP data revealed an excess of microwave emission at the Galactic central region, which can be interpreted as an additional source of electrons and positrons with a hard spectral index [12]. Similarly, a diffuse inverse Compton signal in the inner Galaxy with a similar spatial morphology to the microwave haze was pointed out by the Fermi-LAT [13]. Together, all these observations imply that dark matter decay or annihilation can act as such additional source of excesses, although ordinary astrophysical sources such as pulsars [14, 15, 16, 17] are more plausible. Currently, indirect detection efforts are being developed very rapidly, and we can imagine that in the near future, more accurate measurements will provide many exciting results for indirect detection of dark matter.

This thesis presents a study of indirect searches of dark matter. An overview of dark matter is given in chapter 2. Chapter 3 shortly describes the astronomical observations. Chapter 4 discusses the cosmic-ray propagation in our Galaxy. Chapter 5 focuses on constraining decaying dark matter by folding universal response functions with a specific dark matter model. We develop these response functions by current radio and gamma-ray data as well as the observed positron fluxes. In chapter 6, we perform a statistical analysis of the full-sky radio and gamma-ray emission maps, pointing out unique features in the anisotropy power spectra resulting from dark matter annihilation. Finally we conclude and give an outlook in chapter 7. This thesis is mostly based on the papers [18, 19, 20, 21] in which I was the main author. The first three papers were published in refereed journals and the last one is submitted for publication.

# Chapter 2

# Properties of Dark Matter

In modern cosmology, the presence of nonbaryonic dark matter is strongly supported by many astronomical and cosmological observations. However, the property of dark matter particle remains a mystery after decades of research. As of today, only the gravitational influence of dark matter on normal visible matter can be detected.

This chapter first gives a short introduction to standard cosmology and shows the most convincing evidence for dark matter. Then what follows is a short description of dark matter halo models in terms of theoretical predictions and recent N-body simulations. This chapter ends with a discussion on dark matter candidates.

## 2.1 Standard Cosmology

The standard cosmology was built after the discovery of the Hubble's law in the early 20th century and is supported by all sorts of cosmological observations. The Einstein's equation of General Relativity can describe accurately the observed Universe and is a foundation stone for any cosmological study (for a good introduction to standard cosmology see Refs [22, 23, 24, 25]). The Einstein's gravitational field equation reads

$$R_{\mu\nu} - \frac{1}{2} g_{\mu\nu} R = -8\pi G T_{\mu\nu} + \Lambda g_{\mu\nu} \,, \tag{2.1}$$

where $R_{\mu\nu}$ and R are, respectively, the Ricci tensor and scalar (obtained by contraction of the Riemann curvature tensor). $g_{\mu\nu}$ is the metric tensor, $G$ is Newtons constant, $T_{\mu\nu}$ is the energy-momentum tensor, and $\Lambda$ is the cosmological constant. Assuming an isotopic and homogeneous Universe (the cosmological principle), the Hubble parameter $H$, which often describes the evolution of the Universe, obeys the Friedmann equation:

$$H^2 \equiv \frac{\dot{a}}{a} = \frac{8\pi G\rho + \Lambda}{3} - \frac{k}{a^2} \,, \tag{2.2}$$

where an unconstrained function $a(t)$ is the scale factor and $\rho$ is the total average energy density of the Universe. Here the constant $k = -1, 0, +1$ depends on if a

negative, flat or positive curvature has been respectively adopted for the metric of the Universe.

The energy density $\rho$ is often expressed in fractions of the *critical density* $\rho_c$, introducing the parameter $\Omega = \rho/\rho_c$ with

$$\rho_c = \frac{3H^2}{8\pi G}\,. \tag{2.3}$$

Here $\rho$ is usually separated into a baryonic component $\Omega_b$ (i.e. ordinary matter), cold dark matter $\Omega_{CDM}$ and a radiation/relativistic particles component $\Omega_r$. In general, the various $\Omega_i$ evolve with time differently, depending on the equation of state of the component. Similarly, the cosmological $\Lambda$ and the curvature $k$ can be often expressed with $\Omega_\Lambda \equiv \frac{\Lambda}{8\pi G\rho_c}$ and $\Omega_k \equiv \frac{-k}{\dot{a}^2}$. The constant term will not be diluted by an expanding Universe. Therefore, it will dominate the energy content of the Universe and accelerate the expansion at some point. Current observations, such as the Type-Ia supernovae [26], indicate that this has started to happen in the recent stage of the evolution of the Universe. The origin of this acceleration is another outstanding question in modern cosmology and particle physics.

A general expression for the Hubble expansion rate as function of redshift $z$ is given by the simple expression

$$H = H_0\sqrt{\Omega_{CDM}(1+z)^3 + \Omega_b(1+z)^3 + \Omega_r(1+z)^4 + \Omega_k(1+z)^2 + \Omega_\Lambda}\,. \tag{2.4}$$

The redshift $z$ is related to the scale factor as $z(t) + 1 = a(t_{obs})/a(t)$, where $a_{obs}$ denotes the scale factor today, and $H_0$ denotes the current Hubble expansion rate $H_0 \sim 70$km/s/Mpc. For standard cosmology, today the Universe is estimated to be 13.7 billion years old and almost flat $\Omega_k \sim 0$, and its energy budget is: $\Omega_\Lambda \sim 74\%$, $\Omega_{CDM} \sim 22\%$, $\Omega_b \sim 4\%$ and $\Omega_r \sim 0.005\%$ [27].

## 2.2 Gravitational Evidence of Dark Matter

In 1933, F. Zwicky [28] firstly inferred the existence of dark matter from the measurements of the velocity dispersion of galaxies in the Coma cluster. By using the virial theorem to the velocity dispersion, he found that a mass-to-light ratio largely exceeds the ratio in the solar system by two orders of magnitude, which means most of mass in cluster must be dominated by invisible matter. His suggestion of a missing *dark matter* component did not arouse much attention at that time until around 40 years later V. Rubin found the same situation by spectroscopical measurements of the rotation curves of stars in edge-on spiral galaxies. This again indicates that something other than the stellar population must contribute significantly to the mass of galaxies [29]. Today, most dynamical estimates [30, 31, 32] confirms both Zwicky's and Rubin's works, inferring a value $\Omega_{CDM} \sim 0.2 - 0.3$ on cluster scales, and the existence of dark matter is widely accepted. Also there are some other complementary measurements to determine the mass of a stellar cluster, such as by the

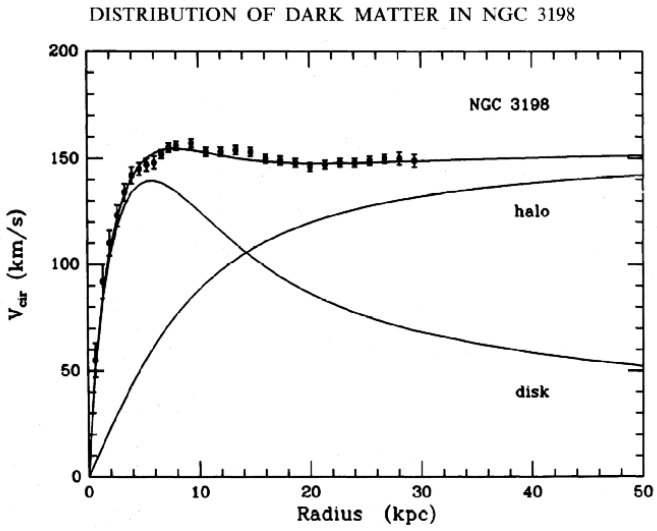


**Figure 2.1:** Rotation curve of NGC 3198 from Ref. [35]. The lines show an example of the ordinary contribution 'disk' and the dark matter contribution 'halo'.

weak gravitational lensing [33] and by studying the profile of X-ray emission that traces the distribution of hot emitting gas in rich clusters (for review see Ref. [34]).

Rotation curves by now are well measured by combining observations of 21-cm line with optical surface photometry. Observed rotation curves usually exhibit a characteristic flat behavior at large distances, i.e. out towards, and even far beyond, the edge of the visible disks (see a typical example in Fig. 2.1). In Newtonian dynamics, the gravitational force keeps the star in a galaxy in a circular orbit and the velocity at a galactic radius $r$ is given by $v(r) = \sqrt{GM(<r)/r}$, where $M(<r) \equiv 4\pi \int^r r'^2 \rho(r') dr'$ the mass within $r$, with a mass density given by $\rho(r')$. Usually, the observed stellar population density decreases exponentially with radius which would imply a constant mass distribution at large radii beyond the optical disk and hence a velocity rotation curve $v \propto 1/\sqrt{r}$ at large radii. However, the observed velocity curve is approximately constant at large distances from the galactic centre. This requires an halo with $M(r) \propto r$, or equivalently $\rho(r) \propto r^{-2}$. This cannot be interpreted as galactic gas and stars alone. Therefore we must introduce an additional dark matter component to explain the rotation curves of galaxies. In Fig. 2.1, we show an example [35] of an rotation curve for the galaxy NGC 3198 to illustrates the discussion above.

Recently, a strong evidence of dark matter comes from the Bullet cluster [36]. Due to the collision of two clusters (one of them has a characteristic bullet shape), the dissipationless stellar component and the fluid-like X-ray emitting plasma are spatially segregated (see Fig. 2.2). On the other hand, the analysis of gravitational weak lensing maps pointed out that the gravitational potential does not trace the baryonic mass component, but rather approximately traces the distribution of galaxies. This behavior cannot be easily explained by modified Newton dynamics [37, 38] and thus prove that the dominated component in the cluster is composed of unseen

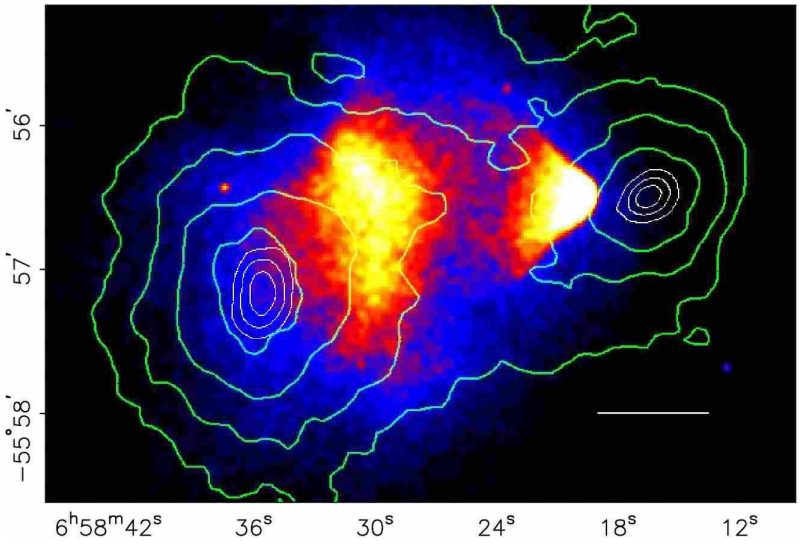


**Figure 2.2:** The observation of merging Bullet cluster (named after the shape to the right) from Ref. [36]. The contours show the distribution of gravitating mass as inferred from weak gravitational lensing. The observation of hot x-ray emitting gas which traces the distribution of intercluster medium is shown in red and the blue hues show the distribution of dark matter in the cluster.

matter.

Most cosmological observations, such as the CMB angular power spectrum, the LSS surveys and the Type-Ia supernovae distance measurements, can determine precisely the dark matter density. Type-Ia supernovae are regard as excellent standard candles for measuring distances in the Universe. The peak luminosity from supernova explosion is always about same. Thus, if the peak luminosity of a type-Ia supernova in a distant galaxy is measured, using the inverse square law, one can infer the distance of its parent galaxy. Combining with a determination of the redshifts $z$ of the observed supernovae, one can place constraints on the Hubble expansion rate $H(z)$, which in turn gives constraints on the cosmological parameters. Furthermore, dark matter plays an important role on both CMB anisotropies and on structure formation through its gravitational influence on ordinary matter. The process can be simply understood as follows.

After the inflation, matter density fluctuations are assumed to be scale invariant. During radiation-dominated era (i.e. when $\Omega_r$ is larger than the other densities), density perturbations can only grow until they enter the horizon of the causally connected Universe, $\sim 1/H$. Perturbations within the horizon will oscillate due to the radiation pressure and will not grow significantly. Thus, the amplitude of perturbations within horizon will be suppressed. As the horizon continues to increase, perturbations at all scales are prevented from growing. At the time of matter-radiation equality ($z \approx 3000$), the dark matter perturbations start to increase. Thus, there is a suppression of structures to a size smaller than the horizon of the Universe at matter-radiation equality. Today this corresponds to a suppression of structures

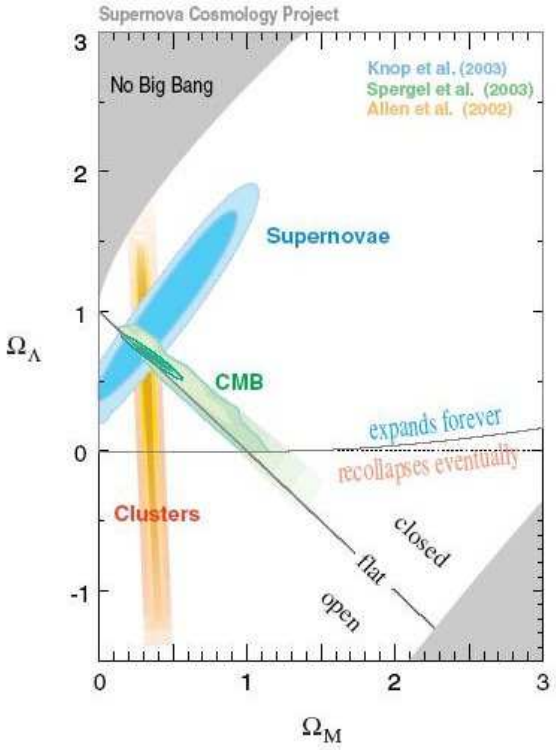


**Figure 2.3:** Combined constraints on cosmological densities $\Omega_\Lambda$ and $\Omega_m$, using supernovae, CMB and cluster abundance data. The flat Universe ($k = 0$) is shown with solid line (from Ref. [39]).

smaller than $\sim$ 1Gpc. However the radiation pressure due to Thomson scattering still resists the increase in baryon perturbations. After recombination ($z \approx 1100$) when the photons have decoupled from baryons, the baryonic matter rapidly fall into the previously formed gravitational potential wells of dark matter, so that photons, which prevent baryons from forming structure, do not have significant consequences on structure formation. At the same time, the patterns of acoustic oscillations, due to the struggle between gravity and radiation pressure in the photon-baryon fluid, are frozen into the CMB. Therefore, the amplitudes and the locations of acoustic peaks in CMB angular power spectrum and the quantity $\sigma_8$, the fractional root mean square fluctuation in density on a linear scale of $8h^{-1}$, can be used to determine the amount of dark matter by observations of clusters. Together with all the aforementioned measurements, the constrains on dark matter density are shown in Fig. 2.3.

When the perturbations have grown sufficiently, a small region might become substantially denser than the mean density of the Universe and at some point it will start to collapse and form gravitationally bound objects called the *halos*. The collapsed objects can be understood by the semi-analytical models from the linear growth theory of initial perturbations, which is only applicable for small enough perturbations ($\frac{\delta\rho}{\bar{\rho}} \ll 1$), as described by the Press-Schechter theory [40] and its

| model | $\alpha$ | $\beta$ | $\gamma$ |
|---|---|---|---|
| Kra | 2 | 3 | 0.4 |
| Iso | 2 | 2 | 0 |
| NFW | 1 | 3 | 1 |

**Table 2.1:** Some of widely used dark matter halo density profiles.

extension [41] with ellipsoidal collapse. However, the analytical description of collisions between dark matter halos is still a problem since the density perturbations can no longer be approximated by a random Gaussian field in a nonlinear regime. Instead the dynamics in nonlinear gravitational region can be best understood by N-body simulations which start from an initial condition (*e.g.* from the primordial power spectrum of fluctuations). The system simulates millions or even billions of interacting particles in an expanding universe. The simulations reveal a hierarchical manner in the structure formation, with small halos forming first and subsequently merging to form larger halos, which are consistent broadly with the observations. We will briefly summarize the distributions and profiles of dark matter halos from theoretical predictions and numerical simulations in the next section.

## 2.3 Profile and Distribution

The evolution of structure in the nonlinear gravitational region can be simulated with a high resolution. The reliability of an N-body simulation is determined by its minimum mass of elementary particle and its grid resolution. In a pioneer paper in the 90's, the large N-body simulations was performed [42] and a power law $\rho \sim 1/r$ was proposed to fit the halo profile in the central part. Recent N-body simulations, such as works from Millennium [43] and Via Lactea [44], confirmed this result and suggest that radially symmetric dark matter halos in a large mass range can be parametrized by a universal density profile of the form [1]:

$$\rho(r) = \frac{\rho_s}{(r/r_s)^{\gamma}[1+(r/r_s)^{\alpha}]^{(\beta-\gamma)/\alpha}} \,. \tag{2.5}$$

In Tab. 2.1, we give the values of the parameters $(\alpha, \beta, \gamma)$ for some of most widely used profiles such as the Kra [45], NFW [46] and Iso [47] profiles. We can see that the slopes of the density profiles in the inner regions are significantly different. In the most extreme case [48, 49], the inner profile could be as steep as $r^{-1.5}$. Note that an NFW profile is based on a conservative assumption relative to this steeper profile which would consequently lead to a larger dark matter signal at the central region.

Alternatively, it has been suggested that another kind of profile, the Einasto profile [50] with the power-law logarithmic slope in radius, can also fit the simulation data over large mass scales. The Einasto profile has a finite central slope, unlike the NFW profile which has a divergent central density. Because of the limited

resolution of N-body simulations, it is not yet known which model provides the best description of the central densities of the simulated dark-matter halos. The Einasto profile introduces a third parameter, $\alpha$, which regulates the transition of the power-law slopes:

$$\rho(r) = \rho_s \exp\left(\frac{2}{\alpha}\right) \exp\left[-\frac{2}{\alpha}\left(\frac{r}{r_s}\right)^{\alpha}\right] . \tag{2.6}$$

The parameter $\alpha$ has been found to depend systematically on the formation history of halos [51].

Conveniently, the parameters $r_s$ and $\rho_s$ can be replaced with virial mass $M$ and concentration parameter $c$ in Eq. (2.5). The concentration parameter is defined as $c \equiv r_{vir}/r_{-2}$, where $r_{-2}$ is the distance at which the profile falls as $r^2$ ($r_{-2} = r_s$ for the NFW profile) and $r_{vir}$ is the virial radius of the halo with the mass $M$. The term *virial* means that the average gravitational potential energy is twice the average kinetic energy. Within the context of the spherical collapse model, the outer extent of the cluster is taken to be the virial radius

$$r_v = \left[\frac{3M}{4\pi\rho_m(1+z)^3\Delta_c(z)}\right]^{\frac{1}{3}} , \tag{2.7}$$

where $\rho_m(1+z)^3$ is the average physical background matter density of the Universe at redshift $z$, and

$$\Delta_c(z) \simeq 18\pi^2\left[1 + \frac{88}{215}\left(\frac{1-\Omega_m}{\Omega_m(1+z)^3}\right)^{\frac{86}{95}}\right] \tag{2.8}$$

is the overdensity of the halo relative to the background density [52] (common values $\sim 200$).

For the NFW profile, A combination of the definitions of virial mass and density profile gives

$$\rho_s = \frac{\rho_m(1+z)^3\Delta_c(z)}{3}\frac{c^3}{\ln(1+c) - c/(1+c)} \tag{2.9}$$

Together, $c$ and $M$ completely determine the dark matter distribution of a given halo. When adopting a NFW profile, the mass of the Milky Way halo has been estimated to $1 \times 10^{12} M_\odot$ and $c$ to be 12 (which corresponds to $r_s = 21.7$ kpc) [53].

The dependence of concentration parameter on the halo mass and redshift has been found in N-body simulations. The typical models proposed to describe $c(M, z)$ agree fairly well within the mass interval resolved in N-body simulations [51, 54, 55, 56]. However, the relation $c(M, z)$ can differ substantially especially when extrapolated to lower mass range and to high redshifts. A conservative value of $c(M = 10^{-6}\, M_\odot, z = 0) \simeq 70$ can be obtained by extrapolating

$$c(M, z) = 4\,\frac{1+z_c}{1+z} \tag{2.10}$$

to the low mass range [54]. Here the collapse redshift $z_c$ is implicitly given by the relation $M_*(z_c) = 0.01M$, where $M_*(z)$ is the mass scale at which $\sigma(M_*, z) = \delta_c$. In a less conservative parametrization motivated by numerical simulations $c$ would follow a log-normal distribution with standard deviation $\sigma_c = 0.18$,

$$\mathcal{P}(\ln c|M, z) = \frac{1}{\sqrt{2\pi}\sigma_c} \exp\left(-\frac{[\ln c - \ln \bar{c}(M, z)]^2}{2\sigma_c^2}\right), \tag{2.11}$$

where the mean concentration parameter $\bar{c}$ is related to the halo mass via [57]

$$\bar{c}(M, z) = \frac{c_0}{1+z}\left[\frac{M}{M_*(z=0)}\right]^{-\alpha_c}, \tag{2.12}$$

where $c_0$ and $\alpha_c$ are constants whose numerical values [54] are typically chosen to be $c_0 = 9$ and $\alpha_c = 0.13$. However, application of this parameterization to low-mass halos and to high redshift give values that are inconsistent with other simulations [58]. A third parameterization [59] uses

$$\bar{c}(M, z) = a(z)\left[\frac{M}{M_*(z)}\right]^{b(z)}, \tag{2.13}$$

with $a(z) = 10.3(1+z)^{-0.3}$ , and $b(z) = 0.24(1+z)^{-0.3}$.

### 2.3.1 Power Spectrum and Halo Mass Function

The mass function of the halo distribution is derived from the Press-Schechter formalism [40]. In this approach, fluctuations in the linear density field with $\delta > \delta_c$ decouple from the local Hubble expansion of the Universe and collapse to form non-linear structures. The fraction of the volume that has collapsed is predicted to be

$$f_{\rm coll}(M(R), z) = \frac{2}{\sqrt{2\pi}\sigma(R, z)} \int_{\delta_c}^{\infty} d\delta\, e^{-\delta^2/2\sigma^2(R,z)}, \tag{2.14}$$

where $R$ is the co-moving radius over which the density field has been smoothed, which is related to the halo mass by $M(R) = \rho_m 4\pi R^3/3$ with $\rho_m$ the co-moving matter density of the universe. The number density of halos is given by [40, 41]

$$\frac{dn(M, z)}{dM} = -\frac{\rho_m}{M}\frac{df_{\rm coll}(M(R), z)}{dM} = \frac{\rho_m}{M} f(\nu)\frac{d\nu}{dM}, \tag{2.15}$$

where

$$f(\nu) \equiv \sqrt{\frac{2A^2a^2}{\pi}}[1 + (a\nu^2)^{-p}]e^{-\frac{a\nu^2}{2}}. \tag{2.16}$$

Here

$$\nu(M, z) \equiv \frac{\delta_c(z)}{\sigma(M, z)}, \tag{2.17}$$

and

$$\delta_c(z) \simeq 1.686 \tag{2.18}$$

is the critical density required for spherical collapse at a redshift $z$ in an Einstein-de Sitter space. The variance in the density field smoothed with a top-hat filter of radius $R = (3M/4\pi\rho_m)^{\frac{1}{3}}$ is

$$\sigma^2(M,z) = G^2(z)\int \frac{dk}{k}\frac{k^3 P_{\rm lin}(k)}{2\pi^2}|W(kR)|^2\,, \tag{2.19}$$

where

$$W(x) = \frac{3}{x^3}[\sin(x) - x\cos(x)]\,, \tag{2.20}$$

$P_{\rm lin}(k)$ is the linear matter power spectrum, and

$$G(z) = \frac{H(z)\int_z^\infty dz'(1+z')[H(z')]^{-3}}{H_0\int_0^\infty dz'(1+z')[H(z')]^{-3}} \tag{2.21}$$

is the growth factor in the linear perturbation theory, often also denoted by $D(z)$. In Eq. (2.16) $A$, $p$, and $a$ are constants. The the canonical Press-Schechter (PS) and Sheth-Tormen (ST) mass functions use the parameters $(p = 0, a = 1)$ and $(p = 0.3, a = 0.707)$, respectively. The normalization $A$ is determined by requiring mass conservation such that

$$\frac{1}{\rho_m}\int_0^\infty dM M\frac{dn}{dM} = \int_0^\infty d\nu f(\nu) = 1\,. \tag{2.22}$$

For PS $A = 1$ and for ST $A = 0.3222$.

The primordial power spectrum $P(k) \propto A_s k^{n_s}$ can be modified by the content and evolution of different matter components of the Universe due to the perturbations that enter the horizon at different epochs. This allows one to relate the linear power spectrum to the primordial power spectrum through a transfer function $T(k)$ via

$$P_{\rm lin}(k,z) = D^2(z)P_{\rm lin}(k,z=0) = D^2(z)A_s(k\cdot{\rm Mpc})^{n_s}T^2(k) \tag{2.23}$$

Fitting formula for an adiabatic CDM model give [60]

$$T_{\rm CDM}(q) = \frac{\ln(1+2.34q)}{2.34q}[1+3.89q+(16.1q)^2+(5.46q)^3+(6.71q)^4]^{-1/4} \tag{2.24}$$

where $q = k\cdot{\rm Mpc}/(h\Gamma)$ and $\Gamma = \Omega_m h\exp[\Omega_b(1+\sqrt{2h}/\Omega_m)]$. One usually uses the rms fluctuation on an $8h^{-1}$ Mpc scale to normalize the amplitude of the present power spectrum. From the five-year WMAP data [27, 61], we adopt $n_s = 0.96$, and $A_s = 1.4\times10^7$. Following Ref. [62], we may furthermore write the linear growth factor as

$$D(z) = \frac{1}{1+z}\frac{g(z)}{g(0)}\,, \tag{2.25}$$

where an approximate expression for $g(z)$ is

$$g(z) = \frac{5/2\Omega_m(z)}{\Omega_m(z)^{4/7} - \Omega_\Lambda(z) + (1+\Omega_m(z)/2)(1+\Omega_\Lambda(z)/70)}\,. \tag{2.26}$$

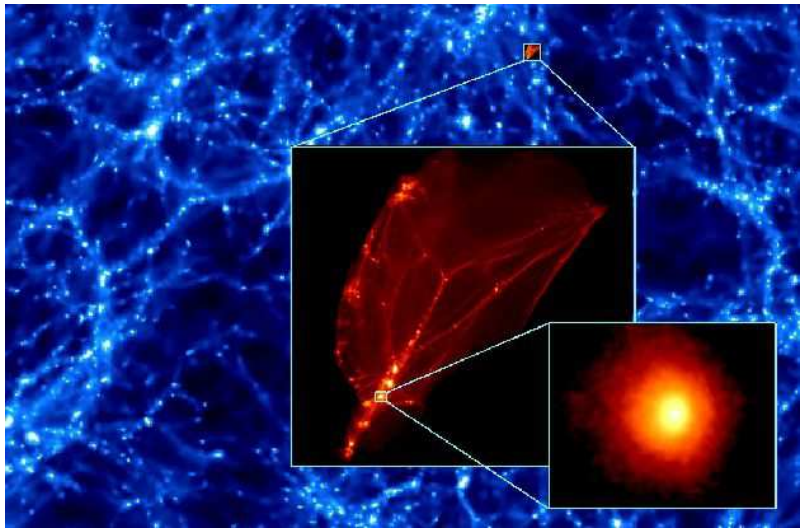

**Figure 2.4:** A zoom into one of earth mass dark halos in the Universe at redshift $z \approx 26$ (from Ref. [58]). The colours show the density of dark matter.

## 2.4 Galactic Substructure Halos

In the cold dark matter scenario, the dark halos can form at very high redshift, $z \approx 60$, with a minimum mass of $\sim 10^{-6} M_{\odot}$, determined by the free-streaming limit and the collisional damping leading to a cutoff of the primordial power spectrum [63, 64, 65, 66]. The first generation of earth-mass halos (see Fig. 2.4) have recently been simulated [58], in a good agreement with the analytic calculations. This suggests that if they can survive until the present day, an enormous number of dark matter clumps (subhalos) are expected to be embedded in our Galaxy. More Recently numerical simulations confirm this prediction [51, 58, 67, 68] (see Fig. 2.5), although the role of the tidal effects from the baryonic component has yet to be quantified and there is no direct test by observations. According to N-body simulations, a Milky Way sized halo should be surrounded by a few hundred dark matter satellites with masses larger than $10^{8} M_{\odot}$ [69, 70], whereas the observed clumps are one order of magnitude smaller than predicted. This dramatic discrepancy between the observations and the hierarchical models is sometimes referred as "the missing satellite problem". Some possible solutions to this problem are proposed mostly by adopting a considerable suppression on the amplitude of density fluctuations at small scales, which leads to the abundance of subhalos is suppressed. Such suppression can be achieved either by suitably varying parameters controlling the amplitude of the small-scale power spectrum within the ΛCDM model itself [71], by normalising the power spectrum or its large-scale tilt, or by switching to models in which the amplitude at small scales is suppressed, as in the warm dark matter (WDM) structure formation scenarios [71, 72, 73, 74, 75, 76].

More recently, several references have discussed the resulting signals from substructure halos, pointing out that those subhalos can boost annihilation rates and

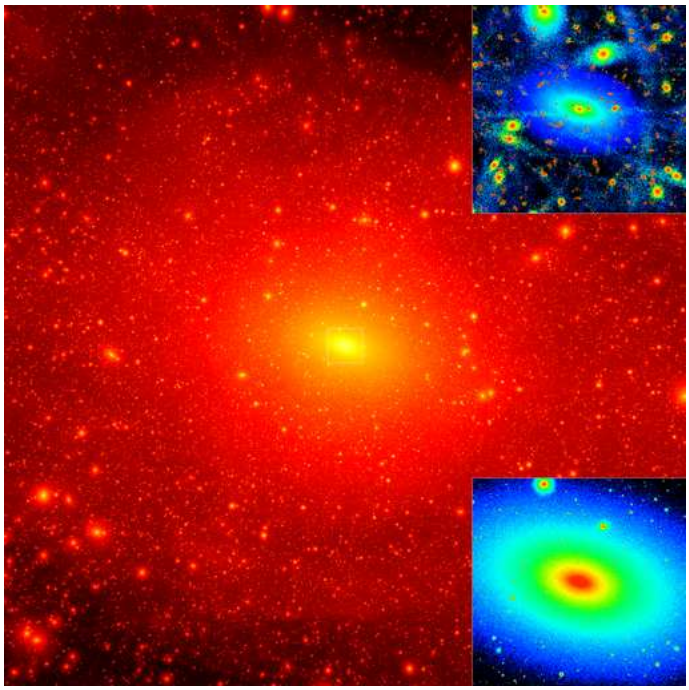

**Figure 2.5:** Dark matter substructures in our Galactic halo. Shown are projected dark matter density-square map of Via Lactea II ( see details in Ref. [68]) with a mass resolution of $4100 M_{\odot}$.

produce a distinguishing radial distribution of emissions [77, 78, 79, 80, 81]. In the following, we briefly summarize the properties of subhalos used in this thesis.

**Subhalo Radial Distribution.** There are two widely used scenarios for describing the subhalo radial distribution. One is unbiased towards the Galactic smooth component (host halo) with the NFW density profile [46] given by

$$\rho_{\rm NFW}(r) = \frac{\rho_s}{x(1+x)^2}\,, \tag{2.27}$$

As mentioned before, for a host halo with the NFW density profile we adopted $\rho_s = 0.2\ {\rm GeV/cm^3}$, $r_s = 21.7\,{\rm kpc}$ and $c_{200} \equiv r_{200}/r_s = 12$ [53]. Here I set $\Delta_c = 200$, which defines the virial mass $M_{200}$ and virial radius $r_{200}$ of a halo via $M_{200} = \frac{4}{3}\pi r_{200}^3 \Delta_c \rho_c$.

In the case where the subhalo distribution is anti-biased compared to the smooth component, we use the fitting formula of the subhalo radial distribution from Gao *et al* [51, 67]. The cumulative fraction of subhalos within a given radius is

$$\frac{N_{anti}(<\zeta)}{N_{tot}} = \frac{(1 + a\, c_{200})\,\zeta^{\beta}}{1 + a\, c_{200}\,\zeta^{\gamma}}\,, \tag{2.28}$$

with $\zeta \equiv r/r_{200}$, $a = 0.244$, $\beta = 2.75$, $\gamma = 2$ and $c_{200}$ is the host halo concentration. Furthermore, $N_{tot}$ is the total number of subhalos within virial radius $r_{200}$ of the host halo.

**Subhalo Mass Function.** Simulations suggest that the cumulative number of subhalos above a given mass $M$ can be fitted simply by a power law [55],

$$N(>M) \simeq 64 \left(\frac{M}{10^8 M_\odot}\right)^{-\alpha_m} . \tag{2.29}$$

In this thesis, we simulate the subhalos with mass down to around one Earth mass, $M_{\rm min} = 10^{-6} M_\odot$ and choose $\alpha_m = 0.9$, as suggested by simulations. We find that choosing $\alpha_m$ between 0.8 and 1 [82] would change the total annihilation rates by roughly a factor of 20.

**Subhalo Density Profile.** More recent simulations suggest that the central structure of small-scale dark matter halos deviates substantially from the NFW profile in the innermost regions, which can be well reproduced by an Einasto density profile as mentioned in Eq. (2.6). Therefore, we adopt the Einasto profile with the parameter $\alpha = 0.16$ given by Gao *et al* [51]. We use a optimistic parameterization (see Eq. (2.12)). The relation of halo concentration and mass is given by

$$c(M) = 398.1 \left(\frac{M}{M_\odot}\right)^{-0.138} . \tag{2.30}$$

The slope and normalization are consistent with those found by Bullock *et al* [54].

## 2.5 Models for Particle Dark Matter

Probably the most popular class of dark matter models is the Weakly Interactive Massive Particles (WIMPs). The main theoretical characteristics of WIMPs are that they must interact with standard particles only via the weak nuclear force and gravity, which make them non-baryonic and electrically neutral; they should carry some conserved quantum number to keep them stable at least on the cosmological timescales; they should be sufficiently heavy compared to standard particles, leading to relatively slow moving and therefore "cold" which makes structure of the Universe hierarchical. Examples for WIMPs include the Lightest Supersymmetric Particle (LSP) with R-parity conservation, such as the lightest neutralino, the gravitino, and the lightest Kaluza-Klein (KK) particle, which is predicted to be stable in some higher dimensional models.

Within standard cosmology, dark matter present relic density and can be calculated reliably if the WIMPs are thermally "freeze-out". After the inflation, due to the high temperatures ($T \gtrsim m_\chi$) in the early Universe, they are in chemical and thermal equilibrium with the primordial plasma through the electroweak interaction. The evolution equation for the WIMP number density $n_\chi$ reads [2]

$$\frac{dn_\chi}{dt} = -3Hn_\chi - \langle\sigma v\rangle(n_\chi^2 - n_{\chi,eq}^2) , \tag{2.31}$$

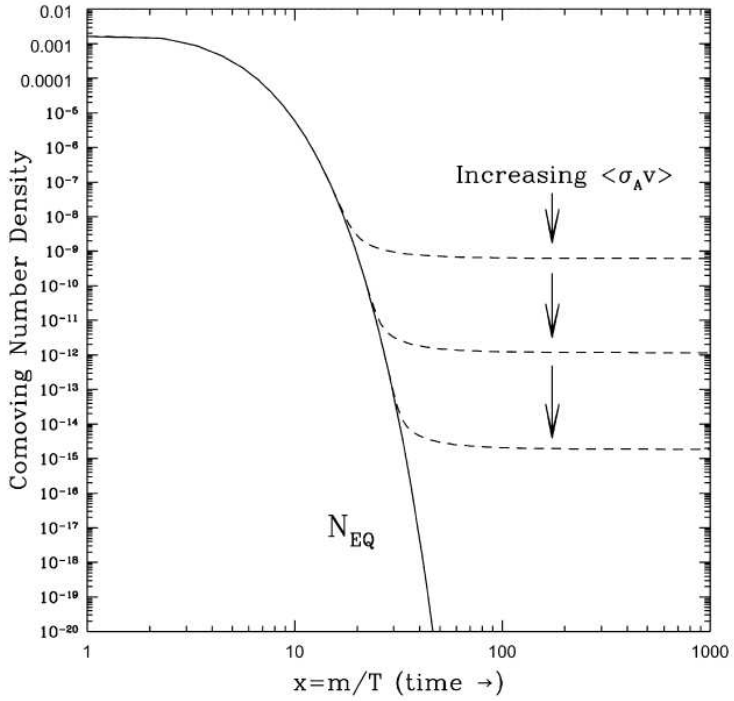


**Figure 2.6:** The dependence of relic density and thermal freeze-out temperature on cross-section from Ref. [2]. When annihilation rate becomes smaller than the expansion rate, the WIMPs fall out of chemical equilibrium. This is known as freeze out. After that, their comoving density is essentially constant. Larger cross-sections result in lower relic densities.

where $n_{\chi,eq}$ denotes the number density in chemical equilibrium and is a function of temperature, $\langle\sigma v\rangle$ is the annihilation cross-section averaged over the velocity distribution and $H$ is the Hubble expansion rate as the function of time. For non-relativistic particles ($T \ll m_\chi$), $n_{\chi,eq}$ can be written as

$$n_{\chi,eq} = g\left(\frac{mT}{2\pi}\right)^{3/2} \mathrm{e}^{-m/T}\,, \tag{2.32}$$

where $g$ is the number of degree of freedom of the particle. At high temperatures, the right-hand side of Eq.( 2.31) dominates the Hubble expansion term and the WIMP number density thus follows equilibrium solution, $n_\chi \simeq n_{\chi,eq}$. As the Universe expands adiabatically, the temperature must drop to maintain constant entropy. Consequently, because of the Boltzmann suppression (i.e. $\mathrm{e}^{-m/T}$ term in Eq. (2.32) ) of $n_\chi$ (and $n_{\chi,eq}$), the density $n_\chi$ becomes so low that the WIMP annihilation rate drops below the Hubble expansion rate. At some point $T = T_{cd}$, the comoving number density starts to deviate considerably from its equilibrium value and eventually will become essentially constant. When this occurs, the WIMPs is said to be "frozen out". The typical value for WIMPs happens around $T_{cd} \sim m_\chi/25$ [2]. This means that WIMPs are already non-relativistic when they decouple from the ther-

mal plasma. After chemical decoupling, the WIMPs may still continue scattering elastically with other particles until kinetic decoupling happens [83, 84]. After that, elastic collisions between WIMPs become very infrequent and therefore WIMPs act as the collisionless cold dark matter.

Based on the above discussion, the dark matter relic density is determined by the history of the Hubble expansion rate until the chemical freeze-out and by the annihilation rate and can be obtained by solving Eq. (2.31) numerically. Some example solutions of relic density for WIMPs with different cross-sections are shown in Fig. 2.6. We find that larger annihilation cross-sections can cause the particle to freeze out later, and result in a lower relic density. For a good approximation (ignoring logarithmic corrections), the present relic density is given by [2, 22]

$$\Omega_\chi h^2 \approx 0.1 \frac{3 \times 10^{-26} \mathrm{cm}^{-3}\mathrm{s}^{-1}}{\langle \sigma v \rangle} \,. \tag{2.33}$$

From cosmological observations, the obtained value of the relic density is $\Omega_\chi h^2 \sim 0.1$, which requires the annihilation cross-section to be $\langle \sigma v \rangle \sim 10^{-26}\mathrm{cm}^{-3}\mathrm{s}^{-1}$. If the WIMPs has a mass at the electroweak scale $m_\chi \sim 100\mathrm{GeV}$, their annihilation cross-section for weakly interacting particles can be estimated as $\langle \sigma v \rangle \sim \alpha^2/m_\chi^2 \sim 10^{-25}\mathrm{cm}^{-3}\mathrm{s}^{-1}$, where $\alpha$ is the fine structure constant. It is appealing that the predicted relic density agrees fairly well with the observations within one order of magnitude and therefore WIMPs are considered to be one of the most likely candidates for cold dark matter.

In addition, if the conserved quantum number is slightly violated, dark matter will become unstable and *decay* happens. There exist a large number of interesting and theoretically well motivated dark matter models that *predict* the decay of dark matter on the cosmological time scales, namely with lifetime longer than $\tau_\chi \simeq \mathcal{O}(10^{26})\mathrm{s}$, which are typically required to be consistent with current observational limits [3, 4, 5]. Among these candidates is the gravitino in small $R$-parity breaking scenarios (motivated by requiring a consistent thermal history of the Universe [85]) and models of sterile neutrinos, whose long lifetime is due to tiny Yukawa couplings (see Ref. [86] and references therein). Other interesting models include kinetically mixed hidden gauge bosons and gauginos [87, 88]. Even in models where the dark matter candidates are stable in the first place, the consideration of higher-dimensional operators often renders the dark matter candidate particle unstable within the cosmological lifetime [89].

Furthermore, it is expected that the self-annihilation or the decay of dark matter can give rise to significant fluxes of gamma-rays, electrons, positrons, neutrinos, and even some antimatter such as anti-protons and positrons, especially in regions with high dark matter density. We will concentrate on *indirect searches* of dark matter later in chapters 5 and 6, providing the most stringent constraints on the properties of dark matte from astrophysical measurements.

# Chapter 3

# Astronomical Observations

The multi-wavelength searches of dark matter can produce much information from astrophysical radiation backgrounds and cosmic-ray signals also provide useful complementary information. In this chapter, we briefly review the aspects of radio and gamma-ray astronomy and the cosmic-ray antimatter measurements. These are useful in comparing dark matter signatures with the astrophysical backgrounds.

## 3.1 Radio Astronomy

Radio astronomy is one of the most important tools for astronomical observations. Radiation frequencies in the Universe range from 3 Hz to 300 GHz or wavelengths from $10^5$ km to less than 1 mm. The first detection of radio emission from the Milky Way was made in 1932 by Karl Jansky, whose discovery marked the birth of radio astronomy. Technological developments during the Second World War brought a huge improvement in radio reception methods, and the new antennas and sensitive receivers were developed. In the 1950s and 1960s, significant events in radio astronomy are the discovery of 21-cm hydrogen line, quasars, pulsars, and the CMB, which contributes to a great part of our understanding of the Universe.

Radio astronomers often use distinguishing methods to gather radiations. Instead of immediate measurement, the radio radiation is amplified and manipulated coherently firstly by the instrument for preserving its phase information, before it is finally detected. The radio detectors should be constructed as large as possible for obtaining large collecting area and great angular resolution. Compared with other radiations such as X-rays and gamma-rays, the radio radiations can pass through the atmosphere almost without absorption, as shown in Fig. 3.1, allowing radio observations to be made on the ground instead of being taken from airplanes, balloons, or satellites. In the following, we will briefly discuss the astrophysical origins of the extragalactic radio background and the Galactic radio foreground.

**Extragalactic Background.** The extragalactic radio background is significant for astronomers since it contains abundant information associated with the formation

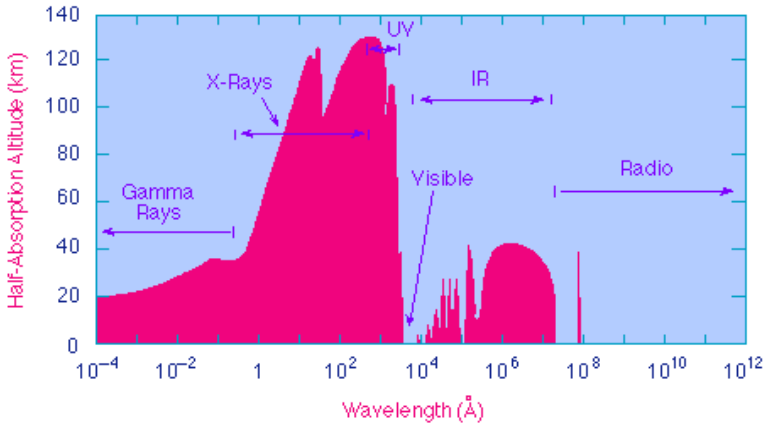


**Figure 3.1:** Electromagnetic waves of different wavelengths have different ability to penetrate the atmosphere [90]. The atmosphere is essentially transparent for optical waves and a portion of radio waves with wavelengths less than a few meters.

and the evolution of galaxies, and with the history and the large-scale structure of the Universe. In addition, the diffuse radio background is much lower than other radiation background, as shown in Fig. 3.2. This implies that the radio background would have a better sensitivity in search for the signatures of dark matter. The main contributors of the radio background can be summarized as follows:

**(i) The CMB Radiation.** The cosmic microwave background (CMB) is a radiation originating from a very early time in the Universe (at redshift $z \approx 1100$), and is predicted by the Big Bang theory as being black-body radiation at a temperature of 2.73K, which means that it peaks in the microwave range frequency of 160.2 GHz, corresponding to a 1.9 mm in wavelength. The CMB was discovered by Arno Penzias and Robert Wilson in 1964, and this discovery is considered as a landmark test of the Big Bang model of the Universe. The two well-known radio astronomy satellites were both devoted to studying the CMB. The COBE (Cosmic Background Explorer) satellite, launched in 1989, has carefully measured the spectrum of the CMB, and conclude that it is extremely close to thermal black-body spectrum at a temperature of 2.725K. Due to the quantum fluctuations of matter from the Cosmic Inflation, the CMB should contain very small anisotropies. These fluctuations were first detected by the COBE, but the COBE has only measured large-scale anisotropies with an poor angular resolution of about 7°. In June 2001, NASA launched a second CMB space mission, the Wilkinson Microwave Anisotropy Probe (WMAP), to make much more precise measurements of small scale anisotropies down to angular scales of 0.2° over the full sky. So far, the WMAP has well measured the CMB polarization and in particular the positions and amplitudes of the first three acoustic peaks in TT angular power spectrum, which enable accurate testing of cosmological models [27].

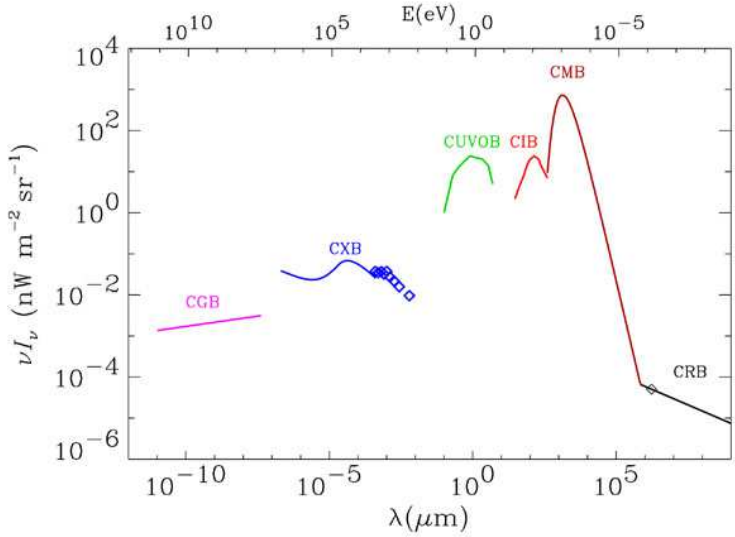


**Figure 3.2:** The comparison of the extragalactic radiation backgrounds [91], consisting of the combined flux of all extragalactic sources.

**(ii) The 21-cm Radiation.** One of the most important spectral lines in astronomy is the 21-cm line emission caused by a flip of the electron and proton spins from parallel to antiparallel, corresponding to radio waves with a wavelength of 21-cm (1.42 GHz). This "hyperfine" splitting is minuscule, so that the hydrogen is able to emit or absorb the 21-cm line even in very cold interstellar gas clouds with temperatures between 100 K to about 3000 K. In addition, the 21-cm radio emissions can penetrate the interstellar dust clouds whereas the optical photons can not do so because of the dust scattering off the high frequency radiations. The 21-cm line therefore provide an important tool to map the distribution of hydrogen which is by far most abundant in galaxies. The Doppler-shifted 21-cm lines along different lines of sight can be used to determine the rotation curves. Moreover the redshifted 21-cm line at frequencies of 200 MHz and below has the powerful ability to probe the processes of structure formation and to study the epoch of reionization ($z \lesssim 6$).

**(iii) Astrophysical Discrete Sources.** In most cases, the extragalactic radio sources has been modelled approximately with the same radio spectrum in the form of $F_\nu \propto \nu^{-0.7}$, and classified as radio-quiet AGNs, radio-loud AGNs, normal star-forming galaxies and starburst galaxies [92].

**Galactic Diffuse Foreground.** The Galactic diffuse emission mostly includes three components [93, 94]: synchrotron and free-free radiation, which are important only at frequencies below 60 GHz, and thermal emission from dust particles, which dominates at frequencies above 60 GHz (see Fig. 3.3). Free-free emission originates mainly within a few hundred pc of the Galactic disk. Generally, the synchrotron

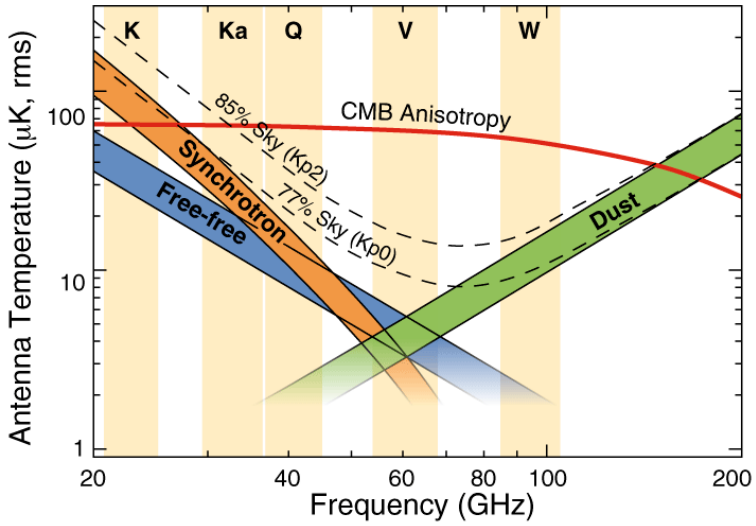


**Figure 3.3:** Frequency dependence and approximate relative strength of the CMB and Galactic three known sources of foreground emission: synchrotron, free-free, and thermal dust emission from Ref. [94]. The composite galactic emission for two sky cuts, retaining 77% and 85% of the sky respectively, are shown as dashed lines and the five WMAP radiometer bands are indicated in background.

radiation is emitted by high energy electrons gyrating in the Galactic magnetic field, while free-free emission results from the thermal bremsstrahlung from hot ($\geq 10^4$K) electrons produced in the interstellar gas by the Galactic UV radiation field. The dust emission arises from the thermal re-radiation of absorbed stellar light.

However, diffuse synchrotron and dust emissions can extend several kpc above the disk. Moreover, there are hints of a possible fourth mechanism to emit microwave radiation from rapidly spinning dust grains, though the evidence for this is still quite tentative. In principle, it is possible to distinguish these three components by measuring their different frequency dependence and spatial morphology. But the frequency dependence and spatial template are not currently well known. Recently, a global sky model with only three components was proposed [95], which can well fit the observed all-sky Galactic foreground at any frequencies from 10 MHz to 100 GHz to an accuracy around $1\% - 10\%$ depending on the frequency and the sky region.

**Haze Signals.** Recently the WMAP has revealed an excess of microwave emission 20° around the Galactic Center, with an approximate radial symmetry, known as the "WMAP haze" [96, 97, 98]. Again, Fermi-LAT reported a diffuse inverse Compton signal in the inner Galaxy with a similar spatial morphology to the "WMAP haze" [13], supporting the existence of a hard population of electrons which generate the "WMAP haze". These two facts taken together strongly suggested that the electrons responsible for these excess signals come from an unknown component

with a harder spectrum than the SN shock-accelerated electrons. One of the possible explanations is dark matter annihilation [12, 96, 99].

**Future Observations.** The future radio telescope is likely to revolutionize our knowledge about the Universe, which will allow us to observe the radio sky in unprecedented details. In space, the Planck satellite will be the third generation CMB space mission following COBE and WMAP. It was launched on 14th May 2009 and will produce full-sky map in nine frequency bands in the microwave regime between 30 and 857 GHz. The Planck satellite had successfully completed a second all-sky survey by February 2010 and some preliminary results is scheduled for public release in December 2010. The first full data release of the CMB is planned for 2012. The basic scientific goal of the Planck mission is to measure the CMB anisotropies using an unprecedented sensitivity and a high angular resolution of $5-10$ arcminutes over the entire sky, and thus the Planck satellite can detect the precise primordial fluctuation spectrum over the range from large angular scales down to 10 arcminutes, allowing the study of the secondary anisotropies in the CMB and the probing of non-Gaussian features to test inflationary models of the Universe. Also the Planck satellite can map the sky at multiple frequencies to measure the various Galactic foreground and extragalactic background emissions. Multiple frequencies combined with the known spectral dependence and measurements at different wavelengths would allow us to separate various source components from each other.

In addition, there exist two ground-based radio telescopes that will be operational in the near future. The first is the Low Frequency Array (LOFAR) [100], which is designed to operate in the 10-240 MHz frequency range with a total collecting area of one square kilometre. The construction of LOFAR has started in Netherlands and Germany, and there are plans for building a similar instrument in Australia. The LOFAR is one of the currently designed instruments with the aim to probe the end of the dark ages and cosmic reionization by measuring the redshifted 21-cm line emission to determine the neutral gas fraction in the Universe as a function of redshift and angular position.

The second telescope is the Square Kilometre Array (SKA) [101], which will be designed to operate in the whole frequency range of about 150 MHz to 22 GHz, with a total collecting area in the order of one million square metres. The construction will last most of the next decade. It will be an extremely powerful survey telescope with the capability to follow up individual objects with high angular and time resolution. The SKA will reach a point source sensitivity of 25 nJy in 1 hour of integration. The scientific opportunities of the SKA is immense and the key science projects are as follows: it can be used to discover tens of thousands of pulsars and black holes which can be used to provide fundamental and detailed tests of our current understanding of gravity; it can be used to determine the complicated processes occurring during the epoch of reionization through redshifted 21-line emission and detect star-forming galaxies at these redshifts through redshifted CO emission; it can be used to study the origin and the evolution of cosmic magnetic field by measuring the Faraday

rotation, polarized synchrotron emission and the Zeeman effect.

## 3.2 Gamma-ray Astronomy

Gamma-ray astronomy is a rather new field compared with other astronomy field such as the optical astronomy whereas it enjoyed rapid growth in recent decades. Since most gamma-rays coming from space are absorbed by the Earth's atmosphere at high latitude (see Fig. 3.1), gamma-ray astronomy could not be developed until it was possible to place detectors beyond atmosphere by using balloons and spacecraft. The gamma-ray emissions from our Galaxy were first detected by a gamma-ray detector aboard the OSO-3 satellite in 1967 and a concentration of gamma-rays in the Galactic plane [102] was found. In 1972 the SAS-2 [103] satellites not only confirmed earlier findings, but also gave the first full-sky gamma-ray image. In 1975, with relatively high resolution of instruments, the COS-B satellite [104] identified 25 point sources. The great step for gamma-ray astronomy comes from the Energetic Gamma Ray Experiment Telescope (EGRET), which is one of four instruments added on the Compton Gamma Ray Observatory (CGRO) satellite launched in 1991 [105]. So far, the most surprising results were detected by EGRET. With modern gamma-ray imaging systems and spectrometers, especially by using scintillators that convert gamma-rays into visible photons, EGRET created a detailed full-sky gamma-ray map in an total energy range from 30 MeV to 30 GeV, by which one was able to solve many puzzles about gamma-rays. EGRET also provided the first accurate measurement of the diffuse Galactic and extragalactic gamma-ray emissions, which are tightly related with the distributions of the Galactic high energy cosmic-rays and the origins of gamma-rays in the early Universe, respectively. Generally speaking, energetic photons can act as an ideal carrier of information about the non-thermal relativistic processes in astrophysical settings [106] because of their fundamental properties: (1) they can be produced copiously in many galactic and extragalactic objects due to effective acceleration of charged particles and their subsequent interactions with the ambient gas, low frequency radiation, and magnetic fields; (2) they can propagate freely in space without deflection in the interstellar and intergalactic magnetic fields; (3) they can be detected effectively by space-borne and ground based instruments. Therefore it is commonly believed that high energy gamma-ray astronomy is destined to play a crucial role in the exploration of non-thermal phenomena in the Universe in their most extreme forms.

**Detection Techniques.** Generally, the energy band of gamma-ray astronomy extends over several orders of magnitude, typically from 500 keV to more than 1 TeV. Since the wavelength of gamma-rays is much shorter than the sizes of atoms in a mirror, gamma-rays cannot be focused by reflection. Gamma-rays thus are usually detected indirectly. For gamma-rays with energies $\lesssim$ 100 GeV, the detectors on a satellite typically use scintillators or solid-state detectors to transform the gamma-rays into optical or electronic signals via Compton scattering, photo-absorption,

or pair production, which can create high-energy electrons or positrons as charged particles interacting with the matter in the detectors. For the higher energy gamma-rays ($E_\gamma \gtrsim 100$GeV), the detectors are mainly based on air Cherenkov telescopes on the ground which can trace Cherenkov light from the air showers generated by the high-energy gamma-rays interacting with the atmosphere.

**Gamma-ray Sources.** There are a number of different processes occurring in the Universe to induce gamma-ray emissions which can serve as messengers of distant cosmic events. Typically, there are several radiation processes to produce gamma-rays, e.g., through inverse Compton scattering, bremsstrahlung from charged particles deflected by atomic or molecular nucleus and the decay of $\pi^0$ produced by cosmic-ray interacting with the ISM. At present, different astrophysical objects have been observed in gamma-rays. For comprehensive reviews on this subject see *e.g.* Ref. [107, 108] and we briefly summarize the most interesting sources in the following:

**1. Active Galactic Nuclei (AGNs):** In general AGN refers to the existence of energetic phenomena in the nuclei, or central regions, of galaxies that cannot be attributed clearly and directly to stars. In some cases, the size of the AGN is smaller than the size of our solar system. AGNs are believed to host supermassive black holes in the mass range of $10^5 - 10^9 M_\odot$. Although the black hole itself is invisible, gas accreting, or falling, onto a black hole produces relativistic jets which can be observed. When the jets are directed toward the Earth we observe strong gamma-ray emissions with energies ranging roughly from MeV to TeV. This kind of AGNs are referred to as blazars. Many blazars emit a significant fraction of their radiations at energy above 100 MeV and most of gamma-rays are believed to result from inverse Compton scattering occurring within the jets or close to the black holes. In addition, AGNs that are very far from us are usually referred to as quasars.

**2. Supernova Remnants (SNRs):** SNRs are the dramatic objects produced by the violent explosion of white dwarfs (type-I) or massive stars (type-II) at the end of their lives. Pulsars (or neutron stars) are the remnant stars of core-collapse supernovae and most of them are associated with type-II supernovae. Both pulsars and ejected shells from supernovae explosions produce intense gamma-rays.

**3. Gamma Ray Bursts (GRBs):** GRBs are probably the most luminous events observed in the Universe. Today, a few thousand GRBs have been observed, mostly by the BATSE satellite experiment, whereas their origin remains a mystery. GRBs typically are short-lived lasting from a few milliseconds to less than an hour. For the long-duration bursts ($\gtrsim 2s$), they are associate with explosions from the death of massive stars in a specific kind of supernova-like event commonly referred to as a collapsar. For the short-duration bursts ($\lesssim 2s$), the merging of binary neutron stars to form a black hole has been suggested as a possible explanation.

**4. Other Contributions:** Annihilating or decaying dark matter can act as a potential gamma-ray source contributing to the background. However, their signals usually are entangled with ordinary astrophysical contributions. This topic will be further discussed in Chapters 5, 6.

**Current Observations.** So far, there exist many new gamma-ray telescopes which have entered into operation in the last few years and would highly advance this field. From the ground, new generation Imaging Atmospheric Cherenkov Telescopes (IACTs) like MAGIC [109], HESS [110], VERITAS [111] or CANGAROO-III [112] have contributed to our knowledge about gamma-rays above 50 GeV up to a few TeV. In space we have the small Italian satellite AGILE [113], and the Fermi-LAT [114] which is in operation since summer 2008 and covering energies in the range 0.02-300 GeV. We expect that the Fermi-LAT can dramatically increase the detected number of high energy gamma-ray sources, thus having a huge development in astrophysics, cosmology, and particle astrophysics.

### 3.2.1 Fermi-LAT measurements

The Fermi Large Area Telescope (Fermi-LAT) will make significant progress in understanding the high energy gamma-ray sky. In particular, Fermi-LAT has unprecedented angular resolution, precise energy sensitivity and wide field-of-view, covering the energy range from below 20 MeV to more than 300 GeV. A comprehensive description can be found in Ref. [115]. The main characteristics of Fermi-LAT and the results of 1-year operation can be briefly summarized as follows.

Since High-energy gamma-rays cannot be reflected or refracted, the Fermi-LAT is designed as a pair-conversion telescope with converter-tracker and calorimeter and a surrounding anti-coincident detector (ACD), the first two consisting of a $4 \times 4$ array of 16 modules supported by a low mass aluminum grid structure. The tracker can convert gamma-rays to $e^+e^-$ pairs and is followed by an array of CsI crystals to accurately measure the energy depositions due to electromagnetic particle showers resulting from the $e^+e$ pairs and to image the shower development profiles. Finally, the ACD is used to provide charged-particle background rejection.

Relative to earlier gamma-ray missions, the top-level performance of the Fermi-LAT is governed primarily by (1) a large peak effective area ($\sim 8000\text{cm}^2$ which is $\sim 6$ times greater than EGRET's), (2) a large field-of-view ($\sim 2.4$ sr, nearly 5 times greater than EGRET's, (3) a good background selection and event quality selection, (4) a superior angular resolution (68% containment angle $\sim 0.6^\circ$ at 1 GeV and $\sim 0.1^\circ$ above 10 GeV for the front section and about a factor of 2 larger than for the back section), (5) a fine energy resolution ($\sim 10\%$ between $0.1 - 10$ GeV and 5% for off-axis), (6) a good point source sensitivity ($\sim 3 \times 10^9\,\text{cm}^2\text{s}^{-1}$ above 100 MeV), (7) improved observing efficiency (keeping the sky in the field-of-view with scanning observations).

Consequently, data obtained with the Fermi-LAT are intended to [115] (1) per-

mit rapid notification of high-energy GRBs and transients and facilitate monitoring of variable sources, (2) yield an extensive catalog of several thousand high-energy sources obtained from an all-sky survey, (3) measure spectra from 20 MeV to more than 50 GeV for several hundred sources, (4) localize point sources to $0.3 - 2$ arcminutes, (5) map and obtain spectra of extended sources such as SNRs, molecular clouds, and nearby galaxies, (6) measure the diffuse isotropic gamma-ray background up to TeV energies, and (7) facilitate the discovery of dark matter sources.

Following its launch in June 2008, the Fermi-LAT began a sky survey in August 2008. After one year into the mission, it has already provided a wealth of information in many areas of astrophysics. Based on a threshold likelihood test statistic of 25, corresponding to a significance of just over $4\sigma$, 1451 sources were detected and characterized in the 100 MeV to 100 GeV range, shown in Fig. 3.4. As expected, the Fermi-LAT will improve our knowledge of these sources and increase our understanding of the shape and normalization of their contribution to the Extragalactic Gamma-ray Background (EGB) in the near future.

The other highlight is the results on the Galactic diffuse gamma-ray emission at energies from 100 MeV to 10 GeV at intermediate latitudes ($10^\circ \leq |b| \leq 20^\circ$), which is well reproduced by a diffuse Galactic gamma-ray emission model that is consistent with local cosmic-ray spectra but inconsistent with the EGRET GeV-excess [116, 117, 118]. In addition, the EGB is derived [119]. The component of this diffuse gamma-ray emission is generally considered to have an isotropic or nearly isotropic distribution on the sky. The derivation is based on detailed modelling of the bright foreground diffuse Galactic gamma-ray emission, the detected sources and the solar gamma-ray emission. The spectrum of the EGB is consistent with a power law with differential spectral index $\gamma = 2.41 \pm 0.05$ and intensity, $I(> 100\text{MeV}) = (1.03 \pm 0.17) \times 10^{-5}\text{cm}^2\text{s}^{-1}\text{sr}^{-1}$, where the error is systematically dominated, and not showing any excess signatures from 20 to 100 GeV (see Fig. 3.5).

## 3.3 Antimatter Signals

Because of CP-conservation, dark matter decay or annihilation usually produces the same amount of particles as anti-particles. Considered that the observed astrophysical antimatter backgrounds are much lower than the matter backgrounds, *e.g.*, the local electron fluxes are about ten times larger than the positron fluxes, the measured antimatter fluxes thus can be regarded as a ideal indicator for the signature of annihilating or decaying dark matter. Since the end of October 2008, the new experiments stirred up excitement among the astroparticle and high energy physicists. The two startling revelations about the positron excess and antiproton-to-proton flux reported by the PAMELA collaboration shook the world of cosmic-ray physics and particle physics, as shortly summarized as follows:

**Positron Fraction.** The PAMELA data [6] covers the energy range $1.5 - 100$ GeV, with significantly higher precision than other previous measurements. Two

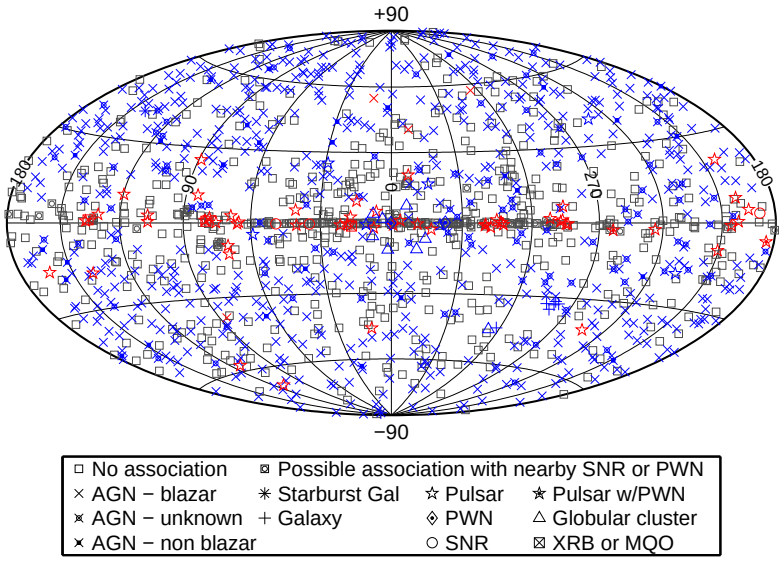


**Figure 3.4:** The First Fermi-LAT catalog (1FGL) containing 1451 sources [120].

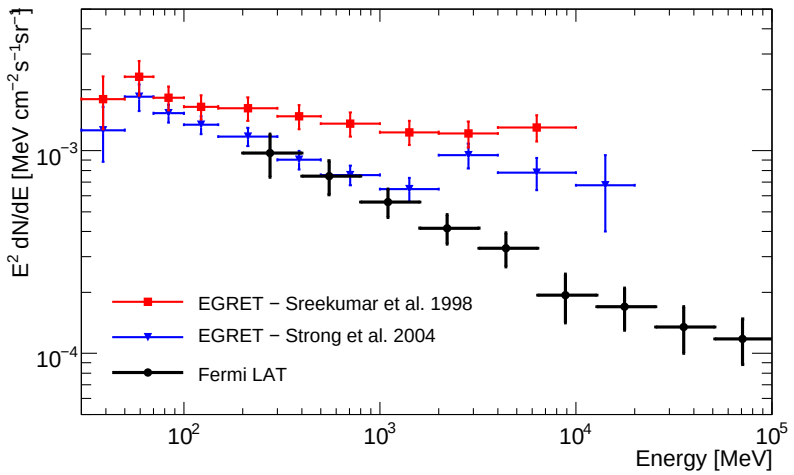


**Figure 3.5:** EGB intensity derived from the Fermi-LAT [119] compared with EGRET-derived intensities [117, 118]

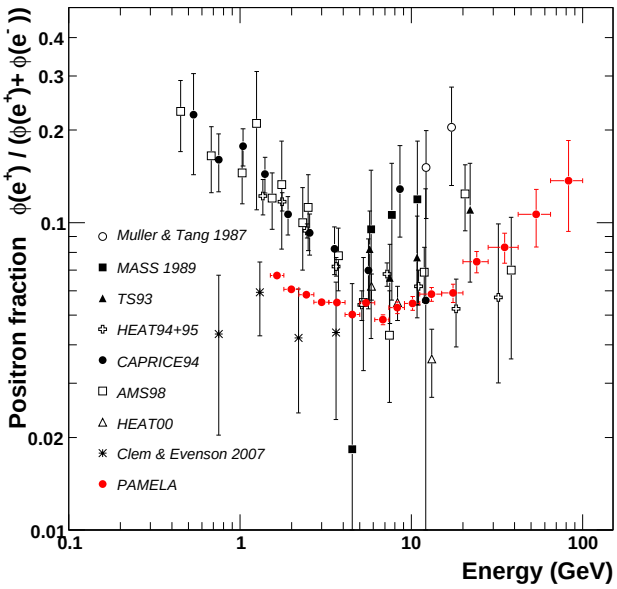


**Figure 3.6:** PAMELA positron fraction with other experimental data from Ref. [6]. The positron fraction measured by the PAMELA experiment compared with other recent experimental data [121, 122, 123, 124, 125, 126, 127, 128]. One standard deviation error bars are shown.

features are clearly visible in the data, shown in Fig. 3.6. At low energies (below 5 GeV), the PAMELA results are systematically lower than the data collected before, which could due to the uncertainty from solar modulation. At high energies (above 10 GeV), the PAMELA satellite observed and convincingly demonstrated a sharp rise of the positron fraction at energies $10-100$ GeV, possibly extending toward even higher energies. This result confirms previous measurements about the existence of a positron "excess" from HEAT [124], CAPRICE [125] and AMS-01 [121], and in conflict with theoretical predictions that the positron fractions are expected to fall as a smooth function of increasing energy for pure secondary production of positrons during the propagation of cosmic-ray nuclei in our Galaxy.

**Antiproton Ratio.** Conventionally, antiprotons are produced only from collisions of energetic cosmic-ray particles during the propagation in the interstellar gas. Cosmic-ray antiproton experiments can be used to probe the transport properties of cosmic-rays and search for or constrain exotic sources. In the past the CAPRICE98 [129], HEAT [130] and MASS91 [131] balloon-borne experiments, scientists have observed a total of about 80 antiprotons above 5 GeV. However, only two cosmic ray antiprotons with a kinetic energy above 30 GeV are reported [129]. Most recently a accurate measurement about antiproton-to-proton fluxes from 1 to 100 GeV was done by PAMELA [7]. The statistics, particularly at high energies, are significantly increased compared to all previous experiments, shown in Fig. 3.7.

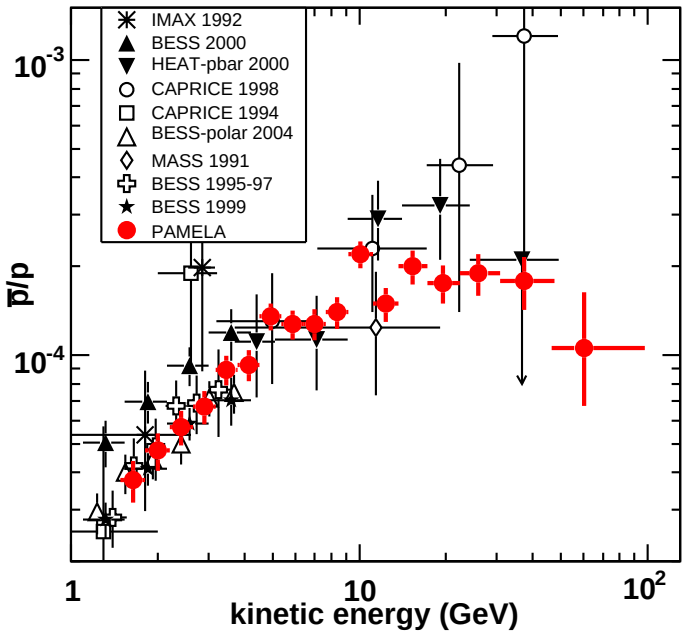


**Figure 3.7:** The antiproton-to-proton flux ratio obtained by PAMELA experiment [7] compared with other measurements [129, 130, 131, 132, 133, 134, 135].

When compared with theoretical calculation for the secondary production model, the observations are consistent very well with expected. The antiproton measurements therefore place strong constraints on the dark matter interpretation of the PAMELA positron excess, requiring the products of the annihilation/decay being dominantly leptonic rather than hadronic.

Almost at the same time, the balloon-borne experiments ATIC [8] and PPB-BETS [136] reported a narrow bump between 300 GeV and 800 GeV in the $e^+e^-$ spectrum, which however contradicts the smooth spectrum observed later by the Fermi-LAT with an unprecedented accuracy [9]. Simultaneously, the HESS collaboration [10, 11] reported a measurement of the $e^+e^-$ spectrum at energies larger than 340 GeV up to several TeV, in agreement with the Fermi-LAT result of a simple power law spectrum with spectral index of $\gamma \approx 3.0$. All these observations taken together result in many proposals trying to explain them, including the production of positrons through pair production processes in the magnetosphere of nearby pulsars [14, 16, 17, 137, 138] and the more appealing explanations like the annihilation or decay of dark matter particles in the Galactic halo [139, 140, 141, 142, 143, 144, 145, 146, 147, 148, 151, 152], and in turn, provide powerful constraints on dark matter models [19, 20] (also see Chapter 5 for details).

# Chapter 4

# Cosmic Ray Propagation

The Galactic cosmic-rays at energies below $Z \times 10^9$ GeV ($Ze$ is cosmic-ray electric charge) are confined by the Galactic magnetic fields and are assumed to propagate in a diffusive process through the Galaxy. When deflected many times by the randomly oriented magnetic fields, the cosmic-rays lose their original direction. During their propagation, secondary cosmic-rays, like Be, gamma rays, positrons, antiprotons and other light elements can be produced by cosmic-rays interacting with the interstellar medium (ISM), where cosmic-rays gain or loss energies. At present diffusion-loss model provides the most adequate description of cosmic-ray propagation in our Galaxy. The diffusion zone is usually assumed to be a cylinder with half-height $L$ of a few kpc and a radius $R \gtrsim 20$kpc. A schematic view including all the most important propagation processes is illustrated in Fig. 4.1. The diffusion-loss equation for particle density per unit of momentum interval $n(\mathbf{r}, p, t)$ can be written in the general form [153, 154]

$$\frac{\partial n}{\partial t} - \mathcal{D}n = Q(\mathbf{r}, p) \tag{4.1}$$

where the differential operator $\mathcal{D}$ is

$$\mathcal{D}n = \boldsymbol{\nabla} \cdot (D_{xx} \boldsymbol{\nabla} n - \mathbf{V_c} n) + \frac{\partial}{\partial p}\left(p^2 D_{pp} \frac{\partial}{\partial p} \frac{n}{p^2}\right) - \frac{\partial}{\partial p}\left[\dot{p}\, n - \frac{p}{3}(\boldsymbol{\nabla} \cdot \mathbf{V_c} n)\right] . \tag{4.2}$$

Here, $D_{xx}$ is the spatial diffusion coefficient, $\mathbf{V_c}$ is the convection velocity, re-acceleration is described as the diffusion in momentum space and is determined by the coefficient $D_{pp}$, and $\dot{p} \equiv dp/dt$ is the momentum loss rate. Since we are interested in relativistic electrons and positrons, we will use energy $E$ and momentum $p$ indistinctly and write $n_e(\mathbf{r}, E)$ instead of $n(\mathbf{r}, E)$ in the following.

When dark matter decays or annihilates into electrons or positrons, the source term can be written as the product of two terms, one depending on the particle property and the other on the dark matter distribution, namely

$$Q(\mathbf{r}, E) = \frac{1}{2} \langle \sigma v \rangle \left(\frac{\rho(\mathbf{r})}{m_\chi}\right)^2 \frac{dN_e(E)}{dE} \tag{4.3}$$

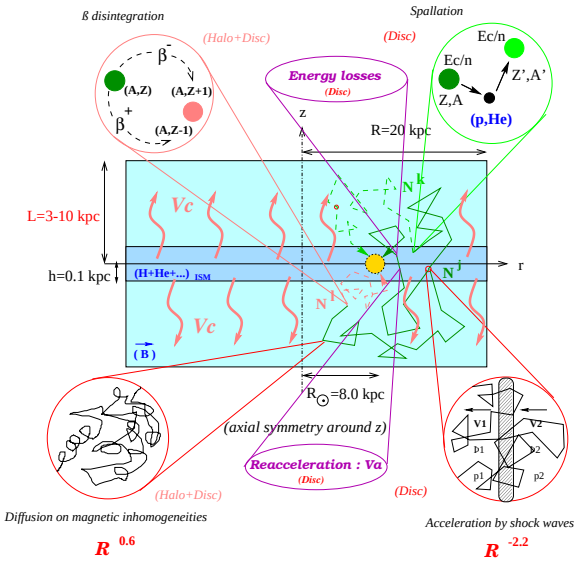


**Figure 4.1:** Schematic view of the propagation of cosmic-rays in our Galaxy from Ref. [155].

in the annihilation scenario, and

$$Q(\mathbf{r}, E) = \frac{\rho(\mathbf{r})}{m_\chi \tau_\chi} \frac{dN_e(E)}{dE} \tag{4.4}$$

in the decay scenario. Here $m_\chi$ is the mass of the dark matter; $\tau_\chi$ is the its lifetime; $\langle \sigma v \rangle$ is the annihilation cross section, and $dN_e/dE$ is the differential electron or positron spectra per decay or annihilation.

## 4.1 Relevant Processes

The diffusion term reflects the spatial propagation of cosmic-rays through the tangled Galactic magnetic fields. The diffusion coefficient $D_{xx}(\mathbf{r}, p)$ is assumed to be constant within the slab considered and is described by using a rigidity dependent function,

$$D_{xx} = \beta D_0 \left( \frac{R}{\mathrm{GV}} \right)^\delta \tag{4.5}$$

where $\beta = v/c$ is the velocity and $R$ is the rigidity of the particle defined by $R = pc/Ze$ in terms of momentum $p$ and electric charge $Ze$. The normalization $D_0$ and the spectral index $\delta$ can be determined from Boron-to-Carbon ratio data [156].

For case of re-acceleration the momentum diffusion coefficient $D_{pp}$ is related to the spatial diffusion coefficient $D_{xx}$ using the formula given in Ref. [157],

$$D_{pp} = \frac{4p^2 v_A^2}{3\delta(4-\delta^2)(4-\delta) w D_{xx}}\,, \tag{4.6}$$

where $v_A$ is the Alfven speed, and $w$ is the ratio of magnetohydrodynamic wave energy density to the magnetic field energy density, which characterizes the level of turbulence. We take $w = 1$ (since it can be subsumed in $v_A$). The re-acceleration term Eq. (4.6) is restricted to a slab of scale height $h_{\rm reac}$ which is in general associated with the gaseous disk and, therefore, smaller than the scale height of the diffusive region [158], see Tab. 4.1 below.

The convection velocity $\mathbf{V_c}$ is assumed to be cylindrically symmetric and to point in the $z$-direction perpendicular to the Galactic plane. The divergence of this velocity gives rise to an energy loss term connected with the adiabatic expansion of cosmic-rays. The energy loss term $\dot{p}$ is due to interactions of the cosmic-rays with ISM, ISRF and synchrotron radiation in the Galactic magnetic field. The ionization, Coulomb interactions, bremsstrahlung, and inverse Compton losses are also taken into account [159] and play an important role in case of re-acceleration.

The largest uncertainties in the predicted fluxes come from poorly known propagation parameters, in particular the possibility of re-acceleration of produced electrons and positrons. The corresponding uncertainty can reach one order of magnitude. We list in Tab. 4.1 six different combinations of propagation parameters for the models MIN, MED, MAX, DC, DR, L1 proposed in Ref. [158, 159, 160, 161, 162], which are compatible with the observed B/C ratio. The MIN, MED and MAX models are known to produce the minimal, medium and maximal antiproton fluxes on Earth, respectively. The L1 model is derived from [162], in which an energy dependent analysis of recent data about secondary/primary ratios allowed a fairly accurate study of the diffusion parameters $\delta$ and $D_0/L$.[1] Although the main aim of [162] was not to find a best fit model able to reproduce all the observed spectra, it is remarkable that the diffusion parameters determined via an high energy analysis are able to describe data down to energies of the order of 1 GeV/nucleon, and also to reproduce with reasonable accurately the PAMELA measurements of the antiproton flux.

Some extreme propagation models, such as the ones discussed in Refs. [163, 164, 165] which consider relatively large convection terms and anisotropic diffusion with coefficients that are different for the radial and the cylindrical directions, should be studied in future.

### 4.1.1 Boundary Conditions

In solving Eq. (4.2), traditionally, ones imposed the Dirichlet boundary condition $n_e(r, z = \pm L) = 0$, $n_e(r = r_{\rm max}, z) = 0$, at which the particles can freely escape. However, electrons and positrons are also produced by decays outside the diffusion

[1] It is a general fact that stable secondary/primary ratios do not allow to probe separately the magnitude of the diffusion coefficient and the height of the diffusion region. Unstable/stable ratios, such as the $^{10}$Be/$^{9}$Be, can in principle provide such a discrimination. The available data on such ratios, however, have very large errors, so that it is extremely difficult to extract information from them.

| Model | $\delta^1$ | $D_0$ [kpc$^2$/Myr] | $R$ [kpc] | $L$ [kpc] | $V_c$ [km/s] | $dV_c/dz$ km/s/kpc | $V_a$ [km/s] | $h_{\rm reac}$ [kpc] |
|---|---|---|---|---|---|---|---|---|
| MIN | 0.85/0.85 | 0.0016 | 20 | 1 | 13.5 | 0 | 22.4 | 0.1 |
| MED | 0.70/0.70 | 0.0112 | 20 | 4 | 12 | 0 | 52.9 | 0.1 |
| MAX | 0.46/0.46 | 0.0765 | 20 | 15 | 5 | 0 | 117.6 | 0.1 |
| DC | 0/0.55 | 0.0829 | 30 | 4 | 0 | 6 | 0 | 4 |
| DR | 0.34/0.34 | 0.1823 | 30 | 4 | 0 | 0 | 32 | 4 |
| L1 | 0.5/0.5 | 0.1523 | 20 | 4 | 0 | 0 | 10 | 4 |

**Table 4.1:** Typical combinations of diffusion parameters that are consistent with the B/C analysis. The first three propagation models correspond respectively to minimal, medium and maximal primary antiproton fluxes, abbreviated by MIN, MED, and MAX, respectively. In the DC model, the secondary $e^{\pm}$, $p$ and $\bar{p}$ fluxes fit the data well, and the DR model can easily reproduce the energy dependence of the B/C data, while the L1 model can provide a good description of B/C, $\bar{p}/p$ and data on other secondary/primary ratios above 1 GeV/n.
[1] Below/above the break in rigidity at $\mathcal{R} = 4$ GV.

zone in the Galactic halo. In this environment, they can propagate along straight lines since inverse ultra-relativistic inverse Compton scattering on low energy photons is boosted in the extreme forward direction. The energy loss time of electrons and positrons in a radiation field of energy density $u_\gamma$ is

$$\begin{aligned} t_{\rm loss}(E) = -\frac{E}{dE/dt} &\simeq 6.5\times 10^{15}\left(\frac{\rm GeV}{E}\right)\left(\frac{u_\gamma}{\rm eV\,cm^{-3}}\right)^{-1}\,{\rm s} \\ &\simeq 10^{16}\left(\frac{\rm GeV}{E}\right)\,{\rm s}\,, \end{aligned} \tag{4.7}$$

where the latter expression is often assumed throughout the Galaxy [166].

Furthermore, since $u_\gamma \simeq 1\,{\rm eV\,cm^{-3}}$ and becomes eventually dominated by the CMB far above the Galactic plane, according to Eq. (4.7) the energy loss length is $\geq 100\,{\rm kpc}$ up to TeV energies. Thus, energy loss can be neglected on halo scales. At cylindrical distance $r$ from the Galactic center, the total flux from the halo into the diffusion zone at its boundary at $z = \pm L$ is given by

$$\begin{aligned} j_e(E,\rho)_{\rm halo} &\simeq \frac{1}{4\pi}\frac{1}{m_X\tau_X}\frac{dN_e}{dE}(E) \\ &\times \int_0^{\pi/2} d\theta\cos\theta\sin\theta\int_0^{2\pi} d\phi\int_0^{\infty} ds\,\rho_X\left(\sqrt{r^2+L^2+l^2+2s(r\sin\theta\sin\phi+L\cos\theta)}\right)\,, \end{aligned} \tag{4.8}$$

where the dark matter profile $\rho_X(r)$ is assumed to be spherically symmetric and $dN_e/dE$ is the spectrum of positrons/electrons per dark matter particle decay.

In Eq. (4.8), the integration is performed over the hemisphere above or below the diffusion zone where the flux from a given direction is a line of sight integral over $s$.

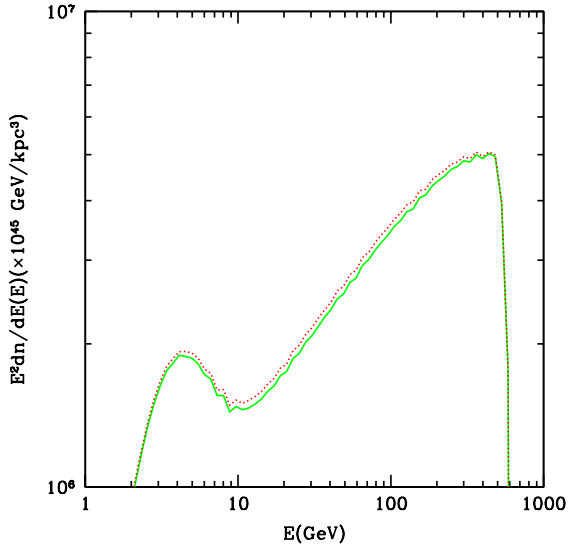


**Figure 4.2:** The dependence of electron density at Earth on boundary conditions in the MIN propagation model, for injection of one electron of 500 GeV energy. The red line refers to the Robin boundary condition Eq. (4.9), and the green one to the Dirichlet condition.

Continuity of the flux at the diffusive halo boundary then requires

$$|D_{zz}(E,r,\pm L)\,\partial_z n_e(E,r,\pm L)| = \frac{c_0}{4}\,n_e(E,r,\pm L) - j_e(E,r)_{\rm halo}\,, \tag{4.9}$$

where $n_e(E,r,z)$ is the local electron plus positron density per unit energy whose distribution is simulated in the propagation code. Eq. (4.9) then determines the boundary condition for the numerical simulation of the electron-positron distribution. Although we use this third type boundary condition at $z = \pm L$ instead of the Dirichlet boundary condition, the Dirichlet boundary condition turns out to be a very good approximation since most decays occur within 1 kpc from the Galactic center. For example, in the MIN model, considering the halo contribution, the electron/positron fluxes would increase by only 10% in Fig. 4.2, and in other propagation models with a larger diffusion zone the enhancement is negligible, as one would expect. We thus impose the Dirichlet boundary condition in the following calculations.

### 4.1.2 Magnetic Field and Photon Energy Density

Various techniques have been applied to the determination of the Galactic magnetic field. Detailed analysis of the rotation measures and dispersion of pulsar emission has been carried out [167, 168]. The work presented in Ref. [169] which is based on the large-scale data set on starlight polarization [170] with nearly 7000 stars show that the local field is parallel to the Galactic plane and follows the local spiral arms.

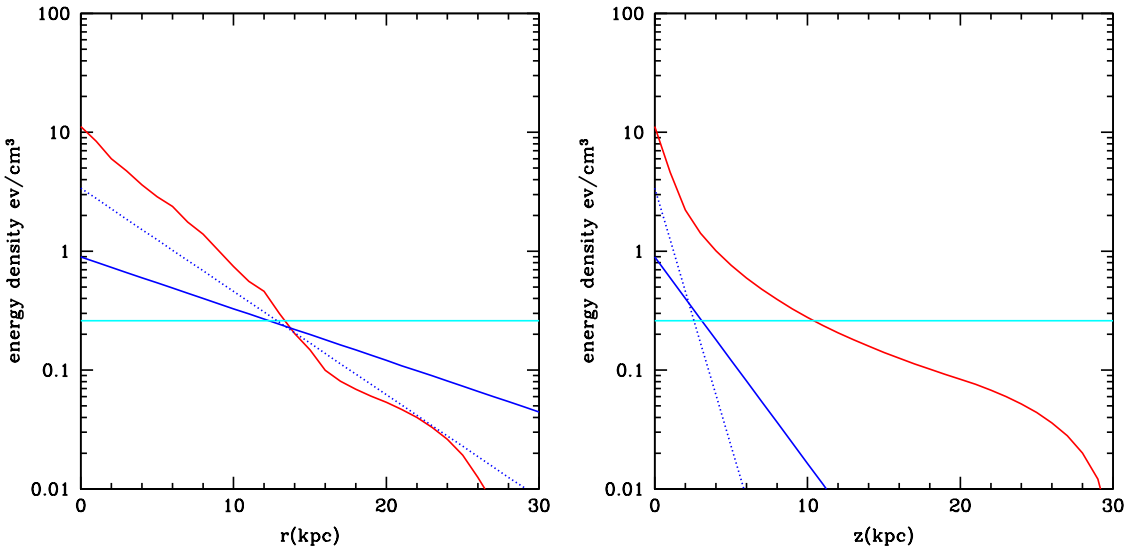


**Figure 4.3:** The interstellar photon energy density as function of $r$ at $z = 0$ and as function of $z$ at $\rho = 0$. The contributions from stellar radiation, magnetic field from Eq. (4.11) and from Eq. (4.10) as well as from the CMB are shown from top to bottom on the left side.

A smooth Galactic magnetic field is also consistent with the conclusions of Ref. [169] and can be parametrized as

$$B(r, z) = 6\, e^{(-r/20\text{kpc})} e^{-|z|/5\text{kpc}}\, \mu\text{G}. \tag{4.10}$$

Random fluctuations are not included in the model. In order to quantify the influence of uncertainties of the Galactic magnetic field on dark matter constraints, a second magnetic field model is also considered, which is parametrized by

$$B(r, z) = 5\, e^{(-(r-8.5\text{kpc})/10\text{kpc})} e^{-|z|/2\text{kpc}}\, \mu\text{G}, \tag{4.11}$$

The value of these parameters are adjusted to match the 408 MHz synchrotron distribution [171].

The magnetic field profile close to the Galactic Centre is quite uncertain and could be considerably higher than a few $\mu$G [172]. However, it is unlikely to influence the predicted signals such as synchrotron radiations beyond $\sim 5^\circ$ of the Galactic center.

The ISRF distribution can be derived based on the IRAS (Infrared Astronomy Satellite) and COBE infra-red data as well as by using information on the stellar luminosity function. A sophisticated ISRF model is proposed in the GALPROP code [171]. In this model, the ISRF energy density is about 10 eV/cm$^3$ near the center and 5 eV/cm$^3$ at the solar position.

In Fig. 4.3 we show the spatial distribution of photon energy density including CMB and magnetic field. For the electrons and positrons with energy above

1 GeV, inverse Compton scattering dominates electron energy loss since the stellar energy density $u_{\rm rad}$ is always much larger than the magnetic field energy density $u_B$. Since the synchrotron and inverse Compton processes have similar energy loss rates, the cooling time of electrons and positrons therefore are almost independent of the magnetic field. In other words, at very high energies where the diffusion length becomes large compared to the energy loss length, the number density of electrons and positrons is approximately determined by the strength of the interstellar radiation field only.

### 4.1.3 Gas Density

The production of secondary cosmic-rays species and energy losses also depend on the distribution of interstellar medium gas. The dominated component of this gas is hydrogen which consists of three different components, i.e. hydrogen $HI$, molecular hydrogen $H_2$ and ionized hydrogen $HII$, with distinctly different distributions. In general, molecular gas $H_2$ concentrates mostly in the Galactic plane and atomic hydrogen $HI$ distribute more broadly, while a relatively small abundance of ionized hydrogen $HII$ has a very broad distribution. A simple but good fit to $HI$ distribution is parameterized as an exponentially decreasing function of the halo height and can be represented by

$$n_{HI}(R,z) = n_{HI}(R) e^{-\ln 2 \cdot (z/z_0)^2}, \tag{4.12}$$

where $n_{HI}(R)$ is taken from [173] , and $z_0$ increase exponentially in the width of the $HI$ layer outside the solar circle [174], namely

$$z_0(R) = \begin{cases} 0.25 \text{ kpc}, & R \leq 10 \text{ kpc}\,; \\ 0.083\, e^{0.11R} \text{ kpc}, & R > 10 \text{ kpc}\,. \end{cases} \tag{4.13}$$

For molecular hydrogen $H_2$, the distribution can be well fitted by using the $CO$ surveys [175]:

$$n_{H_2}(R,z) = n_{H_2}(R)\, e^{-\ln 2 \cdot (z/70 \text{ pc})^2}\ . \tag{4.14}$$

For ionized hydrogen $HII$, we use a two-component model of extensive warm ionized gas added to a second component concentrated around $R = 4$ kpc [176, 177]:

$$n_{HII} = 0.025\, e^{-\frac{|z|}{1 \text{ kpc}} - \left(\frac{R}{20 \text{ kpc}}\right)^2} + 0.2\, e^{-\frac{|z|}{0.15 \text{ kpc}} - \left(\frac{R}{2 \text{ kpc}} - 2\right)^2} \text{ cm}^{-3}\ . \tag{4.15}$$

A temperature of $10^4$ K is assumed to compute Coulomb energy losses in ionized gas. The schematic radial distribution of the three components of hydrogen at Galactic plane is shown in Fig. 4.4. Finally, the $He/H$ ratio of the interstellar gas is taken as a fixed number 0.11 by using recent photospheric determinations [178].

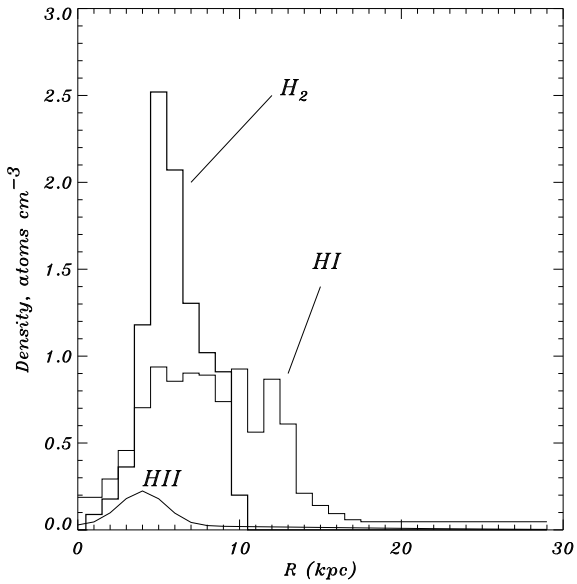


**Figure 4.4:** The radial distribution of the three components of hydrogen as a function of the radius at $z = 0$ from Ref. [159]

## 4.2 Numerical Solution

In order to solve the diffusion equation in chapter 5, we have developed our own numerical code. The main features are the same as in the GALPROP code [159]. We discretize the parameter space $(\mathbf{r}, p, t)$ using cylindrical coordinates for the position in the galaxy $\mathbf{r} = (r, z)$. The diffusion zone is confined to be a flat cylinder with radius $r_{\rm max}$ and height $2L$. The number of bins used for the simulations usually is 60 in $r$ and $z$ and 80 in $p$ (this last one in logarithmic scale). Neumann boundary conditions are imposed at the origin ($r = 0$, $p = 0$) since there is no net flux across these interfaces. In this point our code differs from GALPROP, since there no boundary conditions in $p$ are used. Our code should then provide more accurate solutions at very low energies.

We impose Dirichlet boundary conditions at the external surface of the diffusion zone by setting the electron/positron density to zero there. However, electrons are also produced outside the diffusion zone and some of them propagate into this region again. Because of this, the number of electrons in the stationary solution (within the diffusion zone) would be in reality a bit higher than our numerical results. In order to quantify this effect, a more consistent boundary condition is investigated in Sect. 4.1.1

The stationary solution is looked for by using the Crank-Nicholson implicit updating scheme. The time intervals start with $10^8$ year and are decreased to refine the solution up to a minimum of $10^2$ years. We have cross-checked our results using GALPROP in a number of relevant examples and found the agreement satisfactory. Especially, our own code have strong improvement in convergence behavior for mono-energetic injection spectra.

## 4.3 Analytical Solution

We present the analytical solution of the propagation equation with both the Green's function formalism and the Bessel-Fourier method, for a given source $Q(\mathbf{r}, E)$. For the Galactic dark matter annihilating into electrons and positrons, the advantage of Green's function is that it can be easily applied to the case of substructure halos in our Galaxy, and the Bessel-Fourier method is suitable for smooth host dark matter halo. These analytical schemes can be directly applied in chapter 6.2

### 4.3.1 Green's Function Scheme

If we neglect the convection and re-acceleration terms which are only relevant for electrons and positrons below 10 GeV [179], and assume that spatial diffusion and energy loss coefficients are spatially independent, in the steady state $\partial n/\partial t \equiv 0$, the free-space Green's function [77] for Eq. (4.1) is

$$G_{\rm free}\left[\mathbf{r}, \mathbf{r}', \lambda_D(E, E')\right] = \frac{1}{b(E)} \frac{1}{(\pi\lambda_D^2)^{3/2}} \mathrm{e}^{-(\mathbf{r}-\mathbf{r}')^2/\lambda_D^2}\,, \tag{4.16}$$

where we have defined the diffusion length as

$$\lambda_D^2(E, E') \equiv 4\int_E^{E'} \frac{D(E)}{b(E)} dE = 4D_0 \frac{\rm GeV}{b_0} \left( \frac{(E/{\rm GeV})^{\delta-1} - (E'/{\rm GeV})^{\delta-1}}{1-\delta} \right)\,, \tag{4.17}$$

which is the average distance $e^+e^-$ diffuse through during their energy loss time. Here we use $b(E, \mathbf{r}) = b_0\, E^2$ [for a more complicated treatment of energy loss see Ref.[180]] assuming Thomson limit in energy losses. Then, the Green's function satisfying appropriate boundary conditions can be obtained by considering a series of image charges at positions $x_i = x, y_i = y, z_i = (-1)^i z + 2i \cdot L$. One can verify that

$$G_{2L}(\mathbf{r}, \mathbf{r}', \lambda) = \sum_{i=-\infty}^{\infty} (-1)^i G_{\rm free}(\mathbf{r}, \mathbf{r}'_i, \lambda) \tag{4.18}$$

fulfills the Dirichlet boundary condition. Thus, the general solution to Eq. (4.1), in the limit of time-independent sources and electron/positron number densities which already reached equilibrium, is given by

$$n_e(\mathbf{r}, E) = \frac{1}{b(E)} \int d^3\mathbf{r}' \int_E^{\infty} dE' G_{2L}(\mathbf{r}-\mathbf{r}', \lambda_D(E, E')) Q(\mathbf{r}', E')\,. \tag{4.19}$$

### 4.3.2 Bessel-Fourier Scheme

Alternatively, for primary electrons and positrons from the smooth host dark matter halo, the Bessel-Fourier scheme [156, 181] can require less computational time than

the Green's function. The electron and positron number density after propagation can be expressed as

$$n_e(r,z,E) = \frac{1}{b(E)} \int_E^{M_\chi} dE' \, \frac{dN_e(E')}{dE} \, I(r,z,E,E'), \tag{4.20}$$

where $dN_e(E')/dE$ is the annihilation spectrum into electrons and positrons at energy $E'$ and $I(r,z,E,E')$ is the *halo function* defined by

$$I(r,z,E,E') = \sum_i \sum_n J_0\left(\frac{\alpha_i r}{R}\right) \sin\left[\frac{n\pi(z+L)}{2L}\right] e^{-\left[\left(\frac{n\pi}{2L}\right)^2 + \frac{\alpha_i^2}{R^2}\right]\frac{\lambda_D^2}{4}} R_{i,n} \, . \tag{4.21}$$

Here, $J_i$ denotes the i-th order Bessel function of the first kind and the $\alpha_i$ are the zeros of the Bessel function $J_0$, while $R_{i,n}$ are the coefficients of the Bessel-Fourier transform of the source term $Q(r,z,E)$:

$$R_{i,n}(E) = \frac{2}{J_1(\alpha_i)^2 L R^2} \int_0^R r dr \int_{-L}^{L} dz J_0\left(\frac{\alpha_i r}{R}\right) \sin\left(\frac{n\pi(z+L)}{2L}\right) Q(r,z,E) \, . \tag{4.22}$$

Empirically, Eq. (4.21) converges rapidly if the diffusion length $\lambda_D > 1$ kpc.

# Chapter 5

# Dark Matter Signatures in Radiation and Cosmic-Ray Fluxes

In this chapter we develop a general formalism to derive information and constraints on dark matter decaying models. We focus on three observables, namely the cosmic positron flux on Earth, the synchrotron radiation from electrons and positrons in the Galactic magnetic fields and the gamma-ray emissions from electrons and positrons from inverse Compton scattering (ICS) in the interstellar radiation field (ISRF) and the interstellar medium (ISM) to produce bremsstrahlung emissions. Each observable is supported by data. In 2008, the positron flux has been carefully measured by the PAMELA collaboration [7, 6]. For the synchrotron radiations, our analyses are based on three full-sky maps at 408 MHz [182], 1.42 GHz [183] and 22 GHz [184]. For gamma-ray emissions we use the recent Fermi-LAT results, which measured full-sky gamma-rays at the energy range between 30 MeV and 300 GeV. Usually, constraints are derived in the literature for specific dark matter scenarios with given decay spectra and branching ratios into the final state products. However, since the propagation equation is linear with respect to the electron density, each injected electron energy evolves independently. Therefore, with a finite number of numerical simulations at different injected energies we can construct a numerical *response function* of the signal to background ratio. These response functions only depend on astrophysical parameters such as the cosmic-ray propagation model and the dark matter halo profile, but not on the microscopic decay scenario. Constraints can then be simply obtained by requiring that the convolution of the response functions with a given dark matter decay spectrum be smaller than the product of decay time in $10^{26}$s and mass in 100GeV. These results were published in Ref. [19, 20]. This universal method can also be applied for annihilating dark matter scenario.

## 5.1 Estimation of Dark Matter Signals

In this section, we give some simple estimates of positron, synchrotron and gamma-ray fluxes before embarking on a more detailed calculation of the response functions.

### Electron/Positron Fluxes

The energy loss time of electrons and positrons in a radiation field of energy density $u_\gamma$ is given in Eq. (4.7). The confinement time due to diffusive propagation in the Galaxy is similar to the confinement time of hadronic cosmic-rays which at GeV energies can be estimated from secondary beryllium isotopes in the Galactic cosmic-ray flux [185],

$$t_{\rm conf}(E) \simeq 3 \times 10^7\,{\rm y} \simeq 10^{15}\,{\rm s}\,. \tag{5.1}$$

This is consistent with the diffusion time $t_{\rm diff}(E) \simeq h^2/K(E)$ in a galactic disk of height $2h \sim 4\,{\rm kpc}$ with the diffusion constant [166]

$$K(E) \simeq 3 \times 10^{27} \left(\frac{E}{\rm GeV}\right)^{0.6}\,{\rm cm^2\,s^{-1}}\,, \tag{5.2}$$

which yields

$$t_{\rm diff}(E) \simeq 3 \times 10^{15} \left(\frac{h}{2\,{\rm kpc}}\right)^2 \left(\frac{E}{10\,{\rm GeV}}\right)^{-0.6}\,{\rm s}\,. \tag{5.3}$$

The effective lifetime of electrons and positrons is thus $\tau_e(E) \simeq \min\left[t_{\rm loss}(E), t_{\rm diff}(E)\right]$. At $E \simeq 10\,{\rm GeV}$ this is, therefore, $\tau_e(10\,{\rm GeV}) \simeq 10^{15}\,{\rm s}$.

The differential flux of electrons and positrons $j_e(E)$ per energy interval from dark matter of mass $m_X$ and lifetime $\tau_X$ which produces on average $Y_e(E)$ electrons and positrons per decay and has a local density $\rho_X$ can thus be estimated as

$$\begin{aligned} E^2 j_e(E) &\simeq E\,\frac{c_0}{4\pi}\,\frac{\rho_X}{m_X}\,\frac{Y_e(E)}{\tau_X}\,\tau_e(E) \\ &\simeq 7 \times 10^{-3} \left(\frac{\rho_X}{0.3\,{\rm GeV\,cm^{-3}}}\right) \left(\frac{Y_e(E)E}{m_X}\right) \left(\frac{\tau_e(E)}{10^{15}\,{\rm s}}\right) \left(\frac{10^{26}\,{\rm s}}{\tau_X}\right) {\rm GeV\,cm^{-2}\,s^{-1}\,sr^{-1}}\,. \end{aligned} \tag{5.4}$$

Here, $Y_e(E)(E/m_X) \leq 1$ depends on the particle physics of the decays and could be of order unity.

The observed flux of electrons and positrons at $E \simeq 10\,{\rm GeV}$ is [9, 166, 186]

$$E^2 j_e^{\rm obs}(E) \simeq 2 \times 10^{-3}\,{\rm GeV\,cm^{-2}\,s^{-1}\,sr^{-1}}\,. \tag{5.5}$$

The gravitino dark matter model discussed in Ref. [187] was constructed such that the gravitino decays could explain the EGRET excess, leading to $m_X \simeq 150\,{\rm GeV}$, $\tau_X \simeq 10^{26}\,{\rm s}$. Comparing Eq. (5.4) with Eq. (5.5) shows that the electron-positron flux produced by the decays can be comparable to or even exceed the locally observed electron-positron flux. A more detailed numerical simulation is, therefore, called for.

Indirect effects such as radio emission in the Galactic magnetic field, can give complementary constraints since they are sensitive not only to the local electron-positron flux but also to the electron-positron flux induced by dark matter decay in remote parts of the Galaxy which is not directly measurable. We, therefore, now turn to radio signatures.

### Radio Fluxes

The power per frequency interval emitted by an electron or positron of energy $E$ in a magnetic field $B$, averaged over magnetic field directions, is given by [188]

$$P(\nu, E) = \frac{2\sqrt{3}e^3 B}{m_e} x^2 \left\{ K_{4/3}(x)K_{1/3}(x) - \frac{3}{5}(K^2_{4/3}(x) - K^2_{1/3}(x)) \right\} , \tag{5.6}$$

where $e$ and $m_e$ are the electron charge and mass, respectively, and we have abbreviated $x = \nu/(2\nu_c)$ where the critical frequency is

$$\nu_c(E) = \frac{3}{4\pi}\frac{eB}{m_e}\left(\frac{E}{m_e}\right)^2 = 966 \left(\frac{B}{6\mu\mathrm{G}}\right)\left(\frac{E}{100\,\mathrm{GeV}}\right)^2 \mathrm{GHz}\,. \tag{5.7}$$

For $\nu \gtrsim 10\,\mathrm{MHz}$ self-absorption is negligible and the emitted radio intensity $J(\nu)$ in units of power per frequency interval along a given line of sight is then given by

$$J(\nu) = \int ds \int dE j_e(E) P(\nu, E)\,, \tag{5.8}$$

where $s$ is the distance along the line of sight. Inserting Eq. (5.6) with the approximation $2x^2\{...\} \sim \delta(2x - 1.5)$ simplifies Eq. (5.8) to

$$\nu J(\nu) \simeq \frac{3e^{7/2}}{4(\pi \cdot 0.29)^{1/2}} \frac{\nu^{1/2}}{m_e^{5/2}} \int ds B(s)^{3/2} \left[E^2 j_e(E)\right]\big|_{E_c(\nu)}\,, \tag{5.9}$$

where the critical energy

$$E_c(\nu) = \left(\frac{4\pi}{3\cdot 0.29}\frac{m_e^3}{e}\frac{\nu}{B}\right)^{1/2} = 5.9\left(\frac{\nu}{1\,\mathrm{GHz}}\right)^{1/2}\left(\frac{B}{6\,\mu\mathrm{G}}\right)^{-1/2}\mathrm{GeV} \tag{5.10}$$

is the inversion of Eq. (5.7). Assuming the magnetic field approximately constant out to a distance $d$, for example for about 10 kpc towards the Galactic anti-center, Eq. (5.9) can be quantified as

$$\nu J(\nu) \simeq 2.6\times 10^{-4}\left(\frac{\nu}{\mathrm{GHz}}\right)^{1/2}\left(\frac{d}{10\,\mathrm{kpc}}\right)\left(\frac{B}{6\,\mu\mathrm{G}}\right)^{3/2}\left[E^2 j_e(E)\right]\big|_{E_c(\nu)}\,. \tag{5.11}$$

Inserting now the estimate Eq. (5.4), we obtain

$$\begin{aligned}\nu J(\nu) \;\simeq\; & 2.9\times 10^{-9}\left(\frac{\nu}{\mathrm{GHz}}\right)^{1/2}\left(\frac{d}{10\,\mathrm{kpc}}\right)\left(\frac{B}{6\,\mu\mathrm{G}}\right)^{3/2} \\ & \times\left(\frac{Y_e(E)E}{m_X}\right)\left(\frac{\tau_e(E)}{10^{15}\,\mathrm{s}}\right)\left(\frac{10^{26}\,\mathrm{s}}{\tau_X}\right)\mathrm{erg\,cm^{-2}\,s^{-1}\,sr^{-1}}\,.\end{aligned} \tag{5.12}$$

This is comparable to or higher than the measured high Galactic latitude radio flux, which is of order $10^{-9}\,\mathrm{erg\,cm^{-2}\,s^{-1}\,sr^{-1}}$ at GHz frequencies.

### Inverse Compton Gamma-ray Fluxes

For relativistic electrons and positrons with energy $E$ up scattering background photons from energy $\epsilon$ to $E_\gamma$, the emitted inverse Compton power per energy interval is

$$P_{\rm IC}(E_\gamma, E) = E_\gamma \int d\epsilon\; n(\epsilon) \frac{d\sigma}{dE_\gamma}(E_\gamma, \epsilon, E)\,, \tag{5.13}$$

where $n(\epsilon)$ is the differential ISRF photon number density, while the differential cross section $(d\sigma/dE_\gamma)(E_\gamma, \epsilon, E)$ is given by the Klein-Nishina formula [189]. Folding $P_{\rm IC}$ with the spectral distribution of the equilibrium number density of electrons and positrons, we get the emissivity of IC photons of energy $E_\gamma$,

$$j_{\rm IC}(E_\gamma) = \int dE\; n_e(E)\; P_{\rm IC}(E_\gamma, E), \tag{5.14}$$

which yields the IC intensity at energy $E_\gamma$ by the line-of-sight integral

$$I_{\rm IC}(E_\gamma) = \frac{1}{4\pi} \int d\ell\; j_{\rm IC}(E_\gamma, \mathbf{r})\,. \tag{5.15}$$

The IC intensity from the electrons and positrons can be simplified to

$$I_{\rm IC}(l, b, E_\gamma) = \frac{1}{4\pi} \int dE\; P_{\rm IC}(E_\gamma, E)\; \sigma_e(l, b, E)\,, \tag{5.16}$$

where $\sigma_e(l, b, E)$ denotes the column density of electrons by the line-of-sight integral of $n_e$ at a direction $(l, b)$.

There is a well known "delta-function approximation" where an electron with energy $E$ inverse Compton scattering black-body photons with temperature $T$ emits photons with a characteristic energy $E_\gamma$ in both the Thomson and extreme Klein-Nishina limits [190], *i.e.*, $P_{\rm IC}(E_\gamma, E) = P_{\rm IC}(E)\delta[E_\gamma - E_c(E)]$, where $P_{\rm IC}(E)$ is the total IC energy loss rate of the electron. The numerical calculations show that $E_c(E)$ may be approximated by $E_c(E) \simeq 4k_B T(E/m_e)^2$ and in the Thomson regime one has $P_{\rm IC}(E) = (16e^4\pi/3)u_b E^2/m_e^4$, where $e$ is the electron charge and $u_b$ is the background photon energy density. Eq. (5.16) can thus be simplified to

$$I_{\rm IC}(l, b, E_\gamma) = \frac{1}{16\pi}\, \sigma_e(l, b, E) \frac{m_e P_{\rm IC}(E)}{\sqrt{E_\gamma k_B T}}\,, \tag{5.17}$$

where the electron/positron energy $E$ is related to the gamma-ray energy $E_\gamma$ through the following condition: $E_\gamma = E_c(E)$. This relation reproduces the known slope $I_{\rm IC}(E_\gamma) \propto E_\gamma^{-(s-1)/2}$ for an electron spectrum of $\sigma_e(E) \propto E^{-s}$. In the Thomson limit and for our choice of monoenergetic injection of electron-positron pairs, the index $s \simeq 2$ in the stationary situation if the energy loss term dominates on the right hand side of Eq. (4.2), as is usually the case for electron energies above 10 GeV.

We now turn to more detailed numerical calculations of the signals induced by dark matter decay.

## 5.2 Building Response Function

The source term for positrons/electrons due to decaying dark matter particles with mass $m_\chi$ and lifetime $\tau$ is given by

$$Q_\pm(\mathbf{r}, E_0) = \frac{\rho_X(\mathbf{r})}{m_X \tau_X} \frac{dN_\pm}{dE_0} , \tag{5.18}$$

where $m_X$ is the dark matter particle mass and $\tau_X$ its lifetime, $\rho_X(\mathbf{r})$ is the dark matter density profile in our Galaxy, and $dN_\pm/dE_0$ is the spectrum of positrons/electrons per dark matter particle decay. Consider the stationary solutions $n_\pm^{E_0}(\mathbf{r}, E)$ to the propagation equation in Eq. (4.2) for monochromatic injection of positrons or electrons at $E_0$, i.e. the Green's function satisfying

$$-\mathcal{D}\, n_\pm^{E_0}(\mathbf{r}, E) = \frac{\rho_X(\mathbf{r})}{m_X \tau_X} \delta(E - E_0) . \tag{5.19}$$

The solution of Eq. (4.2) for an arbitrary spectrum $dN_\pm/dE_0$ can then be written as

$$n_\pm(\mathbf{r}, E) = \int dE_0\, n_\pm^{E_0}(\mathbf{r}, E) \frac{dN_\pm}{dE_0} . \tag{5.20}$$

The intensity signals, such as ICS gamma-ray fluxes and radio emissions due to injected mono-energetic electrons and positions at energy $E_0$ from dark matter decay inside of our Galaxy, arriving to the earth from a direction $\Omega$ characterized by galactic coordinates $\Omega = (l, b)$ is given by

$$J^{E_0}(\Omega, E_{ph}) = \frac{1}{4\pi} \int_{l.o.s.} ds \int_{m_e} dE\, n_e^{E_0}(\mathbf{r}, E) P(E_{ph}, E) . \tag{5.21}$$

Here $P(E_{ph}, E)$ is the differential photon emissivity at energy $E_{ph}$ and the spatial integral is along the line of sight. For an arbitrary injection spectrum $dN_e/dE_0$ the intensity of signals at energy $E_{ph}$ is then obtained by

$$J(\Omega, E_{ph}) = \int_{m_e} dE_0 J^{E_0}(\Omega, E_{ph}) \frac{dN_e}{dE_0} . \tag{5.22}$$

Conventionally, ones use frequency $\nu$ instead of notation $E_{ph}$ for radio emission and $E_\gamma$ for gamma-ray flux. It is then convenient to introduce the response functions for positrons $F_p(E; E_0)$ and for synchrotron emission $F_r(\Omega, \nu; E_0)$ as the ratio of the numerically computed $n_+^{E_0}(E)$ and $J^{E_0}(\Omega, \nu)$ respectively, to the observed fluxes as

$$F_p(E; E_0) = \frac{n_+^{E_0}(\mathbf{r}_{\rm earth}, E)}{n_+^{\rm obs}(E)} \left(\frac{\tau_X}{10^{26}\,{\rm s}}\right) \left(\frac{m_X}{100\,{\rm GeV}}\right) , \tag{5.23}$$

$$F_r(\Omega, \nu; E_0) = \frac{J^{E_0}(\Omega, \nu)}{J^{\rm obs}(\Omega, \nu)} \left(\frac{\tau_X}{10^{26}\,{\rm s}}\right) \left(\frac{m_X}{100\,{\rm GeV}}\right) . \tag{5.24}$$

Apart from the injection energy $E_0$, the synchrotron response function $F_r(\Omega, \nu; E_0)$ depends on the observed frequency $\nu$ and the direction in the sky $\Omega$, whereas the positron response function $F_r(E; E_0)$ depends on the observed positron energy $E$. In the latter case, we use the PAMELA data to get our constraints. It consists of seven different energies so we can construct seven different response functions, see Section 5.4. The synchrotron case is more complicated since in principle there are infinite directions to look at, and the optimal direction will depend on the injected spectrum $dN_e/dE_0$ and the observed frequency. We discuss this case in the next section.

For the gamma-ray case, taking into account that the statistics is very important for gamma-rays but negligible for radio fluxes, we introduce response functions, which are functions of the electron injection energy and are associated to gamma-ray observations in a sky patch $\Delta\Omega$ and in an energy band $E_0 \leq E_\gamma \leq E_1$:

$$F_\gamma^{E_0:E_1}(\Delta\Omega; E_e) \equiv \frac{\int_{E_0}^{E_1} dE_\gamma \int_{\Delta\Omega} d\Omega J_{\rm ICS}(\Omega, E_\gamma; E_e)}{J_{\rm obs}^{E_0:E_1}(\Delta\Omega) + 2 \cdot \delta J_{\rm obs}} \left(\frac{\tau_\chi}{10^{26}\,{\rm s}}\right) \left(\frac{m_\chi}{100\,{\rm GeV}}\right) , \quad (5.25)$$

where $J_{\rm ICS}(\Omega, E_\gamma; E_e)$ is calculated from monochromatic injection spectrum according to Eq. (5.21) and we adopt the conservative attitude of adding the $2\sigma$ error to the central value. These response functions depend neither on $\tau_X$ nor on $m_X$ and constraints on a given dark matter decay model can then be easily cast in the form

$$\begin{aligned} \int_{m_e}^{m_X} dE_0\, F_p(E; E_0) \frac{dN_+}{dE_0} &\leq \left(\frac{\tau_X}{10^{26}\,{\rm s}}\right) \left(\frac{m_X}{100\,{\rm GeV}}\right) , \\ \int_{m_e}^{m_X} dE_0\, F_r(\Omega, \nu; E_0) \frac{dN_e}{dE_0} &\leq \left(\frac{\tau_X}{10^{26}\,{\rm s}}\right) \left(\frac{m_X}{100\,{\rm GeV}}\right) , \\ \int_{m_e}^{m_\chi} dE_e\, F_\gamma^{E_0:E_1}(\Delta\Omega; E_e) \frac{dN_e}{dE_e} &\leq \left(\frac{\tau_\chi}{10^{26}\,{\rm s}}\right) \left(\frac{m_\chi}{100\,{\rm GeV}}\right) . \end{aligned} \quad (5.26)$$

The desired response functions can be computed numerically by using the methods of [159, 186]. In order to do so, we have developed our own numerical code. Details on our code and computations are described in Sect. 4.2.

Let us once more stress that our response functions do *not* depend on the specific decay spectrum, but still depend on the characteristics of propagation model and dark matter distribution. We use different halo models, always normalized such that $\rho(\mathbf{r}_{\rm earth}) = 0.3$ GeV cm$^{-3}$. For other normalizations $\rho(\mathbf{r}_{\rm earth})$, our response functions have to be multiplied by $\rho(\mathbf{r}_{\rm earth})/0.3$ GeV cm$^{-3}$.

## 5.3 Response Function for Radio Signals

In this section we compute the radio emission induced by dark matter decay and establish the response function by comparison with radio observations. As can be seen from Eq. (5.7), the radio frequencies relevant for our study are between 0.1 and

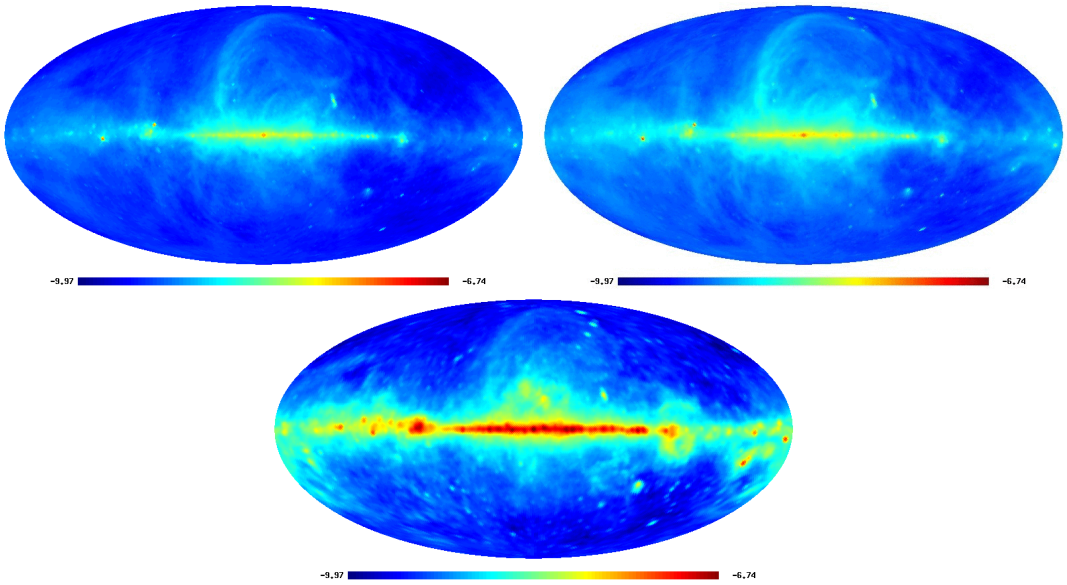


**Figure 5.1:** Maps of the radio sky at frequencies 408 MHz, 1.42 GHz, and 23 GHz, from the top left and moving clockwise [182, 183, 184]. The color scaling is the logarithm to the base 10 of the flux in erg/s/cm$^2$/sr.

a few 100 GHz. Although the CMB would dominate the radio sky at frequencies above $\simeq$ 1 GHz, this signal can be removed from the foreground based on the sensitive multi-frequency survey performed by the WMAP satellite. In Fig. 5.1, we show the full sky surveys at the frequencies 408 MHz [182], 1.42 GHz [183], and 23 GHz [184]. We do not use the higher frequency channels (33 GHz, 41 GHz, 61 GHz, 94 GHz) observed by WMAP, as they are considerably more noisy and less robust to foreground subtraction than the lower frequency bands. In addition, we smoothed all maps to angular resolution of 1°.

Furthermore, the use of the WMAP haze map (see Sect. 3.1 in details) with subtracted "known" foregrounds could further strengthen our constraints on decaying dark matter easily by an order of magnitude as has been shown already in the case of dark matter annihilation in [191]. We have, in fact, also performed this analysis and found the same order of magnitude improvement in the constraints than Ref. [191]. However, it should be kept in mind that the astrophysical backgrounds themselves depend to some extent on the not very well known the Galactic magnetic field and cosmic ray propagation parameters. Therefore, in this section we want to be conservative so we do not present response functions $F_r$ based on the haze maps or other background subtractions. The subtraction of foregrounds will be improved by forthcoming radio data from Planck and at low frequencies from LOFAR and, in a more distant future, from SKA.

### 5.3.1 Radio Emission from Dark Matter Electrons

In Fig. 5.2 we show the radio emission from dark matter decay for the five propagation models of Tab. 4.1 and for the three halo density profiles of Tab. 2.1. For the sake of illustration, we adopted a dark matter of 100 GeV, a lifetime of $10^{26}$ s, and we use a decay spectrum $dN_e/dE = \delta(E - m_X)$ such that the total energy goes into one electron.

From our numerical calculation illustrated in Fig. 5.2, it is clear that the largest uncertainty of synchrotron radiation comes from the propagation models. The average radio flux can differ by a factor of ten. For the MIN model, since the height of the diffusion zone is smallest, most of the radio emissions occurs at low latitudes. In other propagation models the radio emission is more extended because of the larger diffusion coefficient and the larger scale height of the diffusion zone which leads to more dark matter decays contributing.

Compared to the diffusion models MIN, MED and MAX, the DC and DR models always produce smaller signals over the whole diffusion zone. This is mostly due to the larger diffusion coefficient which allows the electrons to escape more easily from the diffusion zone corresponding to fewer confined electrons. Meanwhile, the power of re-acceleration, described by $D_{pp}$ in Eq. (4.2), is also weaker since it is inversely proportional to the diffusion constant ($D_{pp} \propto D_{xx}^{-1}$), see Eq. (4.6). This implies that re-acceleration plays an important role in propagation models.

We also study the variation of the synchrotron emission due to different halo profiles. In general, decaying dark matter with the NFW profile produces the largest average diffuse radio signals due to the relatively steeper slope of the density distribution. For the other two profiles the emissions are comparable with each other. Since the decay rate is only proportional to the density, uncertainties from the halo profiles do not alter the resulting dark matter constraints significantly. We do not take into account any possible small-scale structure of dark matter halos since due to the linear scaling of injection rates with dark matter density it has much smaller influence on fluxes than in annihilation scenarios.

### 5.3.2 Response Functions

Assuming a propagation model and dark matter profile, the radio emission produced by dark matter decay can be obtained for any given decay spectrum. Then an excess map can be calculated in comparison with observed radio maps, defined as the map of the ratio of predicted to observed radio flux in a given direction. One can scan the whole excess map pixel by pixel until the largest excess is obtained. This pixel, therefore, corresponds to the optimal direction for observation.

Figure 5.3 shows several examples of these excess maps at the frequencies 408 MHz, 1.42 GHz, and 23 GHz, respectively. For the sake of illustration, we assumed dark matter particles with $m_X = 100$ GeV with an NFW halo profile and decaying into one monochromatic electron or positron. The most important feature in Fig. 5.3 is that the best directions for dark matter constraints do not point towards the

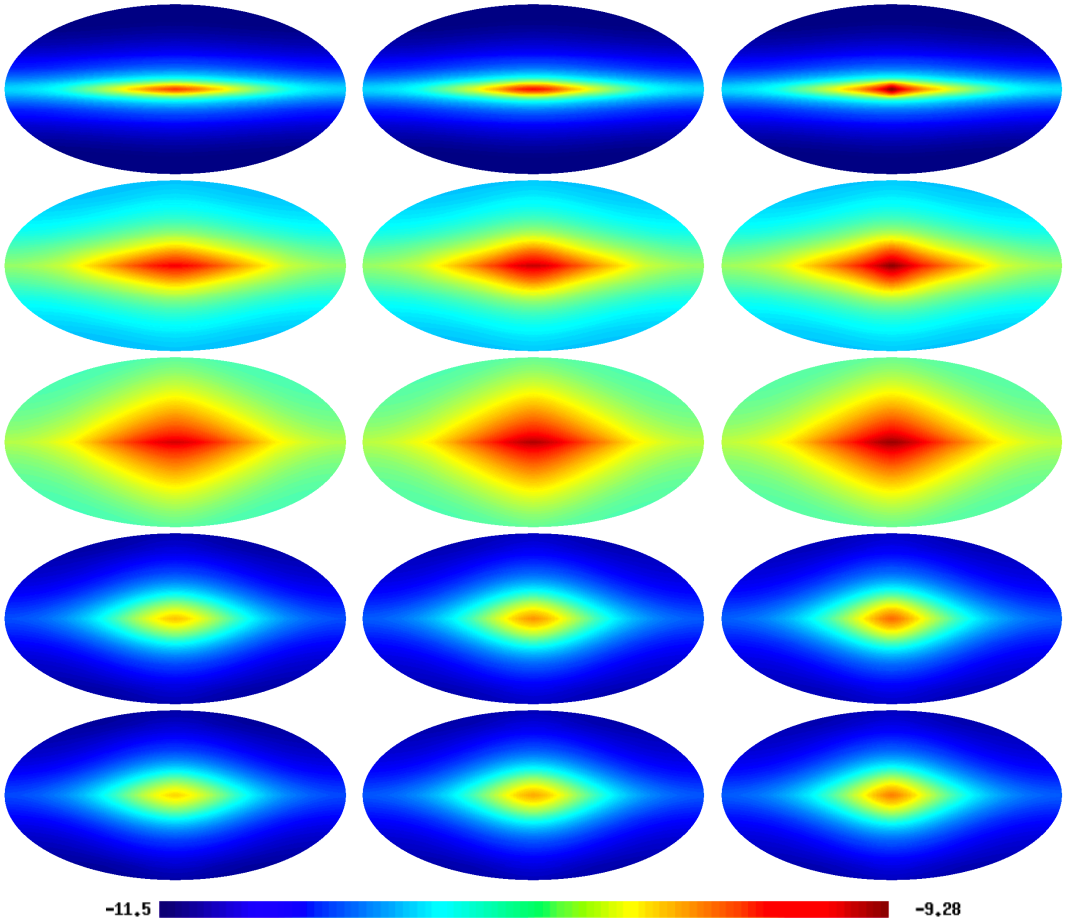


**Figure 5.2:** Model dependence of radio signatures at 1.42 GHz induced by decays of dark matter particles with $m_X = 100\,\mathrm{GeV}$, $\tau_X = 10^{26}\,\mathrm{s}$, for an injection spectrum $dN_e/dE = \delta(E - m_X)$. Results for the five different diffusion models of Tab. 4.1 (from top to bottom: MIN, MED, MAX, DC and DR) and for the three dark matter halo profiles of Tab. 2.1 (from left to right: Kra, Iso and NFW) are shown. The color scaling corresponds to the logarithm to the base 10 of the flux in erg/s/cm$^2$/sr. Note that the color scale corresponds to the same flux range in all panels for convenient comparison.

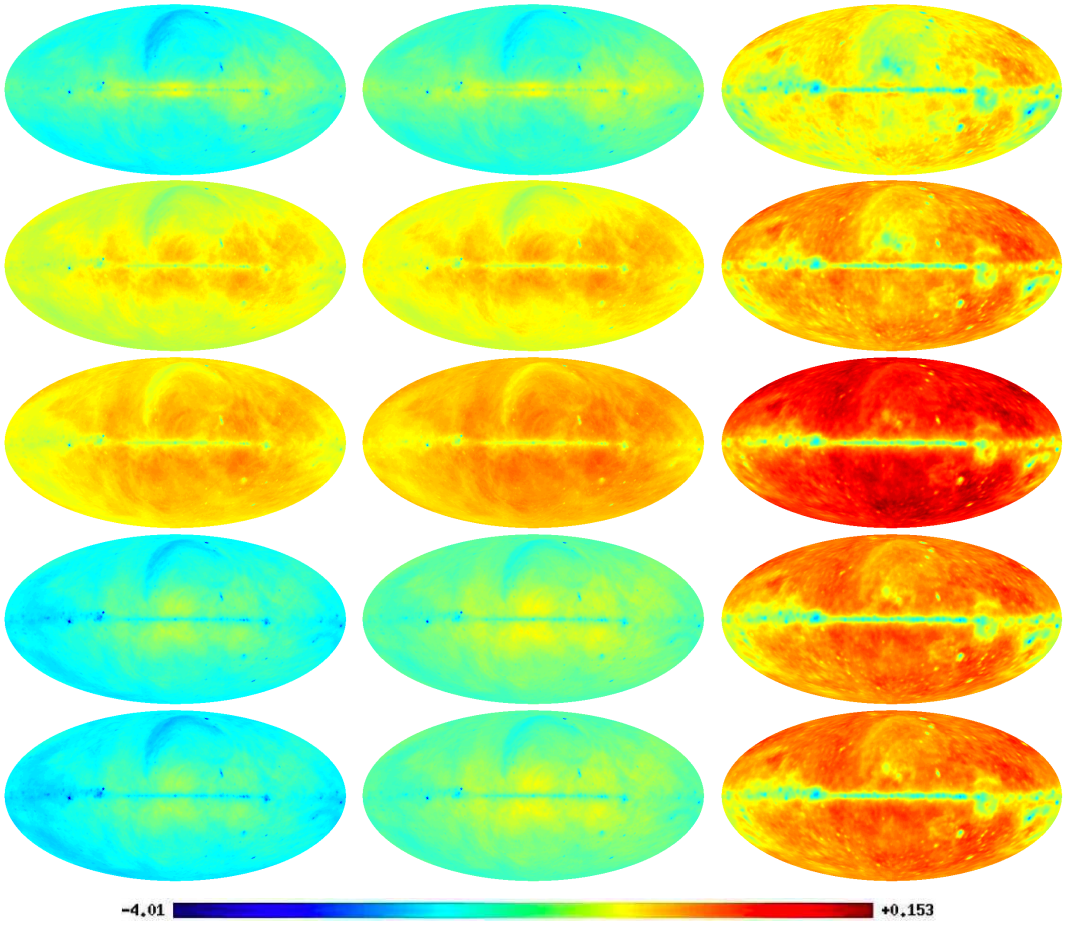


**Figure 5.3:** Excess maps, i.e. contours of predicted to observed radio flux, for decaying dark matter with $m_X = 100\,\mathrm{GeV}$, $\tau_X = 10^{26}\,\mathrm{s}$, and an injection spectrum $dN_e/dE = \delta(E - m_X)$. Results for the five different diffusion models (from top to bottom) of Tab. 4.1 and for three survey maps at 408 MHz, 1.42 GHz and 23 GHz (from left to right) are shown. Note the logarithmic color scaling for the excess, where warmer color indicates larger excesses.

Galactic center region. Although the dark matter signal close to the center is always larger than elsewhere, the observed background flux overcompensates it. Moreover, the optimal direction is not the anti-center where backgrounds are the smallest. The optimal directions tend to be not far from the center, and most of them concentrate in the southern hemisphere as many complex components such as giant molecular clouds and the north polar spur inhabit the northern hemisphere. The location of the warmest color which indicates the largest excess not only depends on which propagation model and halo profile is assumed, but also depends on frequency.

For constructing the response function, we have to perform different simulations with mono-energetic energy spectra at different injected energies $E_0$. For each of the resulting excess maps the optimal direction for observation is slightly different. We do not want to provide more than one response function per observed frequency so we have to fix one particular direction. In order to do so, we add up all the excess maps for different energies and search for the optimal direction. The selected direction is then optimized for a perfectly flat spectrum whereas it may be a bad choice for strongly peaked or hard spectra. Fortunately, our calculations show that different selections for the optimal directions do not change the response function dramatically, at most by a factor of two in the worst scenarios.

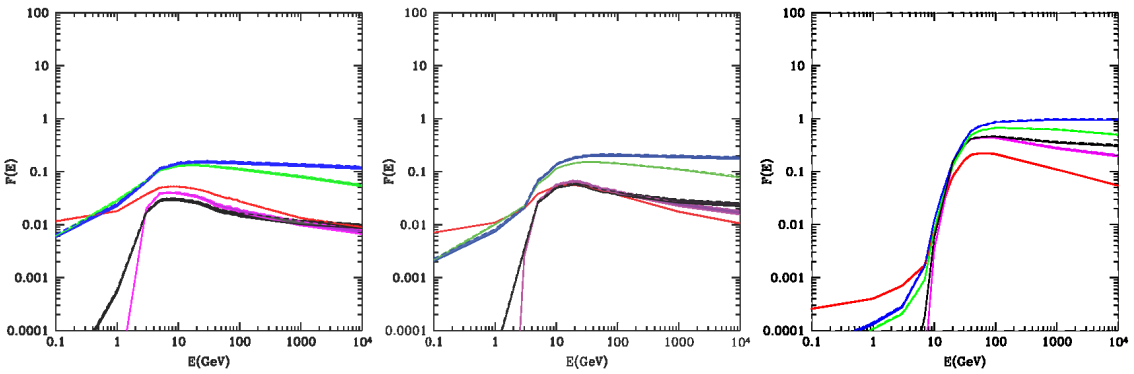


**Figure 5.4:** The model dependence of the response function based on radio emission, $F_r^J$, is shown. The response function based on the observed radio sky at 408 MHz, 1.42 GHz and 23 GHz (from left to right), respectively, are given. The red, green, blue, magenta and black bands denote the MIN, MED, MAX, DC, and DR models of Tab. 4.1, respectively. The width of the bands represents the variation within the Kra, Iso and NFW halo profiles of Tab. 2.1. The optimal directions are $(l, b) = (291°, -13.9°), (291°, -13.9°), (233°, 25°)$ for the three considered radio frequencies, respectively. Analytical fits to these curves are presented in Ref. [19].

In Figure 5.4 we present our response functions for the three synchrotron frequencies, showing the dependence on the propagation models and halo profiles. The optimal directions are shown in the caption. As indicated before, the uncertainty of the response function is dominated by the propagation model whereas the influence of the dark matter halo profile is small. This is because the best direction points far from the Galactic center, see Fig. 5.3, where the different halo models considered

are similar. On general grounds, if the optimal direction is close to the Galactic center, the excess emission will be more sensitive to the halo profile since there the dark matter density is more uncertain in the absence of sufficiently high resolution numerical simulations.

As shown in Fig. 5.4, for the radio excess maps, the MAX propagation model always gives the strongest constraints. The DC and DR models, which exhibit similar behavior, one clearly sees an exponential cut off at low injection energies, whereas the response functions for the MIN, MED and MAX models are dropping more slowly with decreasing energy. This is not surprising since, in the latter case, re-acceleration shifts lower energy electrons to higher energies. The drop at low energies in these models is strongest at the highest frequencies at which re-acceleration of the corresponding higher energy electrons is less efficient. We note that in order to reproduce the observed B/C data, the re-acceleration zone in the MIN, MED and MAX models should be limited to a slab of height $h_{\rm reac} \simeq 0.1\,{\rm kpc}$, comparable to the height of the gaseous disk. If the re-acceleration region would extend to the full height $L$ of the diffusive region, the response function would be flatter and its values would be higher by about a factor of 3 above a few tens of GeV.

To illustrate these points we show in Fig. 5.5 electron spectra in the galactic disc at 1 kpc from the center and 0.2 kpc above the disk, for different propagation models and injection energies. When re-acceleration is included, we get a noticeable bump in the spectrum at a few GeV. Above these energies, the energy loss generated from inverse Compton scattering and synchrotron emission dominates over energy gain by re-acceleration, and below a few GeV, re-acceleration overcompensates the energy losses. Thus a visible bump appears when the electrons accumulate in an energy region where re-acceleration and energy losses offset each other. It seems that the amplitude and the position of the bump is independent of the injection energy below a few GeV. The large amount of electrons and positrons accumulating in this bump region induce most of the radio signals around GHz frequencies. That is why the shape of the response function drops more gradually in the lower energy region in the MIN, MED and MAX models compared to the exponential drop in the DC and DR models.

In the DC model, due to the absence of re-acceleration, the energy spectra appear as a sawtooth shape as the number of propagated electrons above the injection energy have a sharp cutoff. Similarly, in the DR model, since the electrons and positrons can not gain enough energy from re-acceleration due to the larger diffusion parameter and the smaller Alfven speed, see Eq. (4.6), the propagated energy spectrum above the injection energy tends to zero rapidly.

Another interesting property of the response function is that it tends to fall at high energies. This can be understood as follows: Higher energy electrons either loose energy more quickly, or, if their energy loss length is still larger than the half height of the diffusion zone, can propagate further and can thus escape from the diffusion zone more readily. The diffusion length can be estimated as $\sqrt{D_{xx}(E) t_{\rm loss}(E)} \approx$ a few kpc, and is comparable to the the thickness of the diffusion zone in the MIN

and MED models. As a consequence, in Fig. 5.5 for the MIN and MED models, the propagated spectrum is indeed smaller by factors of a few for the highest injection energies. In the case of the MAX model, the half height of the diffusion zone is considerably larger than the typical diffusion scale so that the injection energy has a weak impact on electron spectrum below 100 GeV.

We note that the choice of the diffusion models and the injection energy affect the shape of the electron spectrum significantly only below 100 GeV, where the influence of the diffusion mechanism on electron and positron propagation is still important. For energies above 100 GeV, energy loss dominates the electron spectrum. The spectrum in this energy range thus should only depend on the ISRF and magnetic field and not significantly on the diffusion parameters, as is confirmed by Fig. 5.5. The plots for the DC and DR models, for which re-acceleration is insignificant, confirm our qualitative analysis. For instance, for 10 TeV injection, a flat spectrum appears at energies above 100 GeV, below which the spectrum steadily drops due to electron diffusion.

The response function reaches its maximum around the critical energy of Eq. (5.10) corresponding to the energy at which electrons emit photons of the considered frequency $\nu$ (namely about 5 GeV for 408 MHz, 9 GeV for 1.42 GHz and 20 GeV for 23 GHz, for slowly varying magnetic field of $\sim 5\mu$G strength in the regions of interest).

We also note that the response function for the DC and DR models tend to give stronger constraints than the MIN scenario for the 23 GHz map. Since the thickness of the diffusion zone in the MIN model is only 1 kpc, there is no strong emission from directions far from the Galactic center, similarly to Fig. 5.2. As a result, the optimal direction at 23 GHz points to high latitude.

## 5.4 Response Function for Positron Fluxes

Recently, PAMELA reported a relatively large positron fraction in the electron/positron flux above 10 GeV [6]. Possible explanations include as yet unknown nearby astrophysical sources or the decay or annihilation of dark matter. However, decaying dark matter models can be constrained by requiring the predicted positron flux to be smaller than the observed one. This can again be expressed in terms of a response function along the lines of Sec. 5.2. In order to convert the positron fraction given by PAMELA data [6] into the positron flux, we multiply it with the latest $e^+e^-$ flux observed by the Fermi-LAT Telescope [9] and note that the parametrizations for the Galactic electron flux in Ref. [166, 186] is larger than the new Fermi-LAT data by a factor of about 1.5 below about 30 GeV. Compared with the PAMELA data, the statistical errors of the Fermi-LAT data is sub-dominant because of the finer energy binning and the smaller statistical error of the flux. Therefore, for the statistical error of the positron flux we take into account only the statistical error of the PAMELA positron fraction data. The Fermi-LAT data are well fit by a simple power law expression $J_e = 172.37\, E^{-3.04}\,\mathrm{s}^{-1}\mathrm{m}^{-2}\mathrm{sr}^{-1}\mathrm{GeV}^{-1}$. The resulting "observed" positron flux is shown in Fig. 5.6. The strongest constraints come from

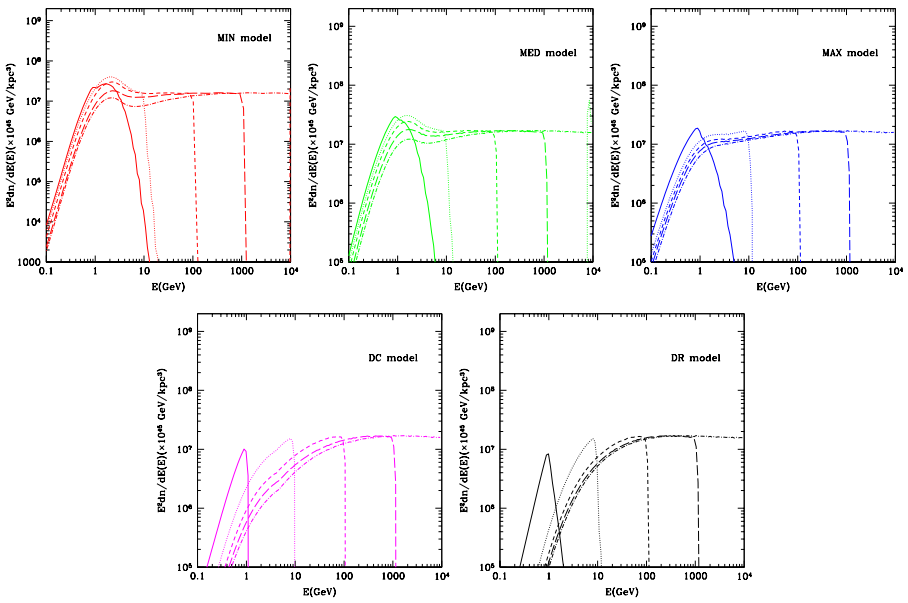


**Figure 5.5:** The electron or positron spectra versus energy at $r = 1\,\mathrm{kpc}$, $z = 0.2\,\mathrm{kpc}$ in the NFW halo model. The solid, dotted, short dash, long dash and dotted-short dash line represent an injection energy of 1 GeV, 10 GeV, 100 GeV, 1 TeV and 10 TeV, respectively. Color keys are as in Fig. 5.4.

the positron flux at the lowest energy where the statistical error is negligible.

The response functions based on the positron flux measured by PAMELA [6] are shown in Fig. 5.7. We only consider the high energy region above 10 GeV where the solar wind has no significant influence. Compared to the synchrotron response functions the positron response functions are generally larger and, therefore, in general lead to stronger constraints.

We shall note however that this would not be the case in CP-non-symmetric dark matter decay models in which the positron flux is suppressed with respect to the electron flux. In this situation one should note that synchrotron constraints based only on the electron density are stronger than those based on the locally observed electron flux itself, since the electron flux is about ten times larger than the positron flux.

Fig. 5.7 shows a prominent feature in the response function based on the PAMELA data in comparison with the response function based on the radio emission: It depends mostly on the diffusion model but little on the dark matter halo profile. This is because high energy positrons mostly come from nearby sources within $\sim 1\,\mathrm{kpc}$ where different halo profiles yield very similar dark matter densities. Further, the constraints are weakly affected by the magnetic field since energy losses are dominated by the background radiation fields.

In addition Fig. 5.7 shows that the response function cuts off below the energy at which the positron flux is observed in the DC and DR models where powerful re-acceleration is absent, as one would expect since electrons essentially can only

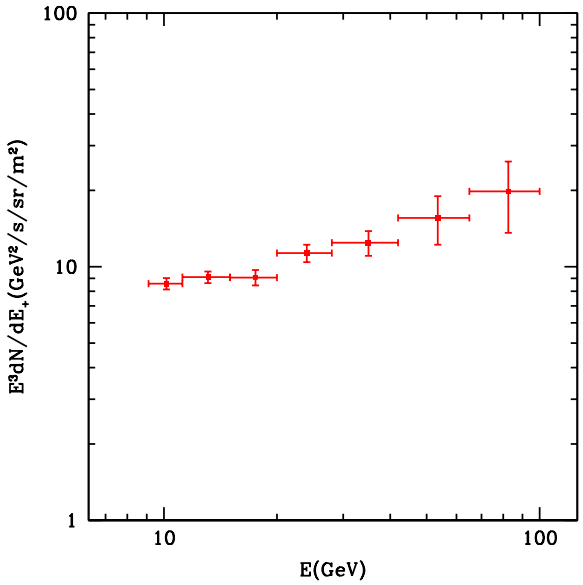


**Figure 5.6:** The positron flux observed at Earth as obtained by multiplying the $e^+ + e^-$ flux observed by Fermi-LAT [9] with the positron fraction measured by PAMELA [7, 6], see text.

loose energy in this situation. On the other hand, the response function tends to peak where the injection energy approaches the observed energy. Above that energy the response function gradually falls off due to the faster diffusion effects of higher energy positrons, similarly to the behavior of the radio based response function discussed before. The MAX scenario predicts the largest locally observed positron flux since the stronger re-acceleration in the MAX models shifts the predicted peak of the energy spectrum to larger energies, similarly to Fig. 5.5. We should note that the amplitude of the bump in Fig. 5.5 in the MAX model is somewhat lower than in the MIN and MED scenarios due to the larger diffusion parameter. However, since this bump is shifted to larger energies in the MAX model, the MAX scenario still gives the strongest constraint.

## 5.5 Response Function for Gamma-rays

In this section, we present the response functions based on the Fermi-LAT data and discuss how they are improved by the removal of astrophysical contributions of known origin to the gamma-ray signals. In the following, we will firstly discuss the different sources of gamma-ray radiation resulting from dark matter decay and the uncertainties in the predicted ICS gamma-ray fluxes.

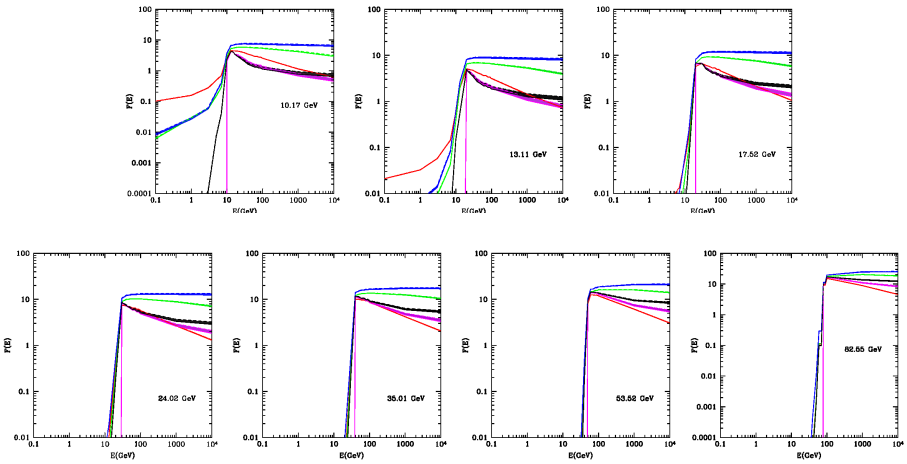


**Figure 5.7:** The response function $F_p(E)$ resulting from the observed positron flux given by PAMELA [6] for various energies at which the positron flux was observed. The model dependence is also shown. The color key is as in Fig. 5.4. Analytical fits to these curves are presented in Ref. [19].

### 5.5.1 Gamma-rays from ICS, Bremsstrahlung and Prompt Radiation

Electrons and positrons produced in the decay of dark matter give rise to a gamma-ray signal, coming from ICS off low energy photons of the ISRF. A further, mostly subdominant, contribution to the gamma-ray flux comes from bremsstrahlung of the electrons and positrons when scattering with the galactic gas. In the context of the PAMELA positron excess, ICS radiation from decaying dark matter has been discussed in Refs. [192, 193], for the case of annihilating dark matter see Refs. [194, 195]. In Eq. (5.21) for gamma-rays, the differential emissivity $P(E_\gamma, E)$ corresponds to two processes,

$$P(E_\gamma, E) = P_{\rm IC}(E_\gamma, E) + P_{\rm bremss}(E_\gamma, E) \ . \tag{5.27}$$

The first term $P_{\rm IC}(E_\gamma, E)$ corresponds to inverse Compton scattering, which is derived by convolving the differential number density of target photons with the well known Klein-Nishina cross section. The second term, $P_{\rm bremss}(E_\gamma, E)$, stems from the bremsstrahlung emission due to deflection of relativistic electrons and positrons in the electrostatic potential of interstellar gas atoms and molecules. Since this contribution is subdominant in the energy range we are interested in, we will always refer to the ICS channel as our reference channel in the following. More details of the calculation can be found in [196].

The predicted gamma-ray flux crucially depends on the *propagation model*. We select three different models, i.e. MIN, MAX and L1 listed in Tab. 4.1 characterized by different choices of the propagation parameters in Eq. (4.2). For illustrative purposes, we show in Fig. 5.8 the predicted gamma-ray emission for the L1 model

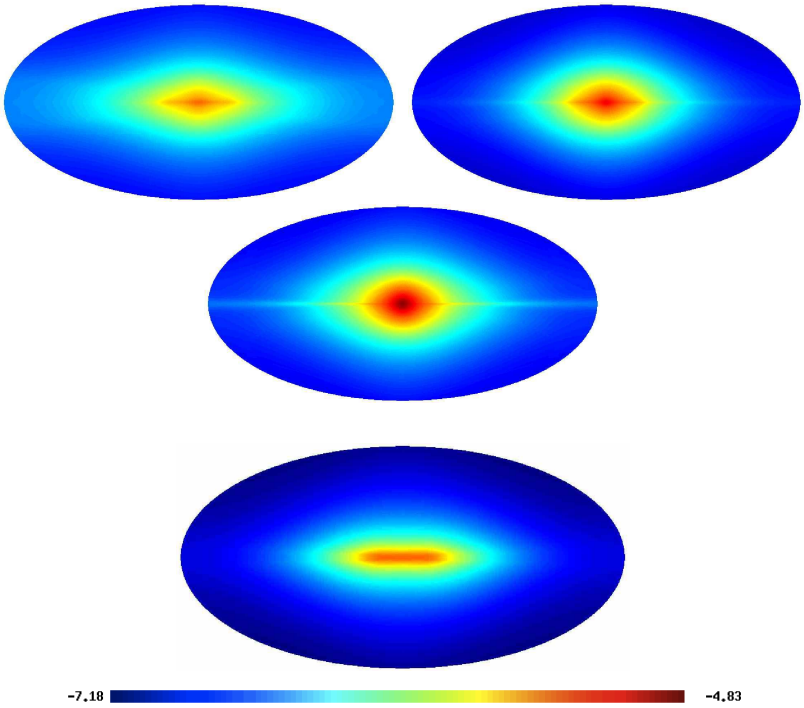


**Figure 5.8:** The gamma-ray emissions at 0.1 GeV, 1 GeV and 10 GeV (upper panel from left to right) produced by dark matter particles decaying into $e^+e^-$ pairs, where $m_\chi = 200\,\mathrm{GeV}$, $\tau_\chi = 10^{26}\,\mathrm{s}$. Results hold for the L1 diffusion model of Tab. 4.1 and for the NFW halo profile. The lower panel shows the ICS radiation from astrophysical sources at 10 GeV for comparison (again from model L1). The color scaling corresponds to the logarithm to the base 10 of the flux in GeV/s/cm$^2$/sr. Note that the color scale corresponds to the same flux range in all panels.

of Tab. 4.1 at 0.1, 1 and 10 GeV, respectively, assuming a dark matter decay into $e^+e^-$, where $m_\chi = 200\,\mathrm{GeV}$ and $\tau_\chi = 10^{26}\,\mathrm{s}$. We also show for comparison the ICS radiation from primary electrons of astrophysical origin. In general, as apparent from these plots, dark matter induced ICS radiation extends to higher latitudes than astrophysically induced ICS radiation, which is mainly concentrated on the galactic disk.

In addition to the ICS radiation produced in our Galaxy there is also a related *extragalactic* contribution, resulting from scattering of electrons from dark matter decaying outside of our Galaxy with the CMB. This component can potentially dominate the overall ICS fluxes at low energies, and we include it for completeness. The calculation is straightforward and details can be found in, *e.g.*, Ref. [192, 195]. In contrast to these references, we also took into account absorption effects due to inelastic scattering between ICS photons and the intergalactic background light (IBL), following Ref. [193, 197] (adopting the "fast evolution" model).

As mentioned before in Sect.4.1.1, a additional contribution to the ICS radiation should come from electrons and positrons produced in the dark matter decay inside

of our dark matter halo, but outside of the diffusion zone. If these particles are far enough from the galactic disk region, beyond a few kpc, their main energy loss channel is scattering with the CMB. The corresponding propagation length is $\mathcal{O}(100\text{kpc})$ for 1 TeV particles, and $\mathcal{O}(10\text{kpc})$ for 10 TeV particles. Calculating the corresponding ICS flux while neglecting the motion of the particles in general overestimates this flux by an $\mathcal{O}(1)$ factor. Being conservative we do not include this radiation component to our bounds and leave a more careful calculation for future work.

**Uncertainties.** The largest uncertainties in the predicted gamma-ray fluxes come from poorly known propagation parameters, in particular from the height of the diffusion zone. The corresponding uncertainties can reach one order of magnitude.

As we already noticed, the height $L$ is only poorly known since its determination is degenerate with the diffusion coefficient. The most widely adopted range of variation of $L$ is between 1 and 15 kpc, based on the poor quality data on $^{10}\text{Be}/^{9}\text{Be}$. Due to this uncertainty it is hard to obtain any definitive constraint on, *e.g.* , the supersymmetric parameter space of dark matter based on current anti-proton data [7, 161]. The forthcoming AMS-02 experiment [198] will however provide very accurate data on unstable/stable ratios (as well as for B/C and other stable secondary/primary ratios), which might allow a more precise determination of the diffusion height scale $L$.

In our case it is clear that a larger height of the diffusion zone leads to more dark matter decays contributing to the gamma-ray flux, because more electrons of dark matter origin are confined in the diffusive region. Uncertainties on other cosmic-ray propagation parameters, such as the Alfvèn velocity $v_A$ and the convection velocity $v_c$, are less relevant in affecting the electron distribution of dark matter, and especially affect only the electrons below around 10 GeV since higher energy electrons lose energy too rapidly via ICS and can not propagate over long distances.

We found that the full-sky ICS gamma-ray emission induced by very high energy electrons from dark matter decay obtained in the L1 model is comparable with the one obtained using other widely known models, namely DC and DR [159] which adopt the same height of the diffusion zone as our L1 model.

Another source of uncertainty comes from the dependence of the gamma-ray emission on the halo profiles. We compared the fluxes predicted for different halo models (with parameters shown in Tab. 2.1) and found that for shallower halo profiles such as the Kra [45] and the Iso [47] profile the gamma-ray emission is reduced by around 10%. On the other hand, in case of the Einasto profile (see [199] and references therein) the flux is enhanced by 30%. Since this variation is subdominant when compared with the uncertainties of the propagation models, we will simply adopt the NFW halo profile in the rest of the present work.

The gamma-ray emission also depends on the Galactic magnetic field, since synchrotron losses can be of the order of ICS radiation losses at high electron energies. The magnetic field profile close to the Galactic center is quite uncertain and could

be considerably higher than a few $\mu$G [172]. Here we adopt the field from Ref. [171] which matches the 408 MHz synchrotron distribution. We compared our results with another widely used magnetic field and found that the gamma-ray fluxes at high energies increase by just 15% by changing the magnetic field model to the one presented in Ref. [200] which is based on a large-scale data set on starlight polarization.

**Prompt Radiation.** Although this work focuses on ICS radiation produced by electrons and positrons from decaying dark matter, we cannot overlook the fact that the prompt radiation of gamma rays can be a very competitive signature of dark matter decays. Indeed, in many realistic cases it turns out that this component can be larger than the ICS and therefore it can actually give the strongest constraints.

Prompt radiation from dark matter decay is produced more frequently inside our overdense Galactic dark matter halo[1] but it is also produced at cosmological distances. At energies around 10GeV or below, the magnitude of the halo and extragalactic fluxes are of the same order when looking in direction of the anti-galactic center, whereas at higher energies around and above 100GeV the inelastic scattering between gamma-rays and the IBL reduces the extragalactic component significantly and can *not* be neglected.

We include the galactic and the extragalactic prompt radiation, following the calculations outlined in Ref. [193]. Uncertainties come mainly from the adopted dark matter halo profile and its normalization at position of the Sun.

### 5.5.2 Response Functions from ICS gamma-rays

We now turn to derive the response functions for the gamma-ray emission induced by dark matter decays into $e^+e^-$ pairs by comparing our predictions with the 1-year observations of Fermi-LAT in the energy range of 0.5 GeV to 300 GeV.

As data we use the Fermi-LAT gamma-ray maps as derived in Ref. [13].[2] In this analysis the events were binned into the eight energy ranges 0.5 - 1 GeV, 1 - 2 GeV, 2 - 5 GeV, 5 - 10 GeV, 20 - 50 GeV, 50 - 100 GeV and 100 - 300 GeV.

A few words of caution are required concerning the data basis: the adopted gamma-ray maps are based on the "diffuse" event class, which at energies above 50 or 100 GeV suffers from background contamination [201] that becomes relevant when diffuse fluxes are studied. In the highest energy regime the background contamination might be on the 50 - 80% level. Furthermore, no attempt of subtracting

[1] Although the halo profile is expected to be approximately isotropic, the corresponding flux at Earth exhibits a strong dipole-like anisotropy due to the offset between the Sun and the galactic center, which can be used to distinguish it from the extragalactic gamma-ray background, see Ref. [193].

[2] We also performed an analysis of the publicly available event data on http://fermi.gsfc.nasa.gov/ssc/data/, coming to identical results as Ref. [13]. We decided to use the maps from [13] in order to keep the data basis of our analysis easily accessible.

point sources were made. The adopted statistical errors are always derived from the exposure $3 \times 10^{10}\mathrm{cm}^2\,\mathrm{s}$, which is good enough for the purpose of this study.[1] We do not attempt to include systematic errors in the analysis, which in light of the large background contamination of the data would be too premature.

### Definitions and Optimal Sky Patch

The response functions for gamma-rays depend crucially on the chosen patch $\Delta\Omega$, which in the ideal case should cover the area with the largest signal-to-background ratio, maximizing the response functions. For the sake of clarity of our approach, and to avoid problems with statistical bias related to adaptive methods (which are related to downward statistical fluctuations and become severe if the statistics is low, see Ref. [202]), we choose a fixed patch with large signal-to-background ratio by inspection of the signal-to-background maps.

Clearly, the optimal region might in principle depend on the observed energy range and injection energy of electrons and positrons. But it turns out that for injection energies around 100 GeV - 10 TeV and high enough gamma-ray energies, the optimal region is always located south of the galactic center. This situation is illustrated in Fig. 5.9, which shows an example of a signal-to-background map for observed energies between 0.5 and 1 GeV, where the statistics is very good, for dark matter decay producing monochromatic electrons and positrons at 100 GeV. The map already suggests that the location of the optimal patch for constraining inverse Compton light from decaying dark matter actually lies in a region close to the Galactic center, located south of the Galactic plane.

Before discussing this further we note that an exception occurs for very high injection energies in the 1 - 10 TeV region, and low enough observed gamma-ray energies. There the overall ICS flux can actually be dominated by extragalactic ICS contributions from scattering between $e^+e^-$ pairs from dark matter decay with the CMB. In these cases the optimal patch would be located at the pole regions. The same holds in general true for prompt radiation from dark matter decay in and outside of the Galaxy, which has a much shallower angular profile than the galactic ICS component.

A more quantitative description of the situation can be found in the plots shown in Fig. 5.10. The black lines in the upper four panels show the signal-to-background ratio in different observed energy ranges as function of galactic latitude or longitude. The injection energy is now fixed to 1TeV, but the results stay qualitatively the same for other injection energies. As expected from the above discussion, at high energies (upper panels) the signal-to-background ratio is maximal in a region close to the galactic center, whereas at very low energies (middle panels) it is maximal at high latitudes, due to the extragalactic ICS component. The same dominance at high latitudes is also present in case of prompt radiation (lower panels).

[1] We cross-checked with our own analysis of the publicly available event data that this gives indeed the correct number counts at high energies.

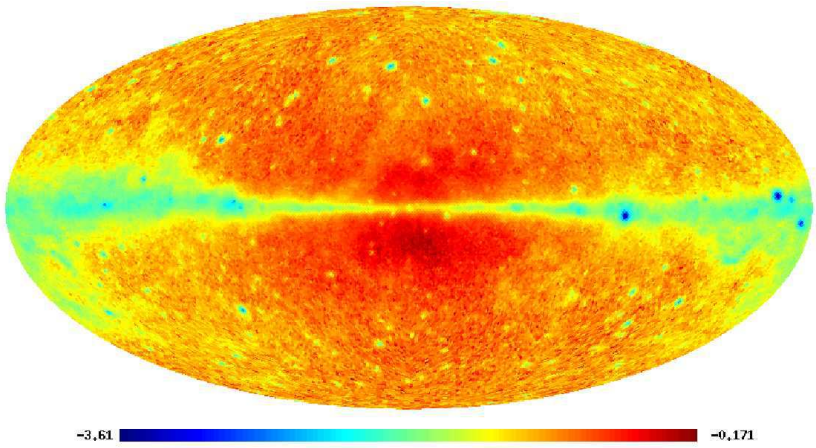


**Figure 5.9:** Signal-to-background map of ICS radiation from dark matter with $m_\chi = 200\,\mathrm{GeV}$, $\tau_\chi = 10^{26}\,\mathrm{s}$ decaying into $e^+e^-$ pairs, compared to the Fermi-LAT gamma-ray observations in the 0.5 - 1 GeV regime. Results hold for the L1 propagation model of Tab. 4.1. Note the logarithmic color scaling, warmer colors indicate larger signal-to-background.

For the derivation of the response functions we will concentrate on the patch $\mathcal{S}$ close to the galactic center and defined by $|l| < 20^\circ$ and $-18^\circ < b < -10^\circ$, which is marked by the colored region in Fig. 5.10. We checked that this patch indeed maximizes the obtained constraints when varying the patch boundaries, except for the very highest energy region (100 GeV - 300 GeV), where however the statistical error is large. For this patch, we construct the response functions by performing simulations injecting different mono-energetic electrons and comparing the results with observations according to Eq. (5.25).

Given that in some cases the optimal patch is actually located at the galactic pole regions we will also calculate and present bounds that come from comparing the preliminary extragalactic gamma-ray background as determined in Ref. [201] with the extragalactic ICS and isotropic prompt radiation component, see below.

### Response Functions without Foreground Subtraction

Our results for the response function are shown in Fig. 5.11 as function of the electron/positron injection energy, for the eight different energy ranges of Fermi-LAT skymaps from Ref. [13]. The highest energy range provides the strongest constraint on decaying dark matter with very hard electron/positron energy spectrum. However, for lower injection energies in the 100 GeV$-$1 TeV region, several energy ranges give actually roughly the same constraints.

To illustrate the large uncertainties related to inverse Compton radiation from dark matter decay inside the diffusive halo, we show in Fig. 5.12 the response func-

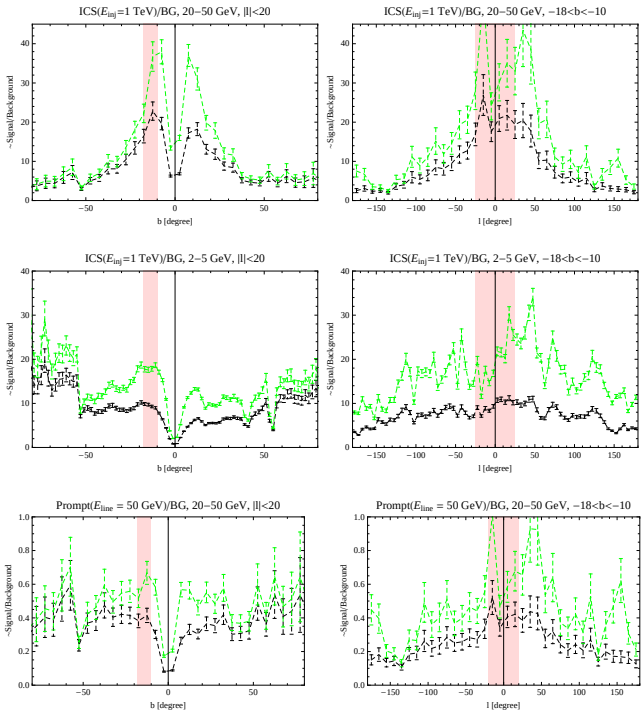


**Figure 5.10:** Signal-to-background ratios as function of galactic latitude (left panels) and longitude (right panels). The upper and middle panels correspond to pure ICS signal, the lower panels correspond to the pure prompt signal for comparison. Extragalactic and galactic radiation are taken into account. The black lines take into account as the whole observed signal, the green lines are obtained after subtraction of our reference model for the astrophysical component (Model L1). We find that the signal-to-background ratio of ICS radiation at higher gamma-ray energies is maximized in the region $\mathcal{S}$ defined by $|l| \leq 20^\circ$ and $-18^\circ \leq b \leq -10^\circ$, which is indicated by the light red shaded region.

tions based on the highest and lowest gamma-ray energy ranges for our three reference propagation models from Tab. 4.1. As emphasized before, the uncertainties on the response functions are dominated by the propagation model, especially for the lower energies, below 10 GeV injection energy, where also effects of reacceleration become relevant. For higher injection energies above 10-100 GeV, where the response functions become of $\mathcal{O}(1)$ and are hence relevant for the actual bounds, the uncertainties mainly stem from the height of the diffusion zone. In effect, high energy electrons and positrons lose energy in a very short time compared to the diffusion time, thus making the other details of the propagation irrelevant. The MAX propagation model gives the strongest constraints due to its large diffusive halo, whereas the MIN propagation model minimizes the constraints. Moreover, for the MAX model re-acceleration shifts lower energy electrons to higher energies. This effect is however only relevant for electrons below around 10 GeV, and thus

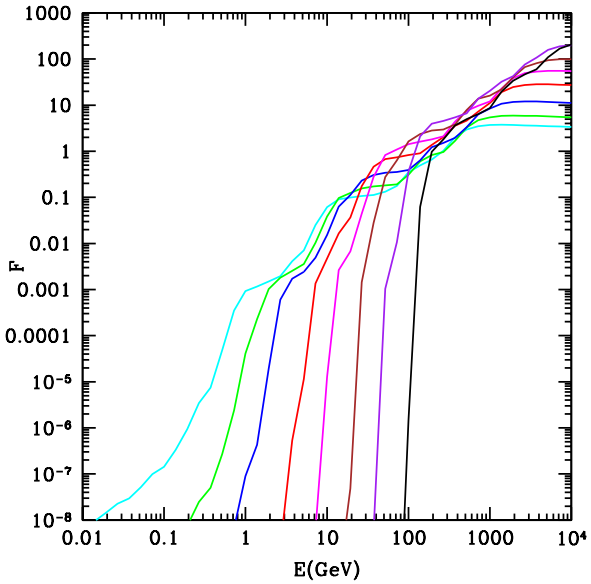


**Figure 5.11:** The response function $F_\gamma$ based on gamma-ray emission for the L1 model of Tab. 4.1. The response functions are derived from the eight gamma-ray energy ranges $0.5-1$ GeV, $1-2$ GeV, $2-5$ GeV, $5-10$ GeV, $10-20$ GeV, $20-50$ GeV, $50-100$ GeV, and $100-300$ GeV from top to bottom at left side, respectively. The underlying sky patch $\mathcal{S}$ is defined by $|l| \leq 20^\circ$ and $-18^\circ \leq b \leq -10^\circ$. Analytical fits to these curves are presented in Ref. [20]

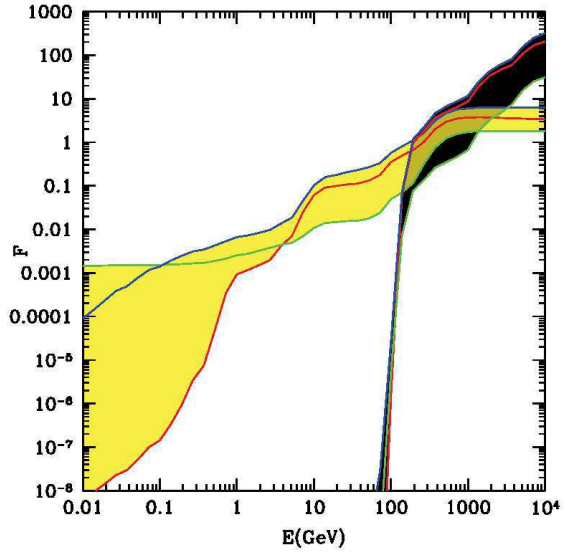


**Figure 5.12:** The propagation model dependence of the response function $F_\gamma$ based on our fixed patch for the gamma-ray energy range $0.5-1$ GeV (yellow band, curves extending to low energies) and $100-300$ GeV (black band, curves cutting off around 100 GeV). The width of the bands represents the variation within the MIN (green), L1 (red) and MAX (blue) propagation models of Tab. 4.1.

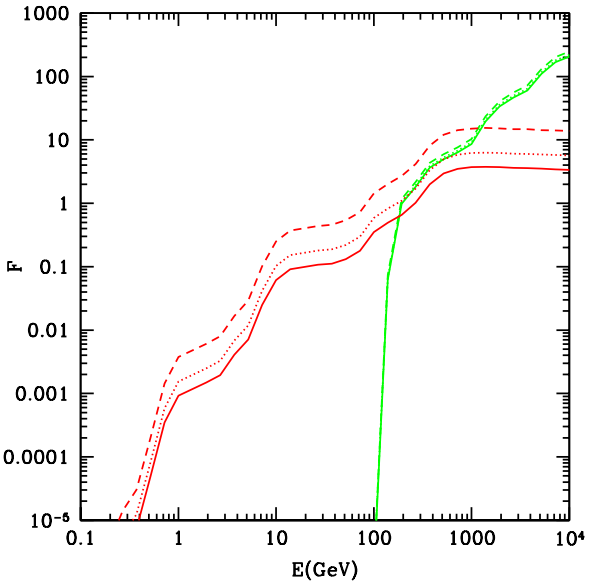


**Figure 5.13:** The dependence of the response functions on subtraction of astrophysical contributions to the gamma-ray signal. The response function $F_\gamma$ for the L1 model based on the raw observed map (solid) and on residual maps with gamma-rays from $\pi^0$ decay (dotted) and from all astrophysical processes (dashed, see text) removed. Red lines extending below 1 GeV are based on gamma-ray flux observed in the energy range $0.5 - 1$ GeV and green lines are based on the interval $100 - 300$ GeV.

increases the gamma-ray emission only in the MeV regime. Note that for the highest observed gamma-ray energy region (100-300 GeV), one clearly finds a sharp cut off at low injection energies since gamma-rays at such high energies cannot be produced from ICS of electrons/positrons injected at energies lower than 100 GeV.

### Response Functions with Subtraction of Astrophysical Foregrounds

The response functions $F_\gamma$ discussed so far are conservative because we did not attempt to subtract any astrophysical contribution to the gamma-ray flux. In order to understand the conventional astrophysical gamma-ray flux one needs to estimate the gamma-ray emission from different galactic components. The most relevant production channels are nucleus-nucleus (mainly proton-proton) photoproduction via $\pi^0$ decay and ICS and bremsstrahlung of cosmic-ray electrons and positrons. It is generally found [171] that hadronically generated gamma-rays dominate the flux at energies between 0.1 and 100 GeV and in the vicinity of the galactic plane, where most of the interstellar gas is located, while at lower and higher energies and at high latitudes ICS becomes comparable and can dominate. Bremsstrahlung is usually a subdominant component.

In Fig. 5.13 we show the response function for the L1 model based on residual gamma-ray maps obtained by subtracting gamma-rays produced via $\pi^0$ decay, ICS

and bremsstrahlung. In this foreground model the electron flux is adjusted to always lie below the electron flux observed by Fermi-LAT, with a spectral index of around -3.2. The subtraction affects the results at low energies. For example, at $E_e \sim 10\,\mathrm{TeV}$ the response functions based on gamma-ray fluxes observed at energies $0.5 - 1$ GeV are increased by a factor of around five when subtracting the total astrophysical "foreground" at these gamma-ray energies. Again at $E_e \sim 10\,\mathrm{TeV}$ the response functions based on gamma-ray fluxes observed at energies $100 - 300$ GeV are increased by $< 10\%$ and $\sim 15\%$ by the removal of gamma-rays originating from $\pi^0$ decay and from all astrophysical processes, respectively. This demonstrates explicitly that constraints on dark matter decay can be improved by taking into account the removal of astrophysical contributions mentioned above. At high energies the removal turns out to be quite insufficient which is at least in part related to the strong background contamination in the adopted data. This situation will be improved when data with better background rejection becomes available.

**Response Function for Annihilating Dark Matter.** Analogously, the response function approach can be extended to the annihilating dark matter with arbitrary annihilation spectra of $e^+e^-$. However, the uncertainties of response functions from dark matter annihilation are larger than the uncertainties in the decay case due to the dependence of the injection spectrum on the dark matter density squared rather than on the density itself. Recent N-body simulations shows that a large number of subhalos are embedded in our Galaxy, which are the relics of the formation history. The presence of substructure results in an enhancement of several orders of magnitude in annihilation signals with respect to a naive estimate for a smooth halo distribution. The Ref. [21] shows that the signals from substructures with masses down to $10^{-6} M_\odot$ dominate over the whole sky relative to the contribution from the smooth component. We find that, the annihilating dark matter with substructures can be well described by a smooth halo whose emissivity follows the distribution of subhalos since the diffusion effects of $e^+e^-$ can smooth the whole sky map; see Section 6.2 for details. Thus, for constructing the response function in annihilating dark matter with substructures scenario, one can replace the source term in Eq. (5.18) by

$$Q_\pm(\mathbf{r}, E_0) = f_N \frac{\rho_{sub}(\mathbf{r}) \langle \sigma v \rangle}{m_X^2} \delta(E - E_0)\,, \tag{5.28}$$

where $\rho_{sub}$ is radial distribution of subhalos. This normalization factor $f_N$ relies on both the radial and mass distribution of subhalos, with typical value of $f_N \approx 10 - 100 \mathrm{GeV/cm}^3$. If the radial distribution of subhalos is "unbiased" with respect to the density profile of the host halo, the same optimal directions or patches as derived before can be adopted directly.

## 5.6 Constraints on Dark Matter Models

The response functions (*i.e.* $F_r, F_p, F_\gamma$) developed in the previous sections can provide interesting constraints on any dark matter decay model. In the following, we apply these response functions to some concrete dark matter decay scenarios and obtain the constraints.

### 5.6.1 Constraints from Radio and Positron Signals

we discuss two simple examples that can be applicable to a number of realistic scenarios. Let us first consider an extremely simple case, direct decay into and electron/positron pair $X \to e^+e^-$ with branching ratio $b_e$. This will give conservative constraints for models that also allow decays into other fermion pairs such as [87, 203]. Moreover, it is certainly the simplest scenario that could account for the PAMELA excess [204, 205]. The spectrum of injected electrons is then $dN_\pm/dE_0 = b_e\delta(E_0 - m_X/2)$ and the constraints from the radio and positron fluxes are therefore

$$\frac{\tau}{10^{26}\ \mathrm{s}} \geq 2b_e \left(\frac{100\,\mathrm{GeV}}{m_X}\right) F_r(m_X/2) \quad ; \quad \frac{\tau}{10^{26}\ \mathrm{s}} \geq b_e \left(\frac{100\,\mathrm{GeV}}{m_X}\right) F_p(m_X/2)\ . \tag{5.29}$$

These bounds are shown on the left panel of Fig. 5.14 for all the different propagation models considered. We see that in general the positron data provide stronger constraints on this particular model than radio data, unless the dark matter mass is smaller than the PAMELA energy window i.e. $m_X < 11$ GeV, and at the same time there is no strong re-acceleration, as is the case in the DC and DR propagation models.

As a more realistic case, we have considered the scenario developed in Ref. [87]. This framework involves an extra U(1) gauge symmetry under which the standard model fields have no charge, a *hidden* U(1). Despite being secluded, interactions of this hidden sector with the standard model particles are realized through a tiny kinetic mixing [206] $\chi$ with the hypercharge $\mathrm{U}(1)_Y$. In particular, the hidden gauge boson $A'$ couples to all hypercharged particles with an additional suppression factor $\chi$ which can have extremely small values, cf. [207, 208, 209, 210]. If this hidden gauge boson accounts for the dark matter and has a mass around $\sim 200$ GeV it can decay into lepton, quark and $W$-boson pairs. Furthermore, if the $A'$ lifetime is of order $10^{26}$ sec, the gamma-rays and positrons resulting from the decay can explain the EGRET and PAMELA excesses. Convolving our response functions with the positron spectrum provided in [87] we find that, based on the continuum component alone, this model can be ruled out in the MIN, MED and MAX propagation scenarios due to the strong re-acceleration effects. The direct decay into $e^+e^-$, has a branching ratio ranging from 0.05 to 0.14 in the mass range 100 GeV $\geq m_{A'} \geq$ 300 GeV and is directly constrained by the left panel of Fig. 5.14[1].

[1] This scenario is somehow similar to the gravitino with R-parity violation described in [85, 211],

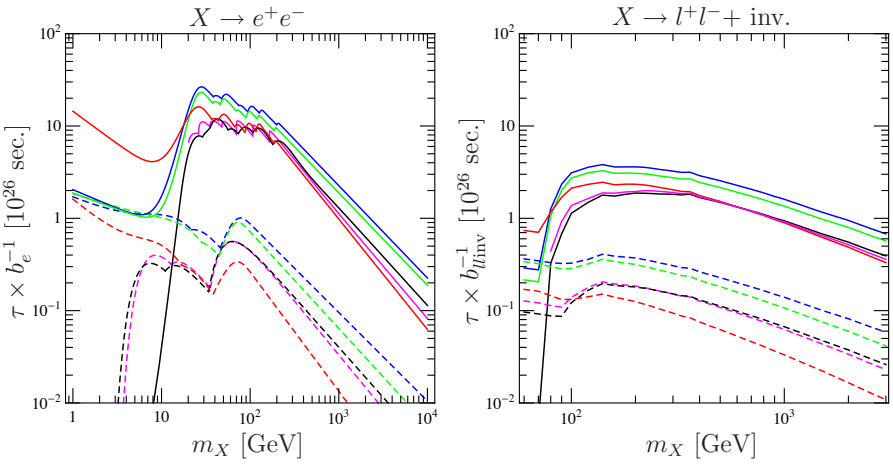


**Figure 5.14:** Bounds on a decaying dark matter particle for the decay mode $X \to e^+ + e^-$ (left panel) and $X \to l^+l^-$+invisible (right panel), see the text for details. The bound is on the lifetime of the dark matter particle divided by the branching ratio of the relevant mode. The color key for the propagation model is as in Fig. 5.4. Constraints from radio emission are dashed and from the PAMELA positron flux (with normalization given by the newest Fermi-LAT data) are solid. Each constraint line is based on either the synchrotron response function for the three frequencies (408 MHz, 1.420 GHz and 23 GHz) or on positron response function for the seven PAMELA energy bins.

Let us now consider the three body dark matter decay $X \to l^+ + l^-$+invisible where $l^\pm$ are Standard Model leptons and *invisible* stands for a nearly massless fermion ($m_X \gg m_{\mathrm{inv}}$). This decay arises for instance in supersymmetric versions of the hidden U(1) extension of the Standard Model outlined above, which also include the *hidden gaugino*, the supersymmetric partner of the hidden gauge boson [212]. As a concrete example consider the scenario recently described in [88]: Dark matter is made of bino-like neutralinos $\chi_1^0$ which are the lightest supersymmetric particles of the Standard Model sector. The neutralino mass is taken to be around $m_{\chi_1^0} = 300$ GeV which gives the correct relic dark matter abundance while the hidden gaugino $\tilde{X}$ is supposed to be a sub-dominant component of dark matter. If the hidden gaugino is lighter than the neutralino, the decay channel $\chi_1^0 \to l^+l^-\tilde{X}$ is available, whereas the reverse process $\tilde{X} \to l^+l^-\chi_1^0$ can be realized in the opposite case. These decays are mediated by heavy sleptons. Since squarks are usually heavier than sleptons, decays into quark pairs are suppressed.

In order to study bounds on this decay we focus onto the democratic case, i.e. equal branching ratio for decaying into lepton pairs of the three different families. We used PYTHIA [213] to simulate the final electron and positron decay spectra, and our response functions to give the bounds shown in the right panel of Fig. 5.14.

whereas the decay branching ratio of hidden gauge boson to the W boson is highly suppressed compared to the gravitino case.

These decay channels can be also found in other contexts like in [214] where a massive B-L gauge boson mediates the kinetic mixing, in grand unified theories [89, 215], or in general SUSY models with slightly broken R-parity with or without considering supergravity [216, 217, 218].

### 5.6.2 Constraints from Gamma-ray Signals

In the previous sections we constructed response functions for dark matter decays which are independent of the particles physics details of the decay and only depend on the spatial distribution of the dark matter particles and the propagation of the produced electrons and positrons. These response functions are very useful to estimate the constraints on dark matter decay based on gamma-rays produced by ICS within some specific dark matter model. However, within a given dark matter model gamma-rays can be produced not only as secondaries of electron and positron propagation in the Galaxy, but also as final-state, or prompt, radiation arising in the decay [151, 219]. For selected decay channels, we calculated the corresponding galactic and extragalactic prompt fluxes in our selected patch as described above and added them to the one described by the response functions in order to derive constraints that come from the total prompt + ICS radiation flux of different dark matter decaying models. Other works on constraints on the decaying/annihilating dark matter interpretation of the PAMELA positrons excess with recent Fermi-LAT gamma-data can be found in Ref. [202, 220, 221].

To illustrate the interplay of prompt and ICS radiation bounds, we show them in detail for the exemplary decay channel into $\mu^+\mu^-$ in Fig. 5.15. In this plot, each of the green lines corresponds to bounds coming purely from the galactic and extragalactic ICS radiation (calculated from our response functions) for the eight different energy regimes of the data. Regions below the green lines are excluded. On the other hand, the red lines show the corresponding bounds when only prompt radiation is taken into account. The thick black line is obtained when both radiation components are combined for each energy regime separately. All fluxes are calculated within our patch $\mathcal{S}$. As obvious from this plot ICS radiation bounds dominate at dark matter masses above a few 100 GeV.

In Fig. 5.16 we show our results for bounds on the four different decay channels into $\mu^+\mu^-\mu^+\mu^-$, $\mu^+\mu^-$, $\tau^+\tau^-$ and $b\bar{b}$ as examples with different amount of prompt and ICS radiation.[1] The first three decay modes can well fit the PAMELA/Fermi positron and electron data if the positron excess is interpreted in terms of decaying dark matter, and the preferred mass and lifetime regions are indicated by the blue blobs and red crosses.[2] We used the PYTHIA package [222] to derive the electron,

[1] The four-body decay into muons proceeds via two intermediate neutral scalar particles with masses of 1 GeV.

[2] The shown regions should be understood as typical masses and lifetimes that well fit the data.

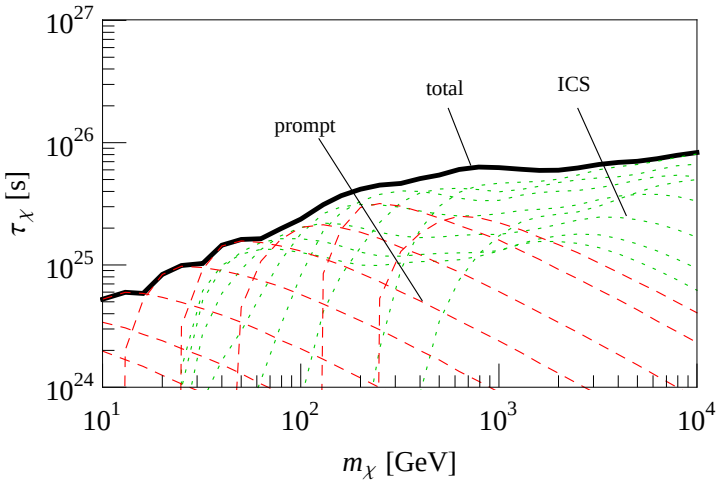


**Figure 5.15:** Constraints on decaying dark matter for the decay channel $\chi \to \mu^+\mu^-$ decoded into its different components. The thick solid line shows the overall bounds on mass and lifetime, *cf.* also Fig. 5.16. Green lines represent the constraint coming from the response function for ICS emission alone, whereas red lines are based on the prompt photon spectrum alone. Each of the eight lines corresponds to one of the observed gamma-ray energy ranges as denoted in the caption of Fig. 5.11.

positron and gamma-ray decay spectra.

In these plots the dashed-dotted (dotted) line shows the bounds obtained from ICS (prompt) radiation in our patch S alone, the thick solid line shows the bounds obtained when prompt and ICS radiation are combined. Furthermore, the bounds can be strengthened to the yellow region when the foreground model L1 is subtracted from the data.

It turns out that for decays into $\mu^+\mu^-$ pairs and four-body decay into $\mu^+\mu^-\mu^+\mu-$, the strongest constraints typically come from ICS rather than from the prompt radiation and the constraints could be improved by more than a factor of 2 for small masses and by a few 10% for large masses after removal of the gamma-ray emission from conventional astrophysical sources. In the case of decay into $\tau^+\tau^-$ and $b\bar{b}$ the prompt radiation alone already provides strong constraints, which can again be improved by subtracting galactic foreground as for the case of decay into muons.

Note that our patch S is optimized for ICS radiation. Prompt radiation from dark

---

We performed a $\chi^2$ test, keeping the electron background as a freely adjustable power-law with spectral index between -3.3 and -3.0, whereas the positron background is kept fixed as the one from "Model 0" in Ref. [223]. We include in the fitting procedure only the PAMELA data on the positron fraction above 10 GeV, as they should be less affected by solar modulation, and the Fermi-LAT and HESS $e^{\pm}$-data, for which we added the corresponding systematic and statistical errors in square. Since systematic errors are correlated, the obtained $\chi^2$ are relatively small, but in view of the large uncertainties in the electron background a more detailed fit is not reasonable. The blue regions correspond to $\chi^2/\text{dof} = 1$ and $\chi^2/\text{dof} = 0.75$, outside these regions the fits to HESS and Fermi-LAT become problematic.

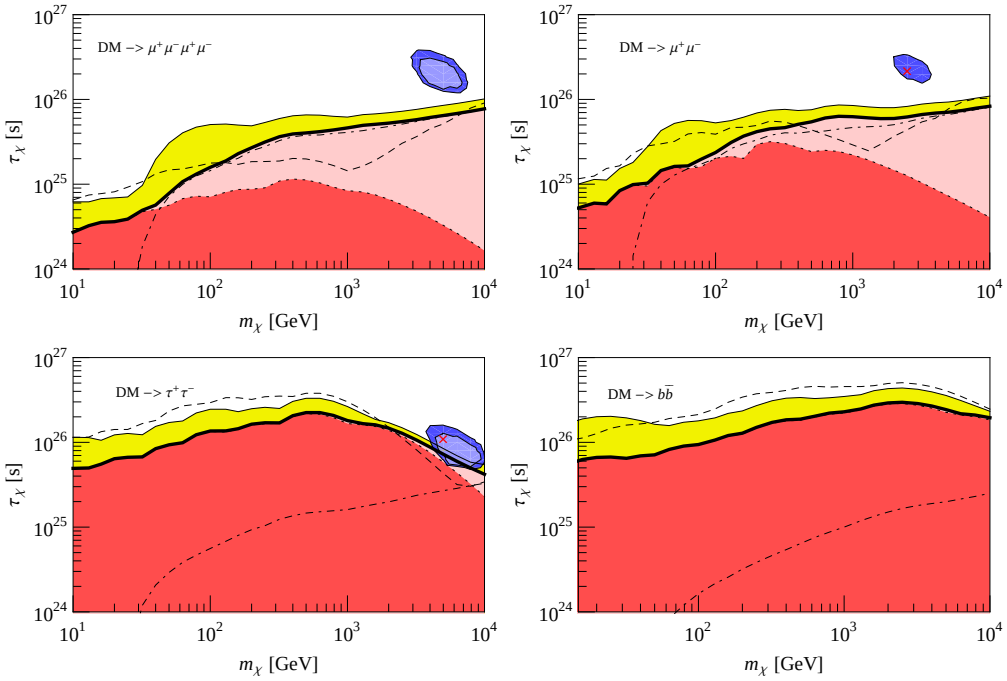


**Figure 5.16:** Bounds on different decay channels in the mass *vs.* lifetime plane. Regions below the thick solid line are excluded by combined ICS and prompt radiation in the L1 propagation model, whereas parameter space below the dashed-dotted (dashed) line is excluded due to ICS (prompt) radiation alone. The ICS constraints shown with the dashed-dotted lines are calculated from the response functions shown in Fig. 5.11. The constraints can be strengthened to the yellow light shaded region if the predictions of Model L1 for the galactic diffuse astrophysical foreground is subtracted. The blue blobs and red crosses (which are taken from Ref. [224]) show the parameters that well fit electron + positron fluxes observed by Fermi-LAT and HESS and the positron fraction observed by PAMELA as described in the text.

matter decay in general dominates at the galactic pole regions, as discussed above (in the actual data, this behavior is disturbed at high gamma-ray energies because of the large contamination of the data with isotropic cosmic-ray background). Following the slicing of the sky as proposed in Ref. [202], we can find for the highest energy bin a patch that actually increases our corresponding final state radiation bounds by around 70%.[1]

For comparison, we also show with the dashed lines in Fig. 5.16 the bounds that can be obtained by comparing the sum of extragalactic ICS radiation, extragalactic prompt radiation and the maximal isotropic part of the halo prompt radiation (which is identical to the flux from the Galactic anti-center) with the preliminary results for

[1]Using this adaptively determined patch, which is located at $10° \leq b \leq 20°$ and $0 \leq l \leq 10°$ and has only a few number counts, still does not allow to raise the bounds as high as shown in Ref. [202]. The difference might originate in the smaller energy bins used in [202], and the inclusion of data above 300 GeV.

the isotropic extragalactic gamma-ray flux as presented in Ref. [201]. Comparing these bounds, which already rely on a foreground subtraction, in case of decay into muons with the ones obtained from patch $\mathcal{S}$ after foreground subtraction shows that they are subdominant and become only relevant at very high masses. Our bounds are somewhat weaker than the ones found in Ref. [221], which is due to our inclusion of absorption effects and our more conservative treatment of extragalactic ICS radiation.

To conclude, under the conservative assumption of a propagation model with the height of the diffusion zone around 4 kpc, based on the Fermi-LAT data, we can severely constrain but not exclude models with dark matter decay into $\tau^+\tau^-$ that can explain the positron excess observed by PAMELA. Moreover, we find that analogous models with two- and four-body decay channels into $\mu^\pm$s remain essentially unconstrained by current observations. When our reference foreground model is subtracted the lower bounds on the lifetime in general increase by $\mathcal{O}(1)$ factors for dark matter masses below 1 TeV, and by 10-60% for masses above 1 TeV, which is however not enough to exclude the above channels in the parameter regime relevant for PAMELA. The bounds might improve by $\mathcal{O}(1)$ factors when data with better background rejection is used. For comparison we also calculated conservative bounds from the isotropic extragalactic gamma-ray background as inferred from the Fermi-LAT data, finding again that even the decay into $\tau^+\tau^-$ cannot be excluded in this way.

# Chapter 6

# Anisotropy Signatures from Dark Matter Annihilation

In this chapter we perform a statistical analysis of full-sky emission map to identify dark matter signatures. This approach can be promising if, e.g., one can identify features in the anisotropy power spectrum that characterize uniquely the dark matter spatial distribution with respect to other astrophysical sources, given that the astrophysical emission profile closely follows the matter density as opposed to the squared dark matter density. In this respect, one is interested in quantifying the anisotropy signatures from annihilating dark matter which can be different from those of astrophysical origin particularly at small scales. In Sect. 6.1, we perform analytic calculations for the anisotropic radio signatures from extragalactic dark matter annihilating into electrons and positrons and compare it with angular power spectrum of the astrophysical and cosmological radio background; In Sect. 6.2, we develop a numerical tool to compute ICS gamma-ray emission from Galactic dark matter annihilation into $e^+e^-$ pairs diffusing in the smooth host halo and the substructure halos with masses as low as $10^{-6}M_\odot$ and show that, unlike the total gamma-ray angular power spectrum observed by Fermi-LAT, the angular power spectrum from ICS is exponentially suppressed below an angular scale determined by the diffusion length of electrons and positrons.

## 6.1 Radio Signatures from Extragalactic Annihilation

In this section we evaluate the diffuse synchrotron emission from the electrons and positrons produced by dark matter annihilation in the cosmological distribution of dark matter halos. We compute both its overall intensity and its angular power spectrum as well as the distribution of visible dark matter annihilation sources as a function of apparent luminosity. We will find that comparing the resulting signals with other backgrounds and foregrounds under conservative assumptions allows one to test the annihilation cross sections close to the natural scale $\langle\sigma v\rangle \sim$

$3 \times 10^{-26}\,\mathrm{cm}^3/\mathrm{s}$.

### 6.1.1 Formalism

We consider a distribution of sources which emit a radio luminosity per frequency interval $L(\nu, \mathcal{P}, z)$ which depends on the parameter $\mathcal{P}$, the frequency $\nu$ and the redshift $z$. The energy flux per frequency interval and solid angle is then given by

$$J(\nu) = \int dz \frac{d^2V}{dz d\Omega} \int d\mathcal{P} \frac{dn}{d\mathcal{P}}(\mathcal{P}, z) \frac{(1+z)L[\nu_z, \mathcal{P}, z]}{4\pi d_L(z)^2}\,, \tag{6.1}$$

where for abbreviation we write $\nu_z \equiv (1+z)\nu$, $(dn/d\mathcal{P})(\mathcal{P}, z)$ is the co-moving volume density of objects per unit interval in the parameter $\mathcal{P}$, $d_L(z)$ is the luminosity distance, the factor $1+z$ comes from redshifting the frequency interval $d\nu$, and the co-moving volume per solid angle and redshift interval is

$$\frac{d^2V}{dz d\Omega} = \frac{d_L(z)^2}{(1+z)^2 H(z)} = \frac{r(z)^2}{H(z)}\,. \tag{6.2}$$

Here, for a flat cosmological geometry, the Hubble rate is

$$H(z) = H_0 \left[\Omega_{nr}(1+z)^3 + \Omega_\Lambda\right]^{1/2}\,, \tag{6.3}$$

$r(z) = \int_{t(z)}^{t(0)} (1+z)dt = \int dz'/H(z')$ is the co-moving distance and $t(z) = \int_0^z dz'/[(1+z')H(z')]$ is cosmic time as function of redshift.

In order to calculate the anisotropies we introduce an emissivity of squared power per frequency interval, $\mathcal{L}^2(\nu, k, z)$,

$$\mathcal{L}^2(\nu, k, z) = \mathcal{L}_1^2(\nu, k, z) + \mathcal{L}_2^2(\nu, k, z)\,, \tag{6.4}$$

which, similar to the approach in Ref. [225], we split into the two parts, $\mathcal{L}_1^2(\nu, k, z)$ and $\mathcal{L}_2^2(\nu, k, z)$. Both depend on the co-moving wavenumber $k$. The first part is essentially Poisson noise and corresponds to the sum over squared luminosities,

$$\mathcal{L}_1^2(\nu, k, z) = \int d\mathcal{P} \frac{dn}{d\mathcal{P}}(\mathcal{P}, z) \left[L(\nu_z, \mathcal{P}, z)|u(k, \mathcal{P})|\right]^2\,, \tag{6.5}$$

where in the following we define $\mathcal{F}_f(k) \equiv \int d^3\mathbf{r} e^{i\mathbf{k}\cdot\mathbf{r}} f(\mathbf{r})$ as the spatial Fourier transform of any function $f(\mathbf{r})$ and where $u(k, \mathcal{P}) = \mathcal{F}_u(k, \mathcal{P})$ is the Fourier transform of the spatial emission density $u(\mathbf{r}, \mathcal{P})$ of an individual source, normalized to unity, $\int d^3\mathbf{r} u(\mathbf{r}, \mathcal{P}) = 1$. The second contribution to Eq. (6.4) is determined by the correlation between sources,

$$\mathcal{L}_2^2(\nu, k, z) = P_{\mathrm{lin}}(k, z) \left[\int d\mathcal{P} \frac{dn}{d\mathcal{P}}(\mathcal{P}, z) L(\nu_z, \mathcal{P}, z) b(\mathcal{P}, z) |u(k, \mathcal{P})|\right]^2\,, \tag{6.6}$$

where $P_{\rm lin}(k,z) = \int d^3\mathbf{r} e^{i\mathbf{k}\cdot\mathbf{r}} (\delta\rho/\rho)(\mathbf{r},z)$ is the linear power spectrum of the density fluctuations $(\delta\rho/\rho)(\mathbf{r},z)$ and we have also introduced a bias factor $b(\mathcal{P},z)$ of the sources with respect to the density field. For the linear dark matter halo bias $b(M,z)$ appearing in Eq. (6.6) we adopt [226]

$$b(M,z) = 1 + \frac{\nu^2(M,z)}{\delta_c D(z)}\,, \tag{6.7}$$

whereas for the galaxy bias we simply use unity.

The angular power spectrum $C_l$ is given by

$$C_l = \left\langle |a_{lm}|^2 \right\rangle\,, \tag{6.8}$$

where

$$a_{lm} = \int d\Omega \left[J(\nu,\Omega) - \langle J(\nu)\rangle\right] Y^*_{lm}(\Omega) \tag{6.9}$$

in terms of the spherical harmonic functions $Y_{lm}(\Omega)$ and the intensity $J(\nu,\Omega)$ measured along direction $\Omega$. For a statistically isotropic sky this results in

$$C_l = \int dz \frac{d^2V}{dz d\Omega} \frac{(1+z)^2 \mathcal{L}^2\left(\nu_z, \frac{l}{r(z)}, z\right)}{[4\pi d_L(z)^2]^2}\,. \tag{6.10}$$

Using $d_L(z) = (1+z)r(z)$ and inserting Eq. (6.2) in Eqs. (6.1) and (6.10) finally gives

$$J(\nu) = \frac{1}{4\pi} \int \frac{dz}{(1+z)H(z)} \int d\mathcal{P} \frac{dn}{d\mathcal{P}}(\mathcal{P},z) L(\nu_z,\mathcal{P},z)\,, \tag{6.11}$$

and

$$C_l = \frac{1}{(4\pi)^2} \int dz \frac{\mathcal{L}^2\left(\nu_z, \frac{l}{r(z)}, z\right)}{d_L(z)^2 H(z)}\,. \tag{6.12}$$

Formally, for point-like sources, the integral over redshift in Eq. (6.12) is divergent at $z \to 0$. In practice this is regularized by the fact that the nearest source has some minimal distance and that one can subtract the most luminous point sources which are also the nearest sources. In addition, the integral is regularized by the spatial extent of the sources, represented by the factor $|u(k,\mathcal{P})|^2$ in Eqs. (6.5) and (6.6). The role of these effects in practical calculations will be discussed in Sect. 6.1.5.

### 6.1.2 Extragalactic Dark Matter Annihilation

For annihilation of dark matter with mass $m_X$ and phase space averaged annihilation cross section times velocity $\langle\sigma v\rangle$, $\mathcal{P}$ can be identified with the mass $M$ of dark matter halos. We then follow the approach of Ref. [34] and write

$$L(\nu,M) = \frac{\langle\sigma v\rangle}{2m_X^2} \mathcal{E}(\nu,M)\,, \tag{6.13}$$

where we define $\mathcal{E}(\nu, M)$ as a quantity which does not depend on annihilation cross section or mass of the dark matter particles,

$$\mathcal{E}(\nu, M) = \frac{\sqrt{3}e^3}{m_e} \int d^3\mathbf{r} \rho_h^2(\mathbf{r}) B(\mathbf{r}) \int_{m_e}^{m_X} dE \frac{Y_e(>E)}{P_{\rm syn}(E) + P_{\rm IC}(E)} F\left[\frac{\nu}{\nu_c(E)}\right] . \quad (6.14)$$

In Eq. (6.14), $e$ and $m_e$ are the electron charge and mass, respectively, $\rho_h(\mathbf{r})$ is the dark matter halo density profile, $B(\mathbf{r})$ is the local magnetic field strength, $Y_e(>E)$ is the multiplicity per annihilation of electrons and positrons with energies larger than $E$, $P_{\rm syn}(E) = 2e^4B^2E^2/(3m_e^4) = (16e^4\pi/3)u_BE^2/m_e^4$ is the total synchrotron emission power of one electron of energy $E$ in a magnetic field of strength $B$, corresponding to an energy density $u_B = B^2/(8\pi)$, and $P_{\rm IC}(E) = (16e^4\pi/3)u_\gamma E^2/m_e^4$ is the energy loss rate at energy $E$ due to inverse Compton scattering on a low energy photon field of energy density $u_\gamma$.

Furthermore, we use the function

$$F(x) = x \int_x^\infty K_{5/3}(y) dy \,, \quad (6.15)$$

in Eq. (6.14), with the critical frequency $\nu_c(E)$ defined in Eq. (5.7).

In the following we use the approximation [189]

$$F(x) \simeq \delta[x - 0.29] \quad (6.16)$$

such that Eq. (6.14) can be simplified to

$$\mathcal{E}(\nu, M) \simeq \frac{9}{8} \left(\frac{m_e^3}{0.29\pi}\right)^{1/2} \frac{Y_e[>E_c(\nu)]}{\nu^{1/2}} I(M) \quad (6.17)$$

where

$$I(M) = \int d^3\mathbf{r} \frac{\rho_m^2(\mathbf{r})}{(eB)^{1/2}(\mathbf{r})} \frac{1}{1 + u_\gamma(\mathbf{r})/u_B(\mathbf{r})} \,, \quad (6.18)$$

with the critical energy $E_c(\nu)$ in Eq. (5.10). In Eq. (6.17) we neglect the magnetic field dependence of $Y_e[>E_c(\nu)]$. For $m_X \gtrsim 100\,\text{GeV}$, $B \gtrsim$ a few $\mu$G and $\nu \sim 1\,\text{GHz}$, the parameters we are interested in, this is a good approximation because the critical energy $E_c(\nu_z) \lesssim m_X/10$. Typical values for these parameters are $Y_e \simeq 10$ [34]. This corresponds to a fraction $f_e \simeq 0.3$ of the total annihilation energy going into pairs. The energy fraction going into pairs of energy above $E$ can be expressed in terms of $Y_e(>E)$ as

$$f_e(E) = \frac{-1}{2m_X} \int_E^{m_X} dE' E' \frac{dY_e}{dE}(E') \leq 1 \,. \quad (6.19)$$

With the above expressions we can rewrite Eq. (6.11) as

$$J(\nu) = \frac{\langle\sigma v\rangle}{2m_X^2} \frac{9}{32\pi} \left(\frac{m_e^3}{0.29\pi\nu}\right)^{1/2} \int \frac{dz}{(1+z)^{3/2}H(z)} \int dM \frac{dn}{dM}(M, z) Y_e[>E_c(\nu_z)] I(M) \,. \quad (6.20)$$

Furthermore, we can redefine $\mathcal{L}_1^2$ and $\mathcal{L}_2^2$ from Eqs. (6.5) and (6.6) by extracting constant factors and write

$$\mathcal{L}_1^2(\nu, k, z) = \int dM \frac{dn}{dM}(M, z) \left(Y_e[> E_c(\nu_z)] I(M) |u(k, M)|\right)^2 \tag{6.21}$$

and

$$\mathcal{L}_2^2(\nu, k, z) = P_{\rm lin}(k, z) \left( \int dM \frac{dn}{dM}(M, z) Y_e[> E_c(\nu_z)] I(M) b(M, z) |u(k, M)| \right)^2 , \tag{6.22}$$

where $u(k, M)$ relates to the halo profile, $u(k, M) = \int d^3\mathbf{r} e^{i\mathbf{k}\cdot\mathbf{r}} \rho_h^2(\mathbf{r}) (eB)^{-1/2}(\mathbf{r})/I(M)$. With these quantities we can now write

$$C_l = \frac{81 m_e^3}{1024 \cdot 0.29 \pi^3 \nu} \left(\frac{\sigma v}{m_X^2}\right)^2 \int dz \frac{\mathcal{L}_1^2\left(\nu, \frac{l}{r(z)}, z\right) + \mathcal{L}_2^2\left(\nu, \frac{l}{r(z)}, z\right)}{(1+z) d_L(z)^2 H(z)} . \tag{6.23}$$

Details about the quantities that enter these expressions are given in Sect. 2.3.

**Limber approximation.** Eq. (6.23) can also be obtained as follows: Limber's equation relates the two-dimensional angular power spectrum $P_2(l)$ to the three-dimensional power spectrum $P_3(k)$ in the flat sky approximation [227]: Given a three-dimensional statistically random field $f(\mathbf{r}) = f(\Omega, r)$, one considers the observation at $\mathbf{r} = 0$ of the projection

$$P(\Omega) = \int dr \; w(r) \; f(\Omega, r) \tag{6.24}$$

with some given radial weight function $w(r)$, where $r$ is the co-moving distance. If the field $f$ fluctuates on scales much smaller than the characteristic scale over which $w(r)$ varies, then we have

$$C_l \simeq \int dr \frac{w^2(r)}{r^2} P_f(l/r, z(r)) \tag{6.25}$$

where $P_f(l/r, z)$ is the power spectrum of $\langle f(\Omega_1, r) f(\Omega_2, r)\rangle$ at the co-moving wavenumber $k = l/r$.

Neglecting the variation of the magnetic field $B$ within the halo regions contributing most to the annihilations, the radio intensity Eq. (6.20) along a given direction $\Omega$ can be written as

$$J(\nu, \Omega) = \frac{\langle \sigma v \rangle}{m_X^2} \frac{9 \rho_m}{64 \pi \nu^{1/2}} \left(\frac{m_e^3}{0.29 \pi e B}\right)^{1/2} \int dz \frac{(1+z)^{3/2}}{H(z)} Y_e[> E_c(\nu_z)] \frac{[1 + \delta(z, \Omega)]^2}{1 + u_\gamma/u_B} , \tag{6.26}$$

where $\rho_m = \Omega_m \rho_c$ is the average dark matter density at zero redshift, and $\delta = \delta\rho/\rho$ is the relative overdensity. Because the dominant contribution comes from the dark

matter halos, where $\delta \gg 1$, we can approximate $(1+\delta)^2 \simeq \delta^2$. Assuming a constant $B$ and a constant optical photon field of density $u_{\rm op} \simeq 5\,{\rm eV\,cm^{-3}}$, we can write the factor $(1+u_\gamma/u_B)^{-1} = [1+u_{\rm op}/u_B + u_0(1+z)^4/u_B]^{-1}$, where $u_0$ is the CMB energy density at $z=0$. This factor effectively cuts off the redshift integration at $z \simeq 2$. Since $E_c(\nu_z)$ varies little over this redshift range, we can then further simplify Eq. (6.26) to

$$J(\nu,\Omega) \simeq \frac{Y_e[>E_c(\nu)]\,\langle\sigma v\rangle}{m_X^2}\frac{9\rho_m^2}{64\pi\sqrt{eB\nu}}\left(\frac{m_e^3}{0.29\pi}\right)^{1/2}\int dz \frac{(1+z)^{3/2}\delta^2(z,\Omega)}{H(z)\left[1+\frac{u_{\rm op}}{u_B}+\frac{u_0}{u_B}(1+z)^4\right]}\,. \tag{6.27}$$

Comparing this with Eq. (6.24), we can use

$$f = \delta^2 - \left\langle\delta^2\right\rangle\,, \tag{6.28}$$

for the random field and the weight function is

$$w(z) = \frac{Y_e[>E_c(\nu)]\,\langle\sigma v\rangle}{m_X^2}\frac{9\rho_m^2}{64\pi\sqrt{eB\nu}}\left(\frac{m_e^3}{0.29\pi}\right)^{1/2}\frac{(1+z)^{3/2}}{1+\frac{u_{\rm op}}{u_B}+\frac{u_0}{u_B}(1+z)^4}\,. \tag{6.29}$$

The power spectrum $P_f(k,z)$ appearing in Eq. (6.25) is then the Fourier transform of the two-point correlation function of $f$ in real space. Following Ref. [228], $P_{\delta^2}(k,z)$ can be written as the sum of a one-halo and a two-halo term, $P_{\delta^2}(k,z) = P^{1h}_{\delta^2}(k,z) + P^{2h}_{\delta^2}(k,z)$, with

$$P^{1h}_{\delta^2}(k,z) = \int_{M_{min}}^{M_{\rm cut}(z)} dM \frac{dn}{dM}\left[\mathcal{F}_{\delta^2}(k,M,z)\right]^2 = \int_{M_{min}}^{M_{\rm cut}(z)} dM \frac{dn}{dM}\left(\frac{A_b\mathcal{F}_{\rho_h^2}(k,M,z)}{\rho_m^2(1+z)^6}\right)^2 \tag{6.30}$$

$$\begin{aligned} P^{2h}_{\delta^2}(k,z) &= P_{\rm lin}(k)\left[\int_{M_{min}}^{M_{\rm cut}(z)} dM \frac{dn}{dM} b(M)\mathcal{F}_{\delta^2}(k,M,z)\right]^2 \\ &= P_{\rm lin}(k)\left[\int_{M_{min}}^{M_{\rm cut}(z)} dM \frac{dn}{dM} b(M)\left(\frac{A_b\mathcal{F}_{\rho_h^2}(k,M,z)}{\rho_m^2(1+z)^6}\right)\right]^2\,, \end{aligned} \tag{6.31}$$

where $M_{\rm min}$ is the minimal halo mass and $M_{\rm cut}(z)$ is the halo mass corresponding to the apparent point source flux $S_{\rm cut}$ above which we consider the source to be resolvable and thus subtractable from the diffuse background. Furthermore, $A_b$ is a boost factor which accounts for possible substructure in the halos. The average of the clumping factor appearing in Eq. (6.27) is given by

$$\left\langle\delta^2(z)\right\rangle = \frac{A_b}{\rho_m^2(1+z)^6}\int_{M_{\rm min}}^{M_{\rm cut}(z)} dM\frac{dn}{dM} \times \int dV_h\,\rho_h^2({\rm r},M,z)\,, \tag{6.32}$$

where $dV_h$ is the halo volume element.

A generic form for the halo mass function $dn/dM$ appearing in the equations above was first proposed by Press & Schechter (PS) [40]; a modified version of this form is given by Sheth and Tormen [41] (ST). When comparing the results obtained from these two forms, we find differences by factors less than 2. Thus, we adopt the PS formula in our calculations.

Current knowledge of the dark matter density distribution mostly comes from N-body simulations. We use NFW halo profile [46] (see Sect. 2.3 for details) in our calculations. In this model the dark matter profile within each halo can be written as

$$\rho_h(r) = \frac{\Delta_c(z)}{3} \frac{c^3}{\ln(1+c) - c/(1+c)} \frac{\rho_m(z)}{r/r_s(1+r/r_s)^2} \,. \tag{6.33}$$

In addition, the minimal halo mass is still rather uncertain. The value $M_{\rm min} = 10^{-6}\,M_\odot$ [58] is close to the free-streaming mass [63, 84, 229], below which there are no fluctuations in the dark matter density to form a halo. Note that the magnetic field may be much smaller than micro Gauss scales in such small halos. In contrast, the value $M_{\rm min} = 10^6\,M_\odot$ roughly corresponds to the minimal mass of dwarf galaxies which are known to contain micro Gauss scale magnetic fields [230]. We, therefore, choose $M_{\rm min} = 10^6\,M_\odot$ as fiducial value in the following, noting that the dark matter signal would increase by only a factor about two for $M_{\rm min} = 10^{-6}\,M_\odot$. We will furthermore use $B = 10\mu$G as fiducial value for the magnetic field. This is a realistic value given that most annihilations occur in the densest regions where also magnetic fields are somewhat larger than typical average galactic fields.

The clumping factor is very sensitive to the concentration parameter, namely $\propto c^3$. How the concentration parameter depends on halo mass and redshift is still an open question. Conservatively, we use the parameterization in Eq. (2.10) because at $z \simeq 0$ it gives values $c \sim 70$ for the minimum halo mass which is significantly smaller than other parameterizations [57, 59].

Recent studies show that dark matter halos exhibit considerable substructure [67, 68, 69, 71, 231, 232, 233, 234, 235, 236, 237]. The total mass of these substructures only account for about 10% of the host halo, but they can give an extra boost factor $A_b \sim 10$ for dark matter annihilation. Some studies show that if one takes into account substructure and assumes a cuspy center slope [238, 239, 240], the theoretical prediction can well explain the excess of high energy positrons and the diffuse $\gamma-$ray background observed by the Heat [124, 241] and EGRET [117, 118] experiments, respectively. The subhalos follow a certain mass and redshift distribution which is still unknown. Therefore, to be conservative we assume the NFW halo model and simply parametrize any possible boost factor with the parameter $A_b \sim 10$. The substructures occur on small scales and do not influence the power spectrum in the range we are interested, $l \lesssim 10^4$.

### 6.1.3 Astrophysical Sources

For astrophysical sources, $\mathcal{P}$ can be identified with the radio luminosity $L_{\nu_0}$ at some fixed frequency $\nu_0$. Eq. (6.11) then simplifies to

$$J(\nu) = \frac{1}{4\pi} \int \frac{dz}{(1+z)H(z)} \int^{L_{\rm cut}(z)} dL_{\nu_0} L_{\nu_0} \frac{dn}{dL_{\nu_0}}(L_{\nu_0}, z) \frac{L(\nu_z)}{L_{\nu_0}} \,, \tag{6.34}$$

where $L_{\rm cut}(z) = 4\pi d_L(z)^2 S_{\rm cut}/(1+z)$ is the intrinsic luminosity corresponding to the apparent point source flux $S_{\rm cut}$ above which we consider the source to be resolvable and thus subtractable from the diffuse background. For the multipoles Eqs. (6.5) and (6.6) can then be written as

$$\mathcal{L}_1^2(\nu, k, z) = \int^{L_{\rm cut}(z)} dL_{\nu_0} L_{\nu_0}^2 \frac{dn}{dL_{\nu_0}}(L_{\nu_0}, z) \left[\frac{L(\nu_z)}{L_{\nu_0}} u(k, z)\right]^2 \tag{6.35}$$

and

$$\mathcal{L}_2^2(\nu, k, z) = P_{\rm lin}(k, z) \left[\int^{L_{\rm cut}(z)} dL_{\nu_0} L_{\nu_0} \frac{dn}{dL_{\nu_0}}(L_{\nu_0}, z) \frac{L(\nu_z)}{L_{\nu_0}} u(k, z) b(L_{\nu_0}, z)\right]^2 , \tag{6.36}$$

respectively. For the luminosity functions $dn/dL_{\nu_0}$ of normal and radio galaxies we will use the expressions given in Ref. [242].

### 6.1.4 Different Contributions to the Diffuse Radio Emission

The CMB dominates the radio sky at frequencies above $\simeq 1\,$GHz, whereas astrophysical sources such as normal galaxies and radio galaxies dominate at lower frequencies down to kHz frequencies [242]. Recently it was argued that synchrotron emission of strong intergalactic shocks can also significantly contribute to the diffuse extragalactic radio below 500 MHz [243, 244].

Using the formuli developed in Sect. 6.1.2, we now evaluate the contribution of synchrotron emission from pairs produced by dark matter annihilation in the magnetic fields of dark matter halos. We consider neutralinos as dark matter candidate, and for the following figures we assume a neutralino mass of 100 GeV and a total annihilation cross section of $\langle \sigma v \rangle = 3 \times 10^{-26}\,{\rm cm}^3/{\rm s}$, fixed for reproducing the correct relic density for thermal relics. We also assume that the average total number of electrons and positrons per annihilation is $Y_e \simeq 10$, and that the halo substructure implies a boost factor $A_b \simeq 10$. We compare the resulting dark matter signal with astrophysical contributions to the diffuse background that can be computed from the expressions in Sect. 6.1.3.

For astrophysical sources the diffuse radio background is likely dominated by normal galaxies and radio galaxies. To estimate the contributions from these sources, we follow Ref. [242], which use the observed correlation between the radio and infrared flux of galaxies. This approach assumes that the radio emission is related to

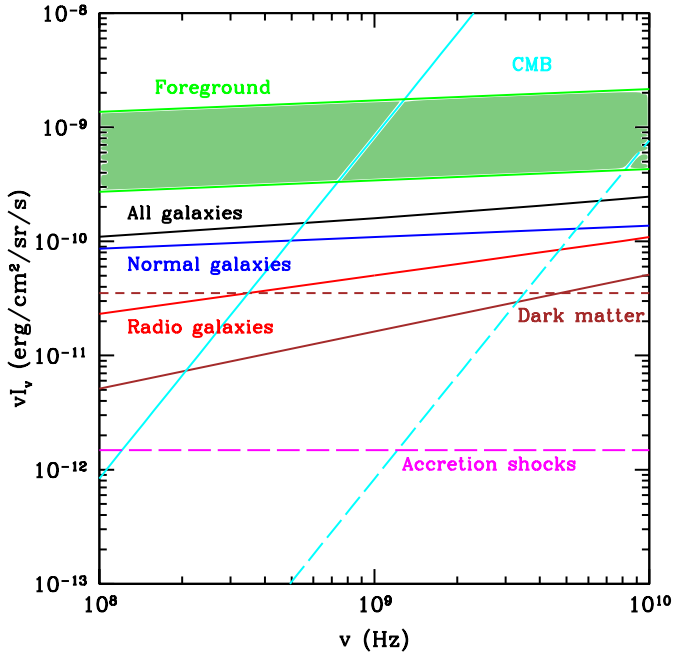


**Figure 6.1:** The average diffuse background flux intensity with no point-source removal. Contributions from normal galaxies (blue curve), radio galaxies (red curve), from radio and normal galaxies combined (black curve), and from a scenario for radio emission from galaxy cluster shocks (magenta curve) [244] (see text for the normalization) are compared to our fiducial dark matter annihilation scenario with $m_X = 100\,\mathrm{GeV}$, $\langle\sigma v\rangle \sim 3\times10^{-26}\,\mathrm{cm}^3/\mathrm{s}$, $A_b = 10$, $B = 10\,\mu\mathrm{G}$, $M_{\rm min} = 10^6\,M_\odot$ (brown curves). Here, the solid brown curve is for $Y_e = 10$, while the dashed brown curve is for $Y_e(E) \simeq m_X/E$. Also shown is the CMB background (cyan solid curve) as well as its subtractable part, determined by uncertainties of the absolute CMB temperature (dotted cyan curve). The Galactic foreground at Galactic latitude $b > 20^\circ$ is shown as the green band within uncertainties.

the star formation and is sensitive to the redshift evolution of the sources, but can explain the observed radio background quite well.

Following the above assumptions, in Fig. 6.1, we show the different contributions to the average diffuse radio intensity. For astrophysics sources, normal galaxies contribute more than radio galaxies. This is because although the individual radio galaxy is brighter than a normal galaxy on average, this is overcompensated by the larger number of normal galaxies. Also shown in Fig. 6.1 is a possible contribution from intergalactic shocks [243, 244] normalized such that its angular power spectrum is comparable to the one of the Galactic foreground, see Sect. 6.1.5.

Of course, the CMB absolutely dominates the radio sky in the wide range from $\nu \simeq 1\,\mathrm{GHz}$ to a few hundred GHz [93], and above these frequencies Galactic foregrounds such as dust emission dominates. Since the CMB is a black body radiator its contribution to the solid angle averaged radio flux can be subtracted up to the

uncertainty of its average absolute temperature. Currently the CMB temperature is measured to $2.725 \pm 0.001$ K [245]. We convert this temperature uncertainty into an intensity of CMB confusion noise. Fig. 6.1 shows that this confusion noise dominates other astrophysical backgrounds and the diffuse signal of our fiducial dark matter scenario at $\nu \gtrsim 4\,\mathrm{GHz}$. At lower frequencies the dark matter signal $\nu J(\nu)$ tends to decrease as $\sqrt{\nu}$ for $Y_e \simeq \mathrm{const.}$, see Eq. (6.27), whereas the background from normal galaxies tends to be flat, see Fig. 6.1. There is thus an optimal window at frequencies $\nu \sim 1\,\mathrm{GHz}$ where dark matter annihilation signatures can be detected and where self-absorption is negligible. Constraints on dark matter parameters can, therefore, only be established for annihilation cross sections about a factor ten higher than the fiducial cross section required for thermal dark matter. Also Fig. 6.1 shows that these foregrounds tend to dominate the astrophysical backgrounds and the dark matter signal in the fiducial scenario.

Can we test the properties of dark matter more powerfully? The absolute CMB temperature is difficult to measure more precisely than to the current permille level, because of inevitable systematic errors. Small-scale temperature fluctuations $\Delta T/T \sim 10^{-5}$ have been seen by the COBE and WMAP satellites because temperature differences can be measured more precisely since systematic errors cancel in measurements of temperature differences. Furthermore, if the Galactic foregrounds have a smooth directional dependence, they may pose less of a contamination when considering the anisotropy of the radio sky. We, therefore, consider in the following the angular power spectra of the radio sky in order to see if it can provide further tests of dark matter properties.

### 6.1.5 Extragalactic Anisotropy Signatures

Since the diffuse average radio flux provides only one number at a given frequency to compare with other astrophysical and cosmological backgrounds, potentially much more information is contained in the angular power spectrum. For example, the power spectrum as a function of angular scale tends to be different for dark matter annihilation and astrophysical sources because the contribution of the latter to the diffuse radio flux is dominated by fewer bright sources. Our goal in this section is whether this can provide dark matter signatures or constraints on mass and annihilation cross section.

Before calculating the angular power spectra, we discuss their qualitative behaviors. The angular power spectrum $C_l = C_l^{1h} + C_l^{2h}$ can be divided into one-halo ($C_l^{1h}$) and two-halo ($C_l^{2h}$) terms, corresponding to the two contributions Eqs. (6.5) and (6.6) to Eq. (6.4), and thus to Eq. (6.12). The two-halo term arises from the correlation between distinct halos which is described by the linear power spectrum. The one-halo term represents correlation within the same halo. Both one-halo and two-halo term are proportional to $|u(k, \mathcal{P})|^2$, the square of the Fourier transform of the spatial emission profile. At large angular scales, $|u(k, \mathcal{P})| \sim 1$, such that $C_l^{1h}$ is essentially independent of $l$. The one-halo term is thus sometimes called Poisson noise. At scales comparable to the size of the source, $|u(k, \mathcal{P})|^2$ starts to become sup-

pressed. Therefore, both one-halo and two-halo terms are expected to be suppressed for multipoles $l$ larger than the typical distance to the source divided by the linear source size. The two-halo term is furthermore proportional to the linear power spectrum which is also suppressed for co-moving wavenumbers $k \gtrsim 0.03\,\mathrm{Mpc}^{-1}$. Therefore, the ratio of the two-halo term to the one-halo term is suppressed for $l \gtrsim 0.03\,\mathrm{Mpc}^{-1} r_\mathrm{H} \simeq 100$, where $r_\mathrm{H} \simeq 3000\,\mathrm{Mpc}$ is the Hubble scale. The one-halo term eventually dominates at very small angular scales.

In Eq. (6.12), for point-like sources, formally the one-halo term $C_l^{1h}$ would diverge for $z_\mathrm{min} \to 0$, whereas the two-halo term Eq. (6.6) is regularized by the linear power spectrum $P_\mathrm{lin}(k, z)$, which is suppressed at large $k = l/r(z)$. This is because the flux of nearby sources of a given luminosity diverges. We can ignore such sources because they can be identified as individual bright sources and be removed from the background flux in actual observations. We can remove sources with intrinsic luminosity $L_\mathrm{cut}(z) \geq 4\pi d_L(z)^2 S_\mathrm{cut}/(1+z)$, corresponding to the point-source sensitivity $S_\mathrm{cut}$ of the telescope. Alternatively, one can regularize Eq. (6.12) by integrating from some finite minimum distance corresponding to the typical distance to the nearest source, $r_\mathrm{min} \sim 1\,\mathrm{Mpc}$. Furthermore, Eq. (6.12) is also formally regularized at $z_\mathrm{min} \to 0$ by the spatial extent of nearby sources, described by $|u(k, \mathcal{P})|^2$. For the NFW profile, the mass of the halo within distance $r$ from the halo centre increases as $r^2$ up to $r = r_s$, and then increases logarithmically between $r_s$ and $r_v$ since $\rho_h(r) \propto r^{-3}$, see Eq. (6.33). Therefore, the dominant contribution to the halo mass comes from $r < r_s$. Similarly, for $r < r_s$ the annihilation signal increases as $r$, but between $r_s$ and $r_v$ increases only as $r_s^{-3} - r^{-3}$. Assuming the emission traces $\rho_h$ for astrophysical emission processes and $\rho_h^2$ for dark matter annihilation, the Fourier transforms of these dependencies then give $u(k, \mathcal{P}) \propto k^{-\gamma}$ for $k \gg r_s^{-1}$, with $\gamma = 2$ for astrophysical emission and $\gamma = 1$ for dark matter, see Appendix A for more details. Since $k = l/r(z)$, and thus $|u\,[l/r(z), \mathcal{P}]\,|^2 \propto r(z)^{2\gamma}$, the one-halo term in Eq. (6.12) diverges only for $\gamma \leq 0.5$. Therefore, under our assumptions for the emission profile, Eq. (6.12) is convergent even without cut-offs in either $r_\mathrm{min}$ or the apparent luminosity. Since nevertheless in particular the one-halo term is quite sensitive to nearby sources, in the following we study its dependence on $S_\mathrm{cut}$ and $r_\mathrm{min}$.

Fig. 6.2 shows the dependence of the two-halo term on $S_\mathrm{cut}$. According to Eq. (6.6), the two-halo term scales with the square of the average flux. Since the apparent luminosity of radio galaxies can be of the order of a Jansky ($1\,\mathrm{Jy} = 10^{-23}\,\mathrm{erg\,cm^{-2}\,Hz^{-1}\,s^{-1}}$), the two-halo term from radio galaxies starts to decline when we cut sources being less luminous than a critical luminosity below a Jansky. In contrast, the contribution of normal galaxies which are much less luminous than radio galaxies starts to decline only when we cut sources more luminous than $\simeq 10\mu\mathrm{Jy}$. The contributions of dark matter halos to the dark matter annihilation signal is basically unaffected by any source removal, even to luminosities down to $\sim 1\mu\,\mathrm{Jy}$. This is easy to explain: In our fiducial scenario the largest dark halos of about $10^{14}\,M_\odot$ produce only about $1.3 \times 10^{38}\,\mathrm{erg/s}$ at 2 GHz from dark matter anni-

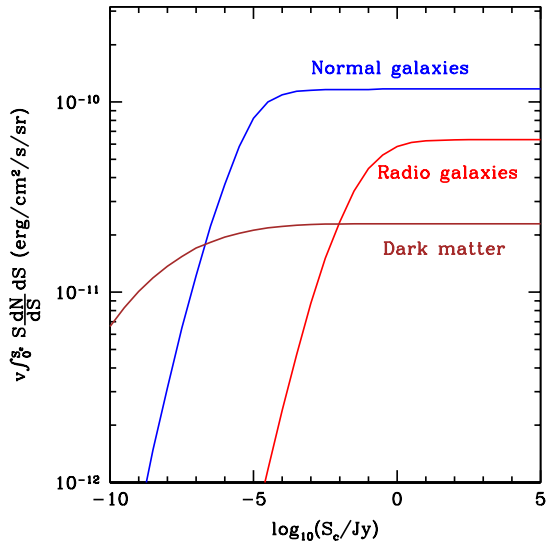


**Figure 6.2:** The cumulative contribution of sources of apparent luminosity $S$ smaller than $S_{\rm cut}$ to the two-halo term at 2 GHz. The red, blue and brown lines represent the contribution from radio galaxies, normal galaxies, and dark matter (fiducial scenario with $Y_e = 10$), respectively.

hilation, far less than the typical radio luminosity of galaxies of about $2 \times 10^{40}$ erg/s. As a result, removing bright sources increases the contribution of dark matter annihilation to the two-halo term relative to the contribution from astrophysical sources.

Next we discuss the one-halo term. The one-halo term is more sensitive to the cut-offs in apparent luminosity $S_{\rm cut}$ and to the minimal distance $r_{\rm min}$ than the two-halo term because of two reasons: First, the two-halo term Eq. (6.6) is the square of an integral of luminosities, whereas the one-halo term Eq. (6.5) is essentially Poisson noise and thus proportional to an integral of squared luminosities, which makes the contribution from bright sources more important. Second, the two-halo term is further regularized by the linear power spectrum at large $k = l/r(z)$. In Fig. 6.3 we show the cumulative contribution of sources dimmer than $S_{\rm cut}$ to $C_l^{1h}$. Similarly to the two-halo term shown in Fig. 6.2, the contribution of radio galaxies and ordinary galaxies decreases rapidly below $\simeq 1$ Jy and 10 $\mu$Jy, respectively, whereas the contribution of dark matter annihilation is affected less by source removal. Nevertheless, the contribution of bright sources is now much larger than for the two-halo term, as expected, and the one-halo term continues to rise with inclusion of brighter sources. On the other hand, practically one should cut off the integral at some minimal distance $r_{\rm min} \simeq 1$ Mpc within which there are essentially no bright sources. Since sources at small distance appear bright, the cut-off in luminosity and minimal distance is of course to some extent degenerate, as confirmed by Fig. 6.3. For radio galaxies, removal above $\simeq 10^5$ Jy is equivalent to restricting to distances larger than 1 Mpc. For ordinary galaxies, cutting at a minimal distance $r_{\rm min} = 1$ Mpc is equivalent to removing sources brighter than 0.1 Jy. Since observational sensitivities are

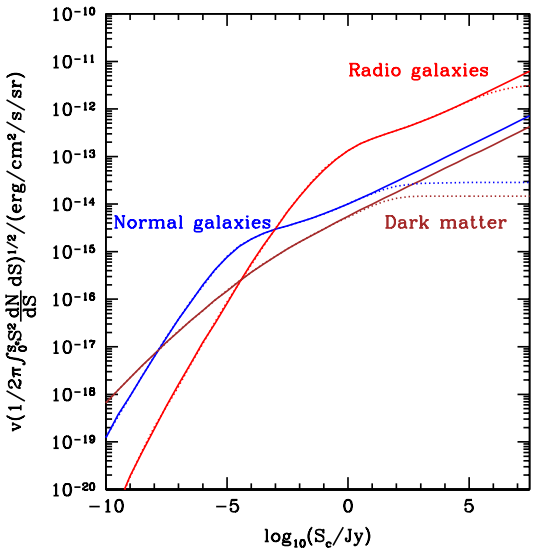


**Figure 6.3:** The cumulative contribution of sources of apparent luminosity $S$ smaller than $S_{\rm cut}$ to the one-halo (Poisson) term at 2 GHz. The solid and dotted curve represent the cases of $r_{\rm min} = 0$ and $r_{\rm min} = 1$ Mpc, respectively. Color keys are as in Fig. 6.2.

considerably better than these luminosities, cutting at $r_{\rm min} \simeq 1\,$Mpc does, therefore, not introduce any significant uncertainties. Note that in Fig. 6.2 dark matter dominates the two-halo terms if all sources above $\simeq 0.1\mu\,$Jy are removed, while in Fig. 6.3 it would dominate the one-halo terms only for unrealistically small cut-off luminosities $\lesssim 1\,$nJy. This is because the one-halo term is much more sensitive to bright sources than the two-halo term and because the dark matter contribution consists of dimmer sources than ordinary astrophysical sources.

The angular power spectra of the radio background at 2 GHz produced by galaxies and by our fiducial dark matter scenario are shown in Figs. 6.4, 6.5, and 6.6 for different source removal cuts. Based on the above discussion, the qualitative behavior of the one- and two-halo terms can be easily understood: In Fig. 6.4 we assume galaxies to appear point-like and we remove sources brighter than 0.1 mJy. The one-halo terms from these sources thus increase proportional to $[l(l+1)]^{1/2}$ in the above figures. The same applies to the one-halo term of the dark matter contribution for $l \lesssim 10^4$, corresponding to angular scales $\theta \simeq \pi/l \gtrsim 0.02°$. At smaller angular scales the power spectrum is suppressed by the inner structure of the dark matter halos. We can estimate this critical scale as follows: The one-halo term is dominated by the brightest halos which correspond to the largest and nearest halos. In our fiducial scenario, the annihilating dark matter in the largest halos can emit a radio flux of $\sim 7 \times 10^{28}\,{\rm erg\,s^{-1}\,Hz^{-1}}$ at 2 GHz, such that the minimum co-moving distance is $r \simeq 830\,$Mpc, $z \simeq 0.2$ if sources brighter than 0.1 mJy are removed. The scale $r_s$ for the corresponding $10^{14}\,M_\odot$ halo is about 0.21 Mpc. This corresponds to a multipole $l \simeq \pi r/r_s \simeq 1.2 \times 10^4$. This simple estimation is consistent with our

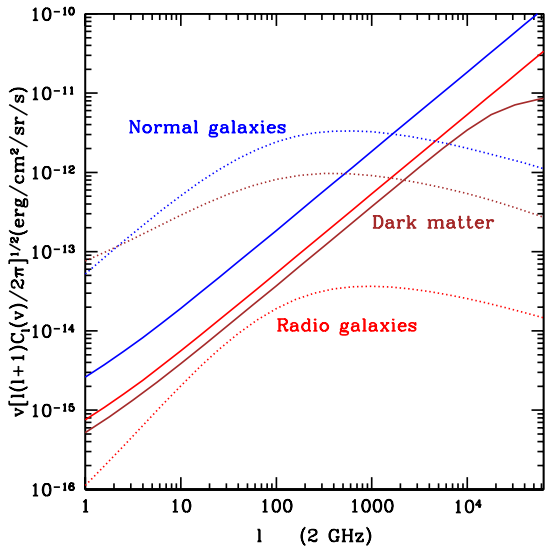


**Figure 6.4:** Angular power spectra of various components at 2 GHz. Solid lines and dotted lines represent the one-halo and two-halo terms, respectively. We assume the astrophysical sources to be point-like. The minimal dark matter halo mass is $M_{\rm min} = 10^6\,M_\odot$. Sources at distances below $r_{\rm min} = 1\,$Mpc, and of apparent luminosity above $S_{\rm cut} = 0.1\,$mJy were removed. Color keys are as in Fig. 6.2.

detailed calculation shown in Fig. 6.4.

Figs. 6.4, 6.5, and 6.6 show that for radio galaxies the one-halo term is always larger than the two-halo term at all multipoles, as expected because of the high luminosity of radio galaxies. For dark matter and normal galaxies, the two-halo term dominates at small $l$. The dependence of the angular power spectrum on $l$ can potentially be used to discriminate the dark matter signal from astrophysical contributions: For $l \lesssim 3 \times 10^3$, the annihilation power spectrum looks significantly flatter than the signal from normal galaxies. In other words, at large angular scales, the annihilation signal has relatively more power. This can be understood as follows: After cutting bright sources, many more dim nearby annihilation sources than galaxies contribute. In addition, at large redshift the synchrotron emission from dark matter annihilation is suppressed by the increased inverse Compton scattering rate on the CMB, see Eq. (6.29). The two-halo term is proportional to $P_{\rm lin}(k)$ which peaks at $\simeq 0.03\,{\rm Mpc}^{-1}$, corresponding to $l \simeq 0.03\,r(z)/{\rm Mpc}$. The on average smaller distance to the dark matter halos then translates into relatively more power at small $l$.

In Fig. 6.5, we take into account the spatial extent of the radio emission of galaxies. We assume the luminosity profiles of galaxies to be roughly proportional to the dark matter density profile with the halo mass is obtained from the relation between mass and bolometric luminosity [246].

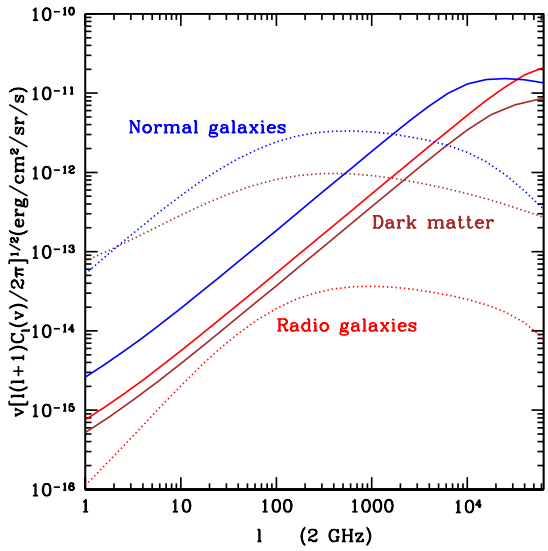


**Figure 6.5:** Same as Fig. 6.4, but assuming the emission profile of the astrophysical sources follows an NFW profile. Sources with luminosities above $S_{\rm cut} = 0.1\,\mathrm{mJy}$ are again subtracted.

For normal galaxies we use the relation [246]

$$M = 14\,\frac{L_{60}\nu_{60}}{L_{sun}}\,\frac{\Omega_m}{\Omega_b}\,M_\odot\,, \tag{6.37}$$

where $L_{60}$ is the luminosity at 60 microns, and $\nu_{60} \sim 5000$ GHz is its frequency, and $L_\odot \sim 3.9 \times 10^{33}\,\mathrm{erg/s}$ is the solar bolometric luminosity. For radio galaxies we simply adopt their typical mass of about $10^{12}\,M_\odot$ to estimate the Fourier transform of the their density profile.

As a result, for normal and radio galaxies the one-halo term starts to drop for $l \gtrsim 6000$ and $l \gtrsim 2.5 \times 10^4$, respectively. Compared to the dark matter signal, the suppression thus sets in at slightly smaller $l$ for normal galaxies, but only at larger $l$ for radio galaxies. For normal galaxies this is due to the more extended emission profile which more closely follows the density as opposed to the squared density in case of dark matter. This is also reflected by the Fourier transform of the emission profiles shown in Fig. A.1. For radio galaxies this effect is overcompensated by the fact that they are much brighter such that after cutting bright nearby sources, their average distance is much larger where their angular extent appears smaller.

Since future radio detectors such as SKA [101] can reach point flux sensitivities of $\sim 1\mu$Jy, we show the power spectra of the background remaining after a corresponding luminosity cut in Fig. 6.6. Since the two-halo term from dark matter annihilation is insensitive to such luminosity cuts whereas the contribution from galaxies decreases rapidly, as shown in Fig. 6.2, the relative contribution of dark matter annihilation increases and gives rise to a flatter power spectrum at moderate $l$.

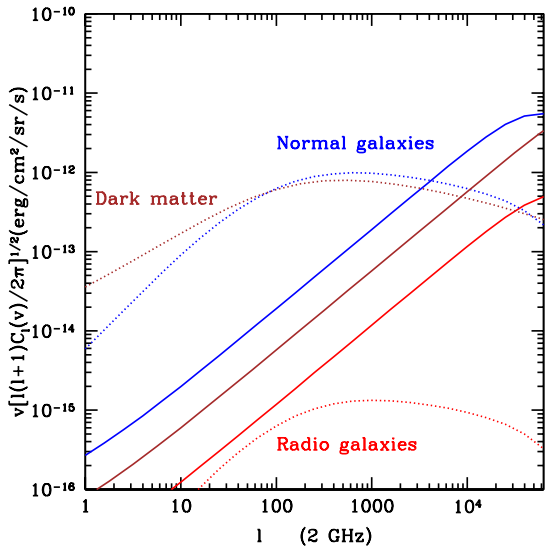


**Figure 6.6:** Same as Fig. 6.5, but subtracting sources above $S_{\rm cut} = 1\,\mu$Jy.

We now have to compare the cosmological background power spectra discussed so far with other potential contaminations. Fig. 6.7 compares the signals from ordinary and radio galaxies and from our fiducial dark matter scenario with the power spectra of the CMB and of the Galactic foreground at high Galactic latitude. The power spectrum of the Galactic foreground is not very well measured and we represent its uncertainties as a green band in Fig. 6.7. At high Galactic latitude below 10 GHz local foreground fluctuations dominate over the CMB power spectrum which is why the CMB anisotropy measurements are performed above 20 GHz. Concerning annihilation signatures of dark matter with mass $m_X \gtrsim 100\,$GeV in the angular power spectrum of the radio sky, the optimal frequency band is around 2 GHz. At higher frequencies, the synchrotron emission of electrons produced from dark matter annihilations cuts off due to Eq. (5.10) and the CMB signal increases. At lower frequencies, synchrotron emission by Galactic electrons dominates the power spectrum even at high Galactic latitude [247, 248, 249, 250]. Around 2 GHz, Galactic synchrotron emission always dominates, whereas free-free emission is a factor few smaller.

Also shown in Fig. 6.7 is a possible signal from intergalactic shocks [244]. Since its normalization is rather uncertain, we normalized it such that it is comparable to the average estimate of the Galactic foreground. The thermal SZ effect [251] is another characteristic contamination caused by hot ionized gas in galaxy clusters and filaments outside of clusters [252]. Since it dominates at small angular scales, $l \gtrsim 3000$, and at high frequencies above 30 GHz, we can neglect this effect here.

As can be seen from comparing Fig. 6.5 and 6.6 and from Fig. 6.7, future radio telescope arrays sensitive around $\nu \sim 2\,$GHz, with their higher point flux sensitivities should allow to further reduce the contribution from galaxies, whereas for $l \lesssim 6000$ the dark matter contribution is hardly changed by removing still fainter sources.

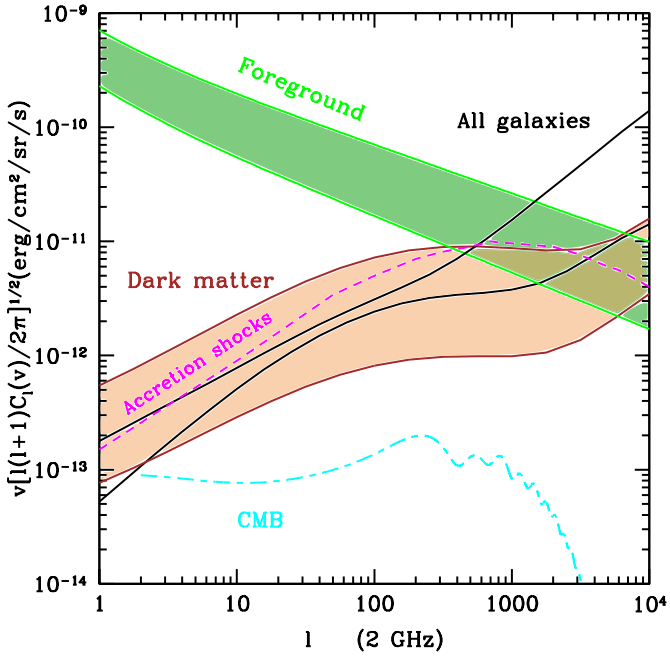


**Figure 6.7:** Angular power spectra of the radio sky at 2 GHz compared with various estimates of the Galactic foreground at Galactic latitude $b > 20°$ (green shaded region) and the CMB (cyan curve). The brown band represents the annihilation spectrum, where the upper and lower ends correspond to $F_{\rm dm} = 10$ and $F_{\rm dm} = 1$, respectively, see Eq. (6.38), and from which halos brighter than 0.1 mJy were removed. The black-dotted and black-solid curves represent the total signal from normal and radiogalaxies, for luminosity cuts $S_{\rm cut} = 10\,{\rm mJy}$ and $S_{\rm cut} = 0.1\,{\rm mJy}$, respectively. Also shown is a possible contribution from intergalactic shocks [244], normalized such that its angular power spectrum is comparable to the Galactic foreground.

This can be understood from the fact that the dark matter signal is dominated by the two-halo term which is insensitive to $S_{\rm cut}$ for $S_{\rm cut} \gtrsim 1\,{\rm nJy}$, see Fig. 6.2. This shows that for dark matter annihilation the distribution of $l(l+1)C_l$ is nearly flat for $200 \lesssim l \lesssim 2000$. At smaller $l$ the power spectrum is dominated by Galactic foregrounds and at larger $l$ the one-halo term from galaxies grows rapidly. The most sensitive range $200 \lesssim l \lesssim 3000$ should be accessible to present and future radio telescopes with their high angular resolution. The SKA will have a sensitivity of about $6 \times 10^{-13}\,{\rm erg\,cm^{-2}\,sr^{-1}\,s^{-1}}$ in the units of the above figures.

We conclude that the power spectrum from dark matter annihilation tends to be flatter than other contributions because of an interplay of the following effects:

- The astrophysical signals are dominated by fewer and much brighter sources than the dark matter annihilation signal which consists of many faint sources. For $S_{\rm cut} = 0.1\,{\rm mJy}$, the two-halo term dominates for $l \lesssim 10^3$ for both the signals from galaxies and from dark matter annihilation. In addition, the dark matter signal is significantly flatter in that angular range, i.e. it has relatively

more power at small $l$. This is because the two-halo term is proportional to the linear power spectrum whose peak in wavenumber for the on average closer and dimmer dark matter annihilation sources translates into smaller $l$ at these luminosities.

- For $l \gtrsim 10^4$, the inner spatial structure of the galaxies and dark matter halos becomes important. The inner structure tends to suppress the power spectra, but the exact angular scale at which these effects become important depends on the halo size, the profile of the emission and source luminosity cut-off.

- The various components evolve differently with the Universe expansion. For example, at high redshift inverse Compton scattering on the CMB tends to suppress synchrotron emission in dark matter halos, whereas astrophysical sources such as radio galaxies tend to be more active at $z \simeq 3$.

### 6.1.6 Dark Matter Constraints

We can now scale the dark matter signal to parameter values different from the fiducial scenario, by multiplying with the factor

$$F_{\rm dm} \equiv \left(\frac{A_b}{10}\right)\left(\frac{Y_e}{10}\right)\left(\frac{\langle\sigma v\rangle}{3\times10^{-26}{\rm cm^3 s^{-1}}}\right)\left(\frac{100{\rm GeV}}{m_X}\right)^2\left(\frac{10\,\mu{\rm G}}{B}\right)^{1/2} \tag{6.38}$$

We caution that a boost factor as high as $A_b \simeq 10$ has not been verified in all dark matter structure simulations and that the average magnetic field $B$ could be significantly smaller than $10\mu$G if many small-scale subhalos contribute. However, smaller values for $A_b$ and $B$ partially compensate in Eq. (6.38) so that one could still obtain observable signatures as long as $B$ is large enough to produce emission at GHz frequencies, see Eq. (5.10).

If we choose $F_{\rm dm} = 10$ (upper end of brown band in Fig. 6.7) and $S_{\rm cut} = 0.1\,$mJy, the annihilation spectrum dominates over other cosmological backgrounds for $100 \lesssim l \lesssim 10^4$ and should become distinguishable from the Galactic foreground. Note that this foreground is likely further reduced close to the Galactic poles. In this situation it should thus be possible to disentangle the rather flat power spectrum of the dark matter annihilation signal from other contributions in the range of $200 \lesssim l \lesssim 3000$. We can thus assert that radio observations are sensitive to $F_{\rm dm} \gtrsim 10$ with some dependence on the source luminosity cut-off $S_{\rm cut}$. Note that the dark matter signal shown in Fig. 6.7 does not strictly scale with $F_{\rm dm}$ because it depends on sources dimmer than $S_{\rm cut}$, here chosen as 0.1 mJy. However, since few brighter dark matter halos contribute, the signal scales with $F_{\rm dm}$ in first approximation.

One can also compare observed radio source counts as a function of apparent point source flux with predictions for astrophysical sources and dark matter annihilation sources. This is done in Fig. 6.8 for the same parameters as used in Fig. 6.7. This establishes the constraint $F_{\rm dm} \lesssim 10$. In contrast, Fig. 6.7 provides dark matter signatures for future measurements but currently does not allow to put a constraint

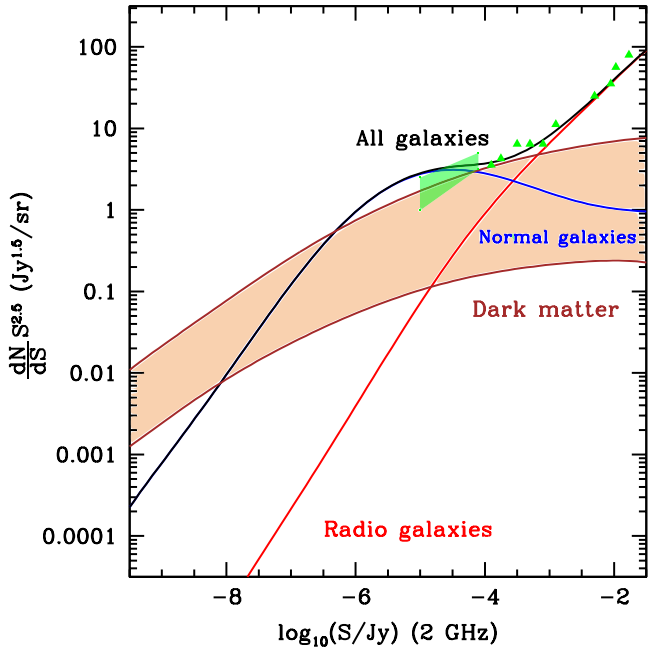


**Figure 6.8:** Observed radio source counts $(dN/dS)S^{2.5}$ as function of apparent radio flux $S$ compared with predictions for normal galaxies (blue curve), radio galaxies (red curve), and annihilations from dark matter halos (brown band, for $1 \leq F_{\rm dm} \leq 10$). Green shaded region and triangles are data from Ref. [253].

on $F_{\rm dm}$ because of the uncertainties in the Galactic foreground spectrum. Note that a future observational extension of the source count spectrum in Fig. 6.8 to apparent luminosities $S \lesssim \mu$Jy will provide an additional test for dark matter which predicts a shallower source count distribution than astrophysical sources.

We have not computed the contribution from dark matter annihilations in our own Galaxy to the anisotropic radio flux in the present work. However, we know from Refs. [254, 255] that for our fiducial values for cross section and mass, at least the smooth halo component does not lead to fluxes higher than current observations from WMAP. The contribution from Galactic substructures is probably more model dependent than our cosmological flux which apart from an overall boost factor depends only on the host halo distribution and effectively averages over a much larger ensemble of halos. This can also be seen from Ref. [82] where the predictions of the gamma-ray flux from Galactic dark matter annihilations varied over orders of magnitude.

## 6.2 ICS Gamma-ray Signatures from Galactic Annihilation

The ICS radiation from energetic electron and positron pairs produced by annihilation of dark matter can generates unique gamma-ray signatures. In this section we study the gamma-ray anisotropies produced by this "secondary" emission, which can be regarded as a new target for indirect searches of signatures induced by Galactic substructure halos. The important point is that the properties of the angular anisotropies for emission from secondary electrons and positrons will be different in general than for prompt emission, because the former will be affected by propagation effects in the Galaxy. In fact, by adopting a spatial diffusion model typical for high energy electrons and positrons in the Galaxy, we will show that the angular power spectrum is suppressed at small angular scales corresponding to the distance diffusively traveled by the charged particles during their energy loss time. As a result, for a typical dark matter model with mass of 1 TeV and a canonical thermal freeze-out cross section $3 \times 10^{-26}\mathrm{cm}^3/\mathrm{s}$, the angular power spectrum from ICS peaks at large angular scales, contrary to the gamma-ray angular power spectrum obtained from a simple analysis of the publicly available Fermi-LAT data.

### 6.2.1 Formalism

For the diffuse gamma-ray emission we are more interested in the column density of electrons,

$$\sigma_e(l,b,E) = \int_0^{l_{max}} d\ell \; n(\mathbf{r},E)\,, \tag{6.39}$$

than in the local space density of electrons. The observer is located at the solar system. In galactic coordinates, a point in cartesian coordinates $(x,y,z)$ at a distance $\ell$ from the observer is given by

$$x = \ell \cos b \cos l, \tag{6.40}$$
$$y = \ell \cos b \sin l, \tag{6.41}$$
$$z = \ell \sin b\,, \tag{6.42}$$

where $l$ and $b$ are the galactic longitude and latitude, respectively. We truncate the integral in Eq. (6.39) at the edge of the diffusion zone, beyond which particles are not confined, $z_{max} = L$ or $\ell_{max} = L/|\sin b|$. The line-of-sight integral can directly act on the free Green's function in Eq. (4.16),

$$\begin{aligned} G^{\sigma}_{\rm free}(l,b,\mathbf{r}',\lambda_D) &= \int_0^{\ell_{\rm max}} d\ell\, G_{\rm free}(\ell\mathbf{n},\mathbf{r}',\lambda_D) = \\ &= \frac{e^{[(\mathbf{n}\cdot\mathbf{r}')^2-(\mathbf{r}')^2]/\lambda_D}}{2\pi\lambda_D^2 b(E)}\left[\mathrm{erf}\left(\frac{\ell_{\rm max}-\mathbf{n}\cdot\mathbf{r}'}{\lambda_D}\right)-\mathrm{erf}\left(\frac{-\mathbf{n}\cdot\mathbf{r}'}{\lambda_D}\right)\right], \end{aligned} \tag{6.43}$$

where we have defined the unit-vector $\mathbf{n} \equiv \mathbf{r}/\ell$. The Green's function satisfying the boundary condition is thus

$$G^{\sigma}_{2L}(l, b, \mathbf{r}', \lambda) = \sum_{i=-\infty}^{\infty} (-1)^i G^{\sigma}_{\rm free}(l, b, \mathbf{r}'_i, \lambda)\,. \tag{6.44}$$

The column density of electrons therefore reads

$$\sigma_e(l, b, E) = \frac{1}{b(E)} \int d^3\mathbf{r}' \int_E^{\infty} dE'\; G^{\sigma}_{2L}\left[l, b, \mathbf{r}', \lambda_D(E, E')\right] Q(\mathbf{r}', E')\,. \tag{6.45}$$

In the limit of $\lambda_D \gg r_s$, where $r_s$ is the scale radius of the subhalo profile, the subhalo can be regarded as a point-like source. Eq.( 6.45) can then be simplified to

$$\sigma_e(l, b, E) = \sum_k \frac{1}{b(E)} \int_E^{\infty} dE'\; G^{\sigma}_{2L}\left[l, b, \mathbf{r}_k, \lambda(E, E')\right] j_k(\mathbf{r}_k), \tag{6.46}$$

where $j_k(E) = \int d^3\mathbf{r}\; Q_k(\mathbf{r}, E)$ for a given subhalo source $Q_k$ located at $\mathbf{r}_k$. For the largest subhalos with masses larger than $\simeq 10^9 M_\odot$, their radius $r_s$ can be somewhat larger than the diffusion length $\lambda_D$. Nevertheless, their contribution to the total flux is a factor $\sim 10^4$ smaller than the flux from the smaller subhalos. Therefore, neither the mean intensity nor the dimensional angular power spectrum (see Sect. 6.2.2) relies significantly on the distribution of electrons in the largest subhalos. As a result, for our purposes we can apply Eq. (6.46) to all subhalos even if $r_s > \lambda_D$.

**Propagation Model.** The propagation of high energy electrons and positrons in the turbulent Galactic magnetic field can be described as a diffusion-energy loss equation (see chapter 4 for details), which can be simplified to

$$\frac{\partial n_e}{\partial t} = \boldsymbol{\nabla} \cdot \left(D(E, \mathbf{r})\, \boldsymbol{\nabla} n_e\right) + \frac{\partial}{\partial E}\left(b(E, \mathbf{r})\, n_e\right) + Q(E, \mathbf{r})\,, \tag{6.47}$$

for the electron-positron number density $n_e$, neglecting the convection and re-acceleration terms which are only relevant for electrons and positrons below 10 GeV [179]. With the assumption that spatial diffusion and energy loss coefficients are spatially independent, for a given source distribution and boundary conditions, the propagation equation can be solved analytically (see expressions in Sect. 4.3). In this section, we adopt the widely used MED model (see Tab. 4.1) which, compared to other models, i.e. the MIN and MAX models. The MIN and MAX propagation models would decrease and increase the predicted gamma-ray fluxes roughly by a factor of three and two, respectively. However, we verified that the shape of the angular power spectrum predicted by these three propagation models is basically the same. Since in this study we mainly focus on a new "suppression" feature in angular power spectrum of the gamma-ray component from ICS, we will use the MED model in the following calculations.

**Dark Matter Model.** For dark matter annihilation, we simply assume mono-energetic injection of the positron and electron in case of CP conservation, i.e. $dN_e/dE = 2\delta(E - m_\chi)$. We choose $m_\chi = 1$TeV, which can well fit the PAMELA excess [152] while not in conflict with gamma-ray observations by Fermi-LAT [194]. Finally, we use $\langle\sigma v\rangle = 3\times10^{-26}\mathrm{cm}^3/\mathrm{s}$ to reproduce the correct relic density for thermal freeze-out. By convolving our results for the gamma-ray spectra with the pair energy, our computational approach can be easily adapted to pair spectra different from mono-energetic injection, such as from dark matter annihilating into $\mu^\pm, \tau^\pm$, and $W^\pm$.

**Energy Losses.** At energies above 10 GeV, the dominant energy losses are synchrotron radiation and inverse Compton scattering (ICS) on the interstellar radiation field. Therefore, in the Thomson limit we write $b(E, \mathbf{r}) = b_0\, E^2$ [for a more complicated treatment of energy loss see Ref.[180]], where $b_0 = 3\times10^{-16}$GeV/s for starlight (SL) , infrared (IR), CMB photons and a magnetic field of $3\mu$G. The ISRF can be approximately characterized as a superposition of three blackbody-like spectra with different temperatures and normalization factors relative to a true black-body emitter: one for the CMB with $T_{CMB} = 2.73$K, for the IR with $T_{IR} = 40.61$K and for the SL with $T_{SL} = 3800$K [194]. The typical normalization of the SL and IR fields of radiation depends on the position in the Galaxy. The averaged normalizations of ISRF photon densities per energy used in this study are $8.9\times10^{-13}, 1.3\times10^{-5}$ and 1 for SL, IR and CMB, respectively [194]. Although these normalizations are valid only in the region with latitude $20^\circ > |b| > 10^\circ$, we have checked that changing the normalization of the ISRF affects the gamma-ray emissions only weakly because an increased emission is partly compensated by a decrease of the density of electrons and positrons as energy losses increase. We also verified that the deviation from the detailed numerical simulation with Galprop [159] is less than a factor of two for a realistic spatial distribution of the ISRF [256].

**Angular Power Spectrum.** The angular power spectrum of the emission maps can be calculated by using the public HEALPix package [257]. We define the dimensionless quantity $\delta I(\psi, E_\gamma) \equiv (I(\psi, E_\gamma) - \langle I\rangle)/\langle I\rangle$ as a function on the sphere, which can be expanded in spherical harmonics $Y_{lm}$ as

$$\delta I = \sum_{l=0}^{l_{max}} \sum_{m=-l}^{l} a_{lm} Y_{lm}(\psi)\,, \tag{6.48}$$

where I($\psi$) describes the gamma-ray intensity in the direction $\psi$. The *dimensionless* angular power spectrum of $\delta I$ is given by the coefficients

$$C_l = \frac{1}{2l+1} \sum_{m=-l}^{l} |a_{lm}|^2\,. \tag{6.49}$$

Note that the measured dimensional amplitude $C_l^I$ of the total angular power spectrum in units of intensity squared can be obtained by multiplying the dimensionless angular power spectrum of a given component, $C_{l,i}$, with its mean intensity squared, $\langle I_i \rangle^2$ and summing over the components,

$$C_l^I = \sum_i \langle I_i \rangle^2 C_{l,i} \,, \tag{6.50}$$

where in our case the sum basically runs over the contributions of the smooth host halo, the subhalo distribution and other astrophysical foregrounds and backgrounds. Here we assumed that the different contributions are uncorrelated.

### 6.2.2 Numerical Scheme

In numerical calculations, taking into account subhalos down to masses $\sim 10^{-6} M_\odot$ in the angular power spectrum would require the generation of $\sim 10^{16}$ subhalos within the diffusion zone in a given Monte Carlo realization. This is not very practical and severely limits the number of realizations one can simulate. Thus, we need to develop a sound scheme to circumvent these computational limits. Here we take advantage of a few simple facts: (i) two terms contribute to the fluctuations anisotropies; the one-halo term which is Poissonian noise and the two-halo term due to the cross-correlation of substructure arising from their radial distribution within the host halo. (ii) the small but numerous substructure halos dominate the mean flux, contribute only to the two-halo term because their Poissonian noise is suppressed as $N(M)^{-1/2}$; (iii) analogously, large and relatively rare substructures contribute mostly to the one-halo term, but negligibly to the two-halo term. There is thus a dividing mass of substructures, $M_0$, below which the contribution to the anisotropies are negligible. The value of this mass depends on the assumed radial distribution of the substructure halos (see below). In any case, though, it turns out that halos with $M < M_0$ have a characteristic radius, $r_s$, which is much smaller than the diffusion length of the gamma-ray emitting electrons, i.e. $\lambda_D \gg r_s$. Thus, effectively all halos below $M_0$ have the same image on the sky in ICS with a characteristic size given by $\lambda_D$. This further simplifies our calculations because besides minor poissonian noise, the angular power spectrum from subhalos with $M < M_0$ is just given by the emission profile obtained by convoluting the subhalo spatial distribution with the image of one subhalo which is mass-independent for $M < M_0$. Thus the contribution from subhalos with $M < M_0$ can be taken into account straightforwardly. Basically we generate a distribution of subhalos with mass in the decade $10^{-6} - 10^{-5} M_\odot$ to obtain the full-sky map. The number of subhalos is typically much smaller than $N(M)$, with $M$ in the above range, but sufficiently large that the angular power spectrum has converged. The intensity of the map can be rescaled to the value appropriate for $N(10^{-6} < M/M_\odot < 10^{-5})$ halos. The map contributed from halos in all other mass decades up to $M_0$ can be obtained by simply rescaling the intensity appropriate for halos in that mass decade. Alternatively, the calculation can be repeated for halos in all other mass decades up to $M_0$.

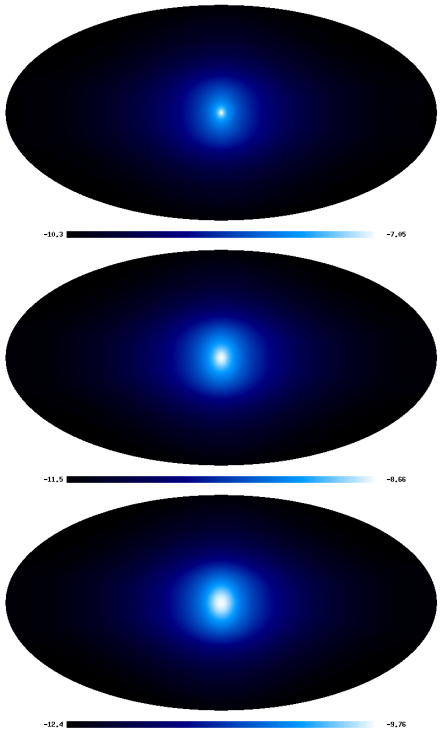

**Figure 6.9:** Sky maps of gamma-ray emission in Galactic coordinates at 1 GeV (top-left), 10 GeV (top-right) and 100 GeV (bottom) due to ICS from the host halo. The color scaling is logarithmic, and the unit is $1/\mathrm{s}/\mathrm{cm}^2/\mathrm{sr}$.

We complete the calculation by adding the contribution of subhalos with mass $M > M_0$, which can now be done with a direct Monte Carlo simulation.

Specifically, we find that our calculation of the angular power spectrum reaches convergence when we use at least $10^5$ subhalos for each mass decade from $10^{-6} M_\odot$ to $M_0$ within the diffusion zone, provided that we use $M_0 = 10^4 M_\odot$ for the unbiased radial distribution and $M_0 = 10^2 M_\odot$ for the anti-biased case.

Note that this method can not be applied to the angular power spectrum of the direct annihilation component since in this case the profile of the emitting region depends on the profile of each subhalo rather than on the identical diffusion length which just depends on the energy of electrons and positrons for all subhalo masses. In the following, we make use of the formalism derived in the previous section to compute the gamma-ray mean intensity map and associated anisotropy power spectrum due to both the smooth host halo component and the substructure halos. We also study how the map morphology and anisotropies depend on the radial distribution of subhalos and of the gamma-ray energy. Finally, we discuss the detectability by Fermi-LAT.

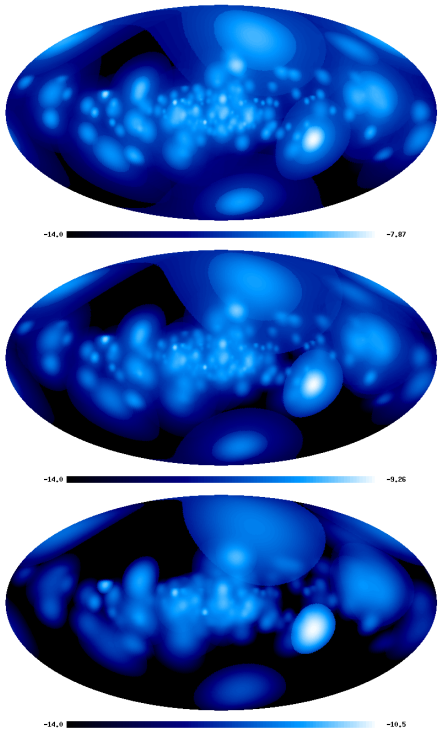

**Figure 6.10:** Sky maps of gamma-ray emission in Galactic coordinates at 1 GeV (top-left), 10 GeV (top-right) and 100 GeV (bottom) due to ICS from one realization of subhalos for the unbiased radial distribution and a minimum subhalo mass of $10^6 M_\odot$. The color scaling is logarithmic, and the unit is $1/\mathrm{s/cm^2/sr}$.

### 6.2.3 Diffuse Gamma-ray Emission

We first consider the gamma-ray emission produced by dark matter annihilating in the smooth host halo and the subhalos into $e^+e^-$ pairs scattering off the ISRF. Using the formalism developed in Sect. 6.2.1, the fluxes from the smooth host halo at 1 GeV, 10 GeV and 100 GeV are shown in Fig. 6.9. We use galactic coordinates, where an observer is located at 8.5 kpc from the Galactic center. We adopt the NFW density profile with the parameters given in Sect. 2.4, and find, as expected, that most of the signal comes from the central Galactic region where the dark matter is highly concentrated. The values of the mean gamma-ray intensity from both the host halo and the substructure are also reported in Tab. 6.1 for the above three photon energies. We find that in both cases the mean gamma-ray intensity decreases faster than $\sim E_\gamma^{-1/2}$ in Eq. (5.17). This is because there will be a high energy cut-off in $E_\gamma$ once the energy of the parent pairs $E \simeq m_e[E_\gamma/(4k_BT)]^{1/2}$ scattering off the low energy background photons exceeds the maximum energy $M_\chi$ produced by dark matter annihilation such that ICS can not produce any gamma-ray signals in delta-function approximation. As a consequence, all background photon energies at CMB energies and above contribute to the 1 GeV ICS photon flux, whereas only

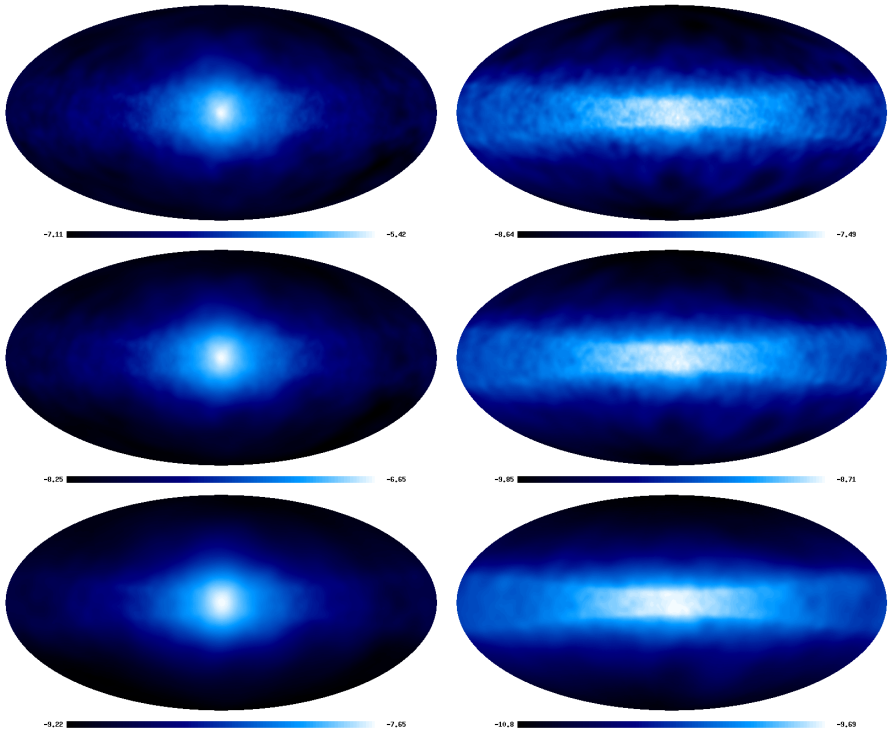

**Figure 6.11:** Sky maps of gamma-ray emission at 1 GeV, 10 GeV and 100 GeV (from top to bottom) due to ICS from one realization of subhalos for the unbiased (left panel) and anti-biased radial (right panel) distribution. The minimum subhalo mass is $10^{-6} M_\odot$. The color scaling is logarithmic, and the unit is $1/\mathrm{s}/\mathrm{cm}^2/\mathrm{sr}$.

the IR and SL contribute to the 10 GeV photon flux and only the SL contributes to the 100 GeV photon flux, as also summarized in Tab. 6.2. Furthermore, using the relation between $E$ and $E_\gamma$ and the expression for $P_{\rm IC}(E)$, for an electron spectrum $\sigma_e \propto E^{-s}$ Eq. (5.17) gives the scaling $I_{\rm IC}(E_\gamma) \propto u_b E_\gamma^{(1-s)/2} T^{(s-3)/2}$. Using the different normalizations for the CMB, IR and SL densities then shows that the gamma-ray intensity originating from $e^+e^-$ pairs scattering off CMB photons is about 5 times larger than the one from scattering off the IR photons and about 10 times lager than the contribution from scattering off SL photons, provided there is no restriction from the kinematics. However, the $e^+e^-$ pairs produced by annihilating dark matter have an absolute cutoff at the parent particle energy. As a result, the more detailed numerical results show that most of the gamma-ray intensity at 1 GeV is produced by pairs with $E \simeq 526$ GeV scattering off the CMB, whereas pairs with $E \simeq 431$ GeV scattering off IR photons dominate the 10 GeV gamma-ray flux and pairs with $E \simeq 141$ GeV scattering off SL dominate ICS photons at 100 GeV.

In Fig. 6.10, we present the sky map of gamma-ray emission predicted by an unbiased radial distribution of subhalos: in order to avoid saturation from the dominant population of small halos, in the figure we only include halos with mass above $10^6 M_\odot$. The most remarkable feature in Fig. 6.10 is that the diffuse emission regions

| Halo model | $E_\gamma = 1$ GeV | $E_\gamma = 10$ GeV | $E_\gamma$ =100 GeV |
|---|---|---|---|
| $M_{min} = 10^{-6} M_\odot$ + unbiased | $3.27 \times 10^{-7}$ | $2.03 \times 10^{-8}$ | $2.21 \times 10^{-9}$ |
| $M_{min} = 10^{-6} M_\odot$+ anti-biased | $8.17 \times 10^{-9}$ | $5.07 \times 10^{-10}$ | $5.52 \times 10^{-11}$ |
| Host halo | $3.83 \times 10^{-10}$ | $2.44 \times 10^{-11}$ | $2.73 \times 10^{-12}$ |

**Table 6.1:** The mean gamma-ray intensities $\langle I \rangle$ at 1 GeV, 10 GeV and 100 GeV, averaged over the sky, from subhalos with minimum mass $M_{\rm min} = 10^{-6} M_\odot$ for the unbiased and anti-biased radial distribution and from the smooth host halo. The unit is cm$^2$/s/sr.

| $E_\gamma$(GeV) | SL ($T_p$ =3800 K) | IR ($T_p$ =40.6 K) | CMB ($T_p$ =2.73 K) |
|---|---|---|---|
| 1 | 14 GeV (2.28 kpc) | 136 GeV (1.1 kpc) | 526 GeV (0.48 kpc) |
| 10 | 44 GeV (1.76 kpc) | 431 GeV (0.65 kpc) | 1665 GeV |
| 100 | 141 GeV (1.26 kpc) | 1365 GeV | 5267 GeV |

**Table 6.2:** The dependence of the characteristic electron energy $E$ on the energy $E_\gamma$ of gamma-ray emission through inverse Compton scattering off the various blackbody components of the ISRF with temperatures $T_p$. For the cases $E < 1$ TeV the corresponding diffusion length $\lambda_D(E)$ is also shown in braces.

can extend to a few kpc in length scale, corresponding to a few tens of degrees on the sky. Furthermore, the size of the brightest regions representing the largest intensity tends to increase with increasing $E_\gamma$, which could give rise to an increase of the angular power spectrum on corresponding angular scales. The size of the emitting region is basically determined by the diffusion length $\lambda_D$ which is the distance that the $e^+e^-$ diffuses during their energy loss time. This length scale can be estimated from Eq. (4.17), giving $\lambda_D(E) \propto E^{-0.15}$ for the MED propagation model. This energy dependence of $\lambda_D$ is shown in Tab. 6.2. The typical diffusion length is 0.48 kpc, 0.65 kpc and 1.26 kpc for electron energies leading to emission at $E_\gamma = 1$ GeV, 10 GeV and 100 GeV, respectively, corresponding to an angular scale $\theta \simeq \lambda_D/d$ with $d \sim$ few kpc the typical distance to the dark matter annihilation source. These angular scales are roughly what one sees in Fig. 6.10 and the above estimate also applies to the smooth host halo case (see Fig. 6.9) and to the anti-biased radial distribution of subhalos.

How does the mean intensity depend on $M_{\rm min}$? Empirically, we find that the mean intensity roughly doubles with each decade of decreasing mass of subhalos, similar to what has been found by Ref. [82]. In light of the subhalo mass function $N(> M)$ in Eq. (2.29) and the concentration parameter $c(M)$ in Eq. (2.30), the annihilation rates per decade of subhalo mass can be approximated by $c(M)^3 M^2 dN/dM \Delta \log(M) \simeq c(M)^3 M N(> M) \simeq M^{-0.3}$, which is fairly consistent with our detailed numerical calculation.

In order to determine the influence of the radial distribution of subhalos on the

intensity, in Fig. 6.11 the gamma-ray full-sky maps at 1 GeV, 10 GeV and 100 GeV for the un-biased distribution are compared with the anti-biased distribution. For the anti-biased radial distribution the mean intensities are roughly 50 times smaller than for the unbiased case since the mean distance of subhalos to us is much larger than in the unbiased case. One notices the important feature in Fig. 6.11 that the emission from the spatially anti-biased distribution is much less centrally concentrated, and apparently accumulates around the Galactic plane compared with the unbiased case. This can be understood from the fact that only electrons and positrons confined within the diffusion zone of scale height $L = 4$ kpc and radius $R = 20$ kpc for the MED model can efficiently produce gamma-rays by ICS and the subhalos within the diffusion zone are distributed much more isotropically for the anti-biased case compared to the more central distribution of the unbiased case. Furthermore, ICS outside the diffusion zone contributes less than 10% to the mean intensity [19, 79, 258].

### 6.2.4 Galactic Anisotropy Signatures

The dimensionless angular power spectra $C_l$ of gamma-ray emission due to the ICS at photon energies 1 GeV, 10 GeV and 100 GeV from the main components of Galactic dark matter are presented in Fig. 6.12. Shown are the power spectrum for subhalos with $M_{\rm min} = 10^{-6} M_\odot$ for the unbiased radial distribution and for the smooth host halo. To clearly illustrate the effects of diffusion, the angular power spectra for spatially unbiased subhalos with $M_{\rm min} = 10^2 M_\odot$ and for the host halo are also shown in absence of diffusion. We recall that in order to obtain for a given component the contribution to the angular power spectrum $C_l^I$ in units of intensity squared, according to Eq. (6.50) one has to multiply the dimensionless power spectra $C_l$ shown in Fig. 6.12 by the squared total intensity $\langle I \rangle^2$ of the corresponding component from Tab. 6.1.

Fig. 6.12 demonstrates the remarkable feature that the power spectrum of the ICS component of galactic dark matter annihilation is exponentially suppressed for $l \gtrsim 10$ compared with what one would obtain without diffusion. Furthermore, the lower energy gamma-rays have more angular power at $l \gtrsim 10$ corresponding to small angular scale. This can be understood from the energy-dependence of the diffusion length: Intensity fluctuations should be damped on length scales smaller than the diffusion length $\lambda_D$, corresponding to a multipole $l \gtrsim \pi d/\lambda_D$, where $d$ is the typical distance to the dark matter annihilation source. Based on the discussion in Sect. 6.2.3, we can estimate the diffusion length of the electrons and positrons emitting a given gamma-ray energy. When doing so, one should keep in mind that the $e^+e^-$ pairs interact with three different photon backgrounds and that, as it turns out, unlike the case of a single background, the lower the gamma-ray energy the higher the energy of the emitting electrons. Since we found that the diffusion length decreases with the electron energy, $\lambda_D(E) \propto E^{-0.15}$, we expect suppression of anisotropies to occur at smaller scales, or larger values of the multipole $l$, for lower photon energy. For other propagation models such as the MIN and MAX models

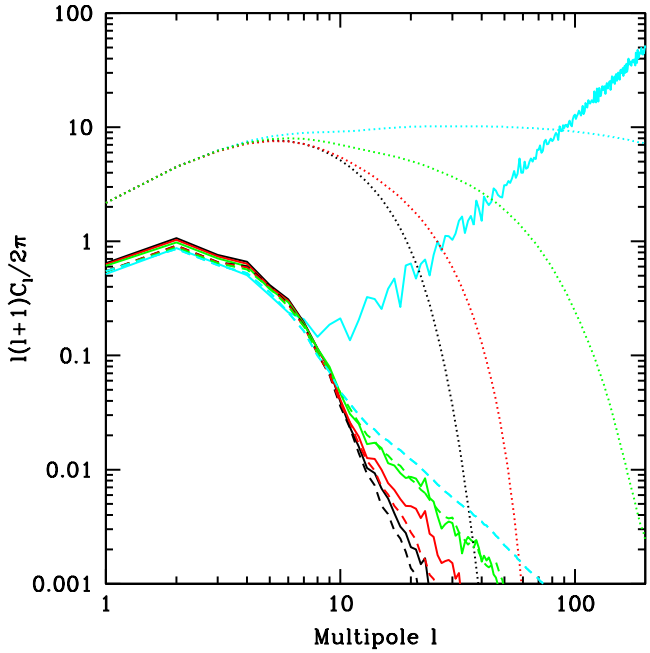


**Figure 6.12:** Dimensionless angular power spectrum $C_l$ of the gamma-ray sky from dark matter annihilation at $E_\gamma = 1$ GeV (green), 10 GeV (red) and 100 GeV (black), respectively. Solid curves correspond to the case of substructures with minimum subhalo mass $M_{\rm min} = 10^{-6} M_\odot$ for the unbiased radial distribution. Dotted and dashed curves are for the smooth host halo with NFW profile, where the emissivity $\propto \rho^2$ and $\propto \rho$, respectively. For comparison, the cyan curves show the power spectrum in absence of diffusion (see text for details). We find a strong suppression due to diffusion for $l \gtrsim 10$. Each power spectrum is calculated exclusively from the contribution of the indicated source component.

which have a slightly different energy dependence of the spatial diffusion coefficient, the diffusion length would be slightly larger or smaller, respectively. This would shift the suppression scale in the angular power spectrum by less than a factor of two in the multipole $l$.

In fact, for the smooth host halo the typical distance is $d \simeq 8.5$ kpc, and the suppression due to diffusion should occur at $l \simeq 55, 47$ and 28 for gamma-ray energies of 1 GeV, 10 GeV and 100 GeV, respectively. This analysis can be applied to the case of subhalos. For an unbiased spatial distribution of subhalos, the typical distance to a subhalo is $d \simeq 7\,$kpc which corresponds to diffusive suppression at relatively smaller $l$ compared to the host halo case. These simple estimates are consistent with our detailed calculations shown in Fig. 6.12.

We also find that the amplitude of the dimensionless angular power spectrum $C_l$ from the smooth host halo is larger than that from the subhalos since the emissivity profile from annihilation in the smooth halo is proportional to the density squared

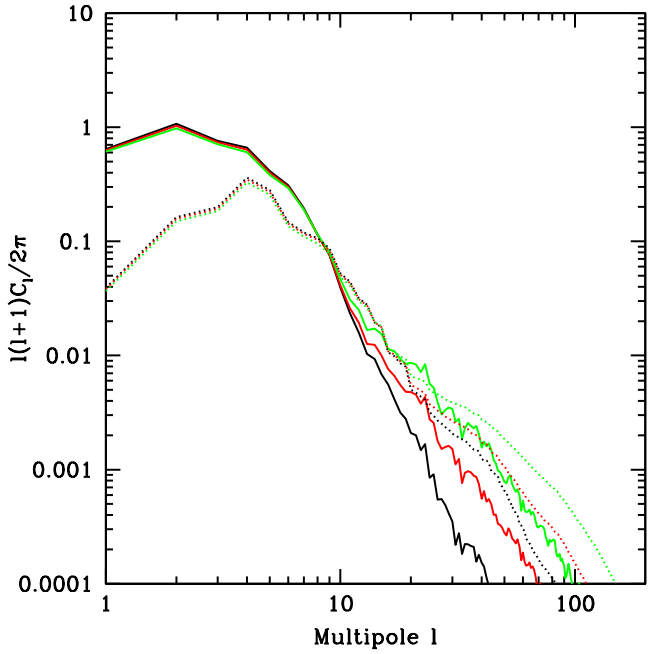


**Figure 6.13:** Comparison of the dimensionless angular power spectrum $C_l$ of gamma-ray emission from dark matter substructures for the unbiased radial distribution (solid) and the anti-biased distribution (dotted) at $E_\gamma = 1$ GeV (green), 10 GeV (red) and 100 GeV (black) with $M_{\rm min} = 10^{-6} M_\odot$.

and thus more peaked than annihilation in the subhalos which essentially follow the linear density profile of an NFW profile, as we see in Fig. 6.12. We note that although the smooth host halo has a large amplitude of the dimensionless angular power spectrum $C_l$, its contribution to the total intensity is as small as $\sim 0.1\%$ for the unbiased subhalo distribution and $\sim 5\%$ for the anti-biased distribution, as seen in Tab. 6.1. We can therefore safely neglect the contribution from the host halo both to the mean intensity and to the dimensional angular power spectrum $C_l^I$.

Finally, we show in Fig. 6.12 the dimensionless angular power spectrum $C_l$ for a smooth halo with emissivity tracing the density of the NFW profile instead of the squared density that would be relevant for the contribution of the host halo in annihilation scenarios. This shows that a smooth NFW profile describes the emission profile by a large number of subhalos following an unbiased radial distribution very well, at a level of $\sim 0.1\%$. This is not surprising since the number of subhalos within the diffusion zone with masses below $10^4 M_\odot$ is sufficiently large, $> 10^5$, for each mass decade to strongly suppress any deviation from a smooth distribution. This conclusion is also true for the anti-biased case. Despite the fact that the contribution of large subhalos in the mass range of $10^4 - 10^{10} M_\odot$ fluctuates strongly, their contribution to the total emission are three orders of magnitude smaller which leads to fluctuations at 0.1% level in angular power spectrum as seen in Fig. 6.12.

How does the radial subhalo distribution affect the angular power spectrum? In Fig. 6.13 we compare results for the unbiased case and the anti-biased case. At small $l$ the angular power spectrum $C_l$ for the anti-biased distribution is suppressed relative to the unbiased case which is due to the more isotropic subhalo distribution at large angular scales seen in Fig. 6.11. For $l \gtrsim 10$, the angular power spectrum induced by an anti-biased distribution has more power than the unbiased case because the typical distance to subhalos is larger for the anti-biased distribution, shifting power to larger $l$.

### 6.2.5 Comparison with Fermi-LAT observations

We now turn to a comparison of the predicted angular power spectra with to the gamma-ray power spectra measured by Fermi-LAT at three energy bins, namely 1-2 GeV, 10-20 GeV and 100-300 GeV. In this study, we do not aim to perform a detailed data analysis including foreground cleaning which would in any case be considerably model dependent. We instead analyze the public data from Ref. [13] which is based on the removal of 3-month 10-sigma bright sources. The raw data used here can be regarded as an overestimation of the gamma-ray background since the further foreground cleaning and the removal of point sources is expected to significantly reduce the mean intensity.

In Fig. 6.14, in order to illustrate the absolute amplitude of the anisotropies, we show the square root of the angular power spectrum in units ph/cm$^2$/s/sr of intensity. As seen in Tab. 6.1, the dimensional angular power spectrum from ICS for the anti-biased subhalo distribution is two order of magnitude smaller than for the unbiased case because of the large normalization from the mean intensity for the latter case. The diffusion of electrons and positrons strongly suppresses the angular power spectrum for $l \gtrsim 10$, in contrast to the observed angular power spectrum which tends to increase at large $l$ for $100\,\mathrm{GeV} \lesssim E_\gamma \lesssim 300\,\mathrm{GeV}$ and is roughly flat at lower energies. The optimal window for searching for the ICS signal of dark matter annihilation should thus be at $5 \lesssim l \lesssim 100$. In this window one may also be able to distinguish from the gamma-ray power spectrum produced by direct annihilation which has no large-$l$ suppression and is more similar to the observed total power spectrum.

We note that for these anisotropy signals to the detectable with a signal-to-background lager than one requires sufficiently large annihilation rates, larger than the thermal relic rate by factors $\sim 5$ and $\sim 3$ for the energy bins at 1-2 GeV and 10-20 GeV respectively for an unbiased subhalo distribution. For 100-300 GeV, the particle physics parameters used here lead to a power spectrum comparable amplitude to the background. However, large Poisson noise due to the small photon count rates can introduce $\mathcal{O}(1)$ uncertainties. For an anti-base subhalo distribution, detectability in the energy bins at 1-2 GeV, 10-20 GeV and 100-300 GeV requires a boost factor beyond the canonical thermal rate of $\sim 500$,$\sim 300$ and $\sim 100$, respectively.

Since astrophysical sources producing gamma-rays should highly contaminate the sky regions around the galactic center and the galactic plane ($|b| < 30^\circ$ for $|l| < 40^\circ$),

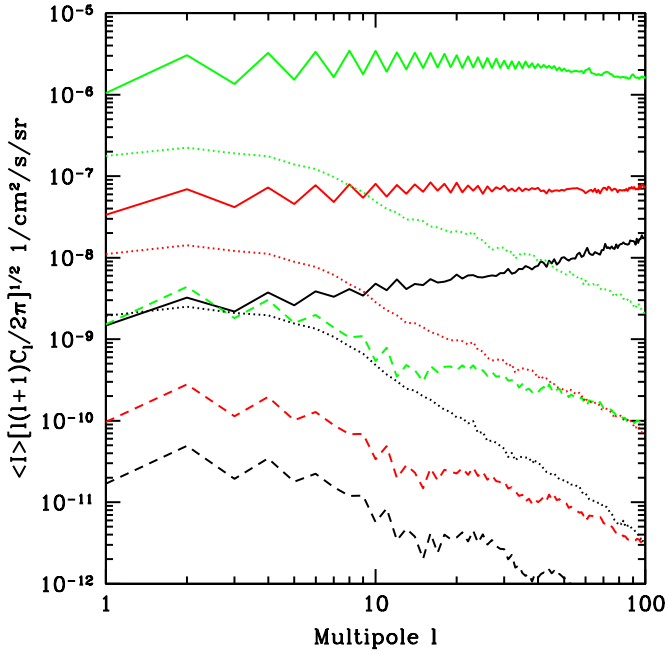


**Figure 6.14:** The dimensional angular power spectrum $C_l^I$ of full-sky gamma-ray anisotropies due to ICS from the entire Galactic dark matter including the host halo and subhalos with minimum masss $M_{\rm min} = 10^{-6} M_\odot$ for unbiased (dotted) and anti-biased case (dashed) distributions compared to the Fermi-LAT gamma-ray observations (solid), at three gamma-ray energies: 1-2 GeV (green), 10-20 GeV (red) and 100-300 GeV (black).

the signals in those regions are usually masked. However, this procedure also removes the dark matter contributions in those regions. We find that the constraining power when using those masked maps is similar to those without mask. We thus do not use masks in the current study.

# Chapter 7

# Summary and Outlook

During the last three years, my main research has focused on the understanding of the nature of dark matter. In order to shed some light on this exciting topic, I proposed two different approaches to extract dark matter diffuse and anisotropy signatures from astrophysical background. Here I briefly describe my main contributions to this field.

### Spectral Signatures of Decaying Dark Matter

In this study, we computed the prediction for three important signatures from decaying dark matter, namely the synchrotron emissions, the positron fluxes and the gamma ray fluxes including the inverse Compton photons resulting from energetic electrons and positrons through scattering with low energy target photons in addition to the bremsstrahlung emissions.

In the view of the recent experimental observations such as the radio full-sky surveys, the PAMELA data and the full-sky gamma-ray observations by Fermi-LAT, we introduced useful response functions that can be applied to constrain any interesting decay models. Robust constraints can be obtained in terms of convolving the response function with the specific decay spectrum into electrons and positrons. Our results show that the resulting constraints depend mostly on the set of propagation parameters rather than the halo profiles. We have finally applied our method to provide model independent constraints on concrete decay modes. In the most case, we found that the strongest constraints on injection spectrum at low energies ($\lesssim$ 1000 GeV) come from the positron data due to its lowest background and at high energies ($\gtrsim$ 1000 GeV) from gamma-ray data. The radio data always provide a relatively weaker constraining power.

### Anisotropy Signatures of Annihilating Dark Matter

In addition, we perform a detailed study of the anisotropy related to the extragalactic and the Galactic dark matter signals. At the radio band, we calculated the angular power spectrum of the cosmological background of synchrotron emission from the

electrons and positrons produced during the annihilations of the extragalactic cold dark matter. The resulting radio background around $\simeq 2\,\mathrm{GHz}$ and its angular power spectrum for multipoles $200 \lesssim l \lesssim 3000$ has comparable or better sensitivity to dark matter annihilation cross sections than other signatures. Under reasonable assumptions on dark matter clustering and magnetic fields in the halo environment, the sensitivity of our signal is considerably better than the conservative limits based on the annihilation of dark matter into neutrinos [149], and comparable to the limits on its annihilation into gamma-rays from diffuse cosmological emission [150].

Furthermore, we investigated the angular power spectrum of the inverse Compton gamma-ray emission from electrons and positrons produced by the Galactic dark matter annihilation. We considered two extreme cases for the radial distribution of subhalos and simulated the full-sky gamma-ray maps at three energies through realizations of a large number of subhalos with masses down to $10^{-6} M_{\odot}$. The contributions to the angular power spectrum and the total flux from the smooth host halo were also made. We then compared the predicted anisotropy signals with the Fermi-LAT observations and discussed the detectability of these signals. We found that, unlike the total gamma-ray angular power spectrum observed by Fermi-LAT, the angular power spectrum from inverse Compton scattering is exponentially suppressed below an angular scale determined by the diffusion length of electrons and positrons. For TeV scale dark matter with a canonical thermal freeze-out cross section of $3 \times 10^{-26} \mathrm{cm}^3/\mathrm{s}$, this feature may be detectable by Fermi-LAT in the energy range 100-300 GeV after more sophisticated foreground subtraction.

### Outlook and Prospects

We already noticed that the largest uncertainties in the predicted signals come from poorly known propagation parameters, such as the reacceleration of electrons and the height of the diffusion zone. The corresponding uncertainty can reach one order of magnitude. Due to these uncertainties it is hard to obtain any definitive constraint on dark matter. The forthcoming AMS-02 experiment [198] will however provide very accurate data on the unstable/stable ratios (as well as for B/C and other stable secondary/primary ratios), which might allow a more precise determination of the diffusion height scale $L$. Also, a more sophisticated foreground subtraction will significantly improve the detectability of dark matter. More works in these issues will therefore be required to gain insight.

On other hand, for anisotropy gamma-ray signatures, we have assumed homogeneous and isotropic magnetic fields and interstellar radiation field. However, in a more realistic case where the radiation and magnetic fields depend on the position in the Galaxy [200], the angular power spectrum should be modified at least at large angular scales. In particular, the small scale fluctuations of the magnetic field could affect the distribution of electrons and positrons [259], influencing the angular power spectrum at all scales. Moreover, a space-dependence of the diffusion length could also lead to a directional dependence of the angular power spectrum. Obviously detecting the differential effect of the anisotropy signal across the Galactic latitude

would be even more difficult than detecting the signal integrated over the whole sky. However, it could introduce subtle effects when part of the sky is masked out, e.g. to avoid the contribution from the Galactic plane. These complications should be investigated more thoroughly in the future by performing a real 3D simulation through numerically solving the transport equation for electrons and positrons. While the formalism developed in Sect. 6.2 can be extended to the anisotropies of the radio sky, the small scale structure of the magnetic field is more important for synchrotron emission and should be treated in more detail. In addition, our work could also be extended to inverse Compton gamma-ray emission from extragalactic dark matter halos.

Finally, annihilation or decay would also affect the expansion history of the Universe due to a change of the equation of state [5, 260], and potentially leave an imprint on the Universe. Considering the heating and ionization effects on baryonic gas during the dark age [3, 4, 261], future 21 cm observation [100, 262, 263] could lead to discovery of visible evidence for dark matter decays or annihilations. We believe that radio observations in particular the future instruments such as the SKA [101] can provide valuable information on the nature of dark matter.

# Appendix A

# Fourier Transforms

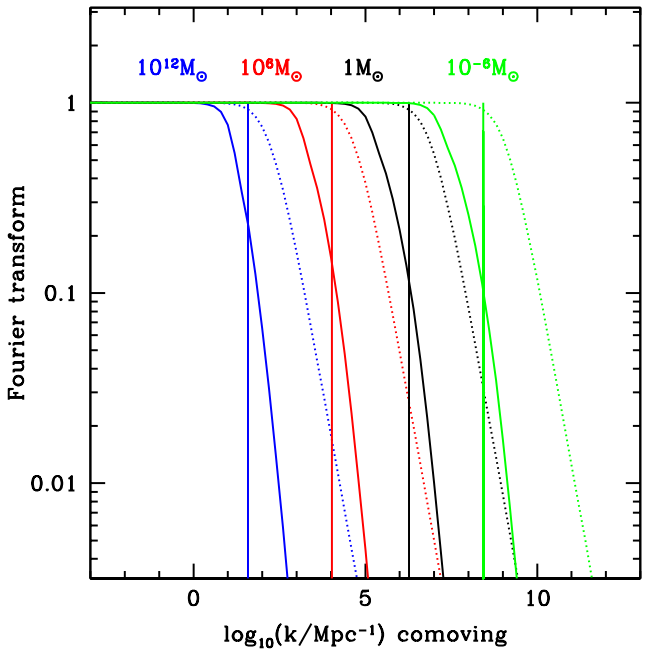


**Figure A.1:** The normalized Fourier transforms $y_1(k, M)$ (solid lines) and $y_2(k, M)$ (dotted lines) of $\rho_h$ and $\rho_{h^2}$, respectively, as functions of co-moving wavenumber $k$. The vertical lines denote the scale $k = 1/r_s(M)$.

The Fourier transform of the spherically symmetric NFW profile of mass M can be written as

$$\mathcal{F}_{\rho_h}(k, M) = \int_0^{r_v} \rho_h(M, r) \frac{\sin(kr)}{kr} 4\pi r^2 dr \,, \tag{A.1}$$

and analogously for $\mathcal{F}_{\rho_h^2}(k, M)$. For the purpose of plotting these Fourier transforms, see Fig. A.1, it is convenient to renormalize them to unity for $k \to 0$ by introducing the new functions $y_1(k, M) = \mathcal{F}_{\rho_h}(k, M)/M$ and $y_2(k, M) = \mathcal{F}_{\rho_h^2}(k, M)/\int dV_h \rho_h^2(\mathbf{r})$. We then have $y_i(0, M) = 1$, and $y_i(k > 0, M) < 1$ for $i = 1, 2$. For the NFW density

profile, $\int dV_h \rho_h^2(\mathbf{r}) = f_c M \rho_m \Delta_c(z)$, where $f_c = (c^3/9)\left[1-(1+c)^{-3}\right] / \left[\log(1+c) - c/(1+c)\right]^2$, and $\Delta(z) \sim 200$. The mass of the halo within radius $r$ increases $\propto r^2$ for $r \lesssim r_s$, and then increase logarithmically for $r_s \lesssim r \lesssim r_v$ where $\rho_h(r) \propto r^{-3}$. Therefore, the dominant contribution to the halo mass comes from $r \lesssim r_s$. Similarly, the annihilation signal is produced mainly within $r \lesssim r_s$, increasing there $\propto r$, but increases only $\propto r_s^{-3} - r^{-3}$ for $r_s \lesssim r \lesssim r_v$.

Fig. A.1 shows that for $kr_s \ll 1$ we have $y_{1,2} \simeq 1$, whereas for $kr_s \gg 1$ one has $y_2(k, M) \propto k^{-1}$, and $y_1(k, M) \propto k^{-2}$.

# Appendix B

# Radio Foregrounds

The radio intensity $I_\nu$ at a given frequency $\nu$ can be expressed in terms of antenna temperature $T_A(\nu)$ via $I_\nu = 2\nu^2 k_\mathrm{B} T_A(\nu)/c_0^2$, where $c_0$ is the speed of light. Alternatively, $I_\nu$ can be written in terms of the thermodynamic temperature as the temperature of a blackbody with the given intensity at frequency $\nu$, thus $I_\nu = 2\nu^3/(e^x - 1)$, where $x \equiv h\nu/k_\mathrm{B}T$ with $h$ the Planck constant. Thus, for power law spectra $I_\nu \propto \nu^\alpha$, $T_A \propto \nu^{\alpha-2}$. In general, the CMB is expressed in terms of thermodynamic temperature $T$, while Galactic and extragalactic foregrounds are expressed in term of antenna temperature. Thermodynamic and antenna temperature are then related by $T = T_A(e^x - 1)/x$, and their fluctuations by $\Delta T = \Delta T_A (e^x - 1)^2/(x^2 e^x)$. For the CMB, $x = h\nu/(k_\mathrm{B} T_\mathrm{CMB}) \simeq \nu/(56.8\,\mathrm{GHz})$ with the CMB temperature $T_\mathrm{CMB} = 2.725\,\mathrm{K}$ [245]. Since we consider frequencies $\nu \lesssim 10\,\mathrm{GHz}$ in Sect. 6.1, $x \ll 1$ and thus $T \simeq T_A$ and $\Delta T \simeq \Delta T_A$.

From the definition of $T_A$ we get

$$I_\nu = 3.06 \times 10^{-25} \left(\frac{\nu}{\mathrm{GHz}}\right)^2 \left(\frac{T_A}{\mu\mathrm{K}}\right) \mathrm{erg\,cm^{-2}\,s^{-1}\,Hz^{-1}\,sr^{-1}}\,. \tag{B.1}$$

Since for $I_\nu \propto \nu^\alpha$ the power spectrum $C_l^{I_\nu}$ of $I_\nu$ at frequency $\nu$ scales as $\nu^{2\alpha}$, we can express it in terms of the power spectrum $C^{T_A}(\nu')$ of the antenna temperature $T_A$ at frequency $\nu'$ via

$$\sqrt{C_l^{I_\nu}(\nu)} = 3.06 \times 10^{-25} \left(\frac{\nu}{\nu'}\right)^{\alpha-2} \sqrt{\frac{C_l^{T_A}(\nu')}{\mu\mathrm{K}^2}} \left(\frac{\nu}{\mathrm{GHz}}\right)^2 \mathrm{erg\,cm^{-2}\,s^{-1}\,Hz^{-1}\,sr^{-1}}\,. \tag{B.2}$$

Here, $\alpha = -0.9$ for synchrotron emission and $-0.15$ for free-free emissions, respectively [248]. For the normalization and the dependence on $l$, we adopted the best-fit model from observations at 2.3 GHz [250]. These parametrizations have been used in Fig. 6.7.

# Bibliography


[1] G. Bertone, D. Hooper and J. Silk, "Particle dark matter: Evidence, candidates and constraints," Phys. Rept. **405**, 279 (2005) [arXiv:hep-ph/0404175]. 1, 8

[2] G. Jungman, M. Kamionkowski and K. Griest, "Supersymmetric dark matter," Phys. Rept. **267**, 195 (1996) [arXiv:hep-ph/9506380]. v, 1, 14, 15, 16

[3] X. L. Chen and M. Kamionkowski, "Particle decays during the cosmic dark ages," Phys. Rev. D **70**, 043502 (2004) [arXiv:astro-ph/0310473]. 1, 16, 105

[4] L. Zhang, X. Chen, M. Kamionkowski, Z. g. Si and Z. Zheng, "Contraints on radiative dark-matter decay from the cosmic microwave background," Phys. Rev. D **76**, 061301 (2007) [arXiv:0704.2444 [astro-ph]]. 1, 16, 105

[5] Y. Gong and X. Chen, "Cosmological Constraints on Invisible Decay of Dark Matter," Phys. Rev. D **77**, 103511 (2008) [arXiv:0802.2296 [astro-ph]]. 1, 16, 105

[6] O. Adriani *et al.* [PAMELA Collaboration], "Observation of an anomalous positron abundance in the cosmic radiation," arXiv:0810.4995 [astro-ph]. vi, vii, 2, 25, 27, 39, 51, 52, 53, 54

[7] O. Adriani *et al.*, "A new measurement of the antiproton-to-proton flux ratio up to 100 GeV in the cosmic radiation," arXiv:0810.4994 [astro-ph]. vi, vii, 2, 27, 28, 39, 53, 56

[8] J. Chang *et al.*, "An Excess Of Cosmic Ray Electrons At Energies Of 300-800 Gev," Nature **456**, 362 (2008). 2, 28

[9] A. A. Abdo *et al.* [The Fermi LAT Collaboration], "Measurement of the Cosmic Ray e+ plus e- spectrum from 20 GeV to 1 TeV with the Fermi Large Area Telescope," arXiv:0905.0025 [astro-ph.HE]. vii, 2, 28, 40, 51, 53

[10] F. Aharonian *et al.* [H.E.S.S. Collaboration], "The energy spectrum of cosmic-ray electrons at TeV energies," Phys. Rev. Lett. **101**, 261104 (2008) [arXiv:0811.3894 [astro-ph]]. 2, 28

[11] F. Aharonian *et al.* [H.E.S.S. Collaboration], "Probing the ATIC peak in the cosmic-ray electron spectrum with H.E.S.S," Astron. Astrophys. **508**, 561 (2009) [arXiv:0905.0105 [astro-ph.HE]]. 2, 28

[12] D. Hooper, D. P. Finkbeiner and G. Dobler, "Evidence Of Dark Matter Annihilations In The WMAP Haze," Phys. Rev. D **76**, 083012 (2007) [arXiv:0705.3655 [astro-ph]]. 2, 21

[13] G. Dobler, D. P. Finkbeiner, I. Cholis, T. R. Slatyer and N. Weiner, "The Fermi Haze: A Gamma-Ray Counterpart to the Microwave Haze," arXiv:0910.4583 [astro-ph.HE]. 2, 20, 57, 59, 101

[14] S. Profumo, "Dissecting Pamela (and ATIC) with Occam's Razor: existing, well-known Pulsars naturally account for the 'anomalous' Cosmic-Ray Electron and Positron Data," arXiv:0812.4457 [astro-ph]. 2, 28

[15] M. Kaplinghat, D. J. Phalen and K. M. Zurek, "Pulsars as the Source of the WMAP Haze," arXiv:0905.0487 [astro-ph.HE]. 2

[16] D. Malyshev, I. Cholis and J. Gelfand, "Pulsars versus Dark Matter Interpretation of ATIC/PAMELA," arXiv:0903.1310 [astro-ph.HE]. 2, 28

[17] D. Hooper, P. Blasi and P. D. Serpico, "Pulsars as the Sources of High Energy Cosmic Ray Positrons," JCAP **0901**, 025 (2009) [arXiv:0810.1527 [astro-ph]]. 2, 28

[18] L. Zhang and G. Sigl, "Dark Matter Signatures in the Anisotropic Radio Sky," JCAP **0809**, 027 (2008) [arXiv:0807.3429 [astro-ph]]. 2

[19] L. Zhang, G. Sigl and J. Redondo, "Galactic Signatures of Decaying Dark Matter," JCAP **0909**, 012 (2009) [arXiv:0905.4952 [astro-ph.GA]]. vii, 2, 28, 39, 49, 54, 98

[20] L. Zhang, C. Weniger, L. Maccione, J. Redondo and G. Sigl, "Constraining Decaying Dark Matter with Fermi LAT Gamma-rays," JCAP **1006**, 027 (2010) [arXiv:0912.4504 [astro-ph.HE]]. viii, 2, 28, 39, 61

[21] L. Zhang, F. Miniati and G. Sigl, "Inverse Compton gamma-rays from Galactic dark matter annihilation: Anisotropy signatures," arXiv:1008.1801 [astro-ph.HE]. 2, 63

[22] L. Bergstrom, Rept. Prog. Phys. **63**, 793 (2000) [arXiv:hep-ph/0002126]. 3, 16

[23] E. W. Kolb and M. S. Turner, "The Early Universe", (Front. Phys., 1990). 3

[24] M. Trodden and S. M. Carroll, "TASI lectures: Introduction to cosmology," arXiv:astro-ph/0401547. 3

[25] S. M. Carroll, "Spacetime and geometry: An introduction to general relativity", (San Francisco, USA: Addison-Wesley, 2004) p. 513. 3

[26] A. G. Riess *et al.* [Supernova Search Team Collaboration], "Observational Evidence from Supernovae for an Accelerating Universe and a Cosmological Constant," Astron. J. **116**, 1009 (1998) [arXiv:astro-ph/9805201]. 4

[27] E. Komatsu *et al.* [WMAP Collaboration], "Five-Year Wilkinson Microwave Anisotropy Probe (WMAP) Observations:Cosmological Interpretation," arXiv:0803.0547 [astro-ph]. 4, 11, 18

[28] F. Zwicky, "Die Rotverschiebung von extragalaktischen Nebeln", Helvetica Physica Acta, 6:110-127, 1933. 4

[29] V. C. Rubin and W. K. Ford, Jr., "Rotation of the Andromeda Nebula from a Spectroscopic Survey of Emission Regions", Astrophys. J. **159**, 379 (1970). 4

[30] N. Bahcall and X. Fan, Astrophys. J. **504**,1 (1998). 4

[31] A. Kashlinsky, Phys. Rept. **307**, 67 (1998). 4

[32] R. G. Carlberg et al., Astrophys. J. **516**,552, (1999). 4

[33] J.A. Tyson, G.P. Kochanski and I.P. Dell'Antonio, Astrophys. J. Lett. **498**, 107 (1998). 5

[34] G. Bertone, G. Sigl and J. Silk, "Astrophysical limits on massive dark matter," Mon. Not. Roy. Astron. Soc. **326**, 799 (2001) [arXiv:astro-ph/0101134]. 5, 73, 74

[35] V.C.Rubin,D.Burstein,W.K.Ford,Jr.,and N.Thonnard, "Rotation velocities of 16 SA galaxies and a comparison of Sa, Sb, and SC rotation properties", Astrophys. J. **289**,81, (1985). v, 5

[36] D. Clowe, M. Bradac, A. H. Gonzalez, M. Markevitch, S. W. Randall, C. Jones and D. Zaritsky, "A direct empirical proof of the existence of dark matter," Astrophys. J. **648**, L109 (2006) [arXiv:astro-ph/0608407]. v, 5, 6

[37] M. Milgrom, "A Modification of the Newtonian dynamics as a possible alternative to the hidden mass hypothesis," Astrophys. J. **270**, 365 (1983). 5

[38] M. Milgrom, "The MOND paradigm," arXiv:0801.3133 [astro-ph]. 5

[39] R. A. Knop *et al.* [Supernova Cosmology Project Collaboration], "New Constraints on $\Omega_M$, $\Omega_\Lambda$, and w from an Independent Set of Eleven High-Redshift Supernovae Observed with HST," Astrophys. J. **598**, 102 (2003). [arXiv:astro-ph/0309368]. v, 7

[40] W. H. Press and P. Schechter, "Formation of galaxies and clusters of galaxies by selfsimilar gravitational Astrophys. J. **187**, 425 (1974). 7, 10, 77

[41] R. K. Sheth and G. Tormen, "Large scale bias and the peak background split," Mon. Not. Roy. Astron. Soc. **308**, 119 (1999) [arXiv:astro-ph/9901122]. 8, 10, 77

[42] John Dubinski and R. G. Carlberg, "The Structure of cold dark matter halos", Astrophys. J. **378**, 496 (1991). 8

[43] Volker Springel et al, "Simulating the joint evolution of quasars, galaxies and their large-scale distribution", Nature, **435**,629, (2005). 8

[44] J. Diemand and B. Moore, "The structure and evolution of cold dark matter halos," arXiv:0906.4340 [astro-ph.CO]. 8

[45] A. V. Kravtsov, A. A. Klypin, J. S. Bullock and J. R. Primack, "The Cores of Dark Matter Dominated Galaxies: theory vs. observations," Astrophys. J. **502**, 48 (1998) [arXiv:astro-ph/9708176]. 8, 56

[46] J. F. Navarro, C. S. Frenk and S. D. M. White, "The Structure of Cold Dark Matter Halos," Astrophys. J. **462**, 563 (1996) [arXiv:astro-ph/9508025]; 8, 13, 77

[47] L. Bergstrom, P. Ullio and J. H. Buckley, "Observability of gamma rays from dark matter neutralino annihilations in the Milky Way halo," Astropart. Phys. **9**, 137 (1998) [arXiv:astro-ph/9712318]. 8, 56

[48] Ben Moore, Thomas R. Quinn, Fabio Governato, Joachim Stadel, and George Lake, "Cold collapse and the core catastrophe", Mon. Not. Roy. Astron. Soc. **310**, 1147 (1999). 8

[49] B. Moore, T. Quinn, F. Governato, J. Stadel and G. Lake, "Cold collapse and the core catastrophe," Mon. Not. Roy. Astron. Soc. **310**, 1147 (1999) [arXiv:astro-ph/9903164]. 8

[50] Einasto J, "Influence of the atmospheric and instrumental dispersion on the brightness distribution in a galaxy", Trudy Inst. Astrofiz. Alma-Ata, 51:87, (1965). 8

[51] L. Gao *et al.*, "The redshift dependence of the structure of massive LCDM halos," arXiv:0711.0746 [astro-ph]. 9, 12, 13, 14

[52] J. P. Henry, "Measuring Cosmological Parameters from the Evolution of Cluster X-ray Temperatures," Astrophys. J. **534** (2000) 565 [arXiv:astro-ph/0002365]. 9

[53] N. Fornengo, L. Pieri and S. Scopel, "Neutralino annihilation into gamma-rays in the Milky Way and in external galaxies," Phys. Rev. D **70**, 103529 (2004) [arXiv:hep-ph/0407342]. 9, 13

[54] J. S. Bullock *et al.*, "Profiles of dark halos: evolution, scatter, and environment," Mon. Not. Roy. Astron. Soc. **321**, 559 (2001) [arXiv:astro-ph/9908159]. 9, 10, 14

[55] J. Diemand, M. Kuhlen and P. Madau, "Formation and evolution of galaxy dark matter halos and their substructure," Astrophys. J. **667**, 859 (2007) [arXiv:astro-ph/0703337]. 9, 14

[56] D. H. Zhao, Y. P. Jing, H. J. Mo and G. Boerner, "Accurate universal models for the mass accretion histories and concentrations of dark matter halos," Astrophys. J. **707**, 354 (2009) [arXiv:0811.0828 [astro-ph]]. 9

[57] A. Cooray and R. K. Sheth, "Halo models of large scale structure," Phys. Rept. **372**, 1 (2002) [arXiv:astro-ph/0206508]. 10, 77

[58] J. Diemand, B. Moore and J. Stadel, "Earth-mass dark-matter halos as the first structures in the early Nature **433** (2005) 389 [arXiv:astro-ph/0501589]. v, 10, 12, 77

[59] U. Seljak, "Analytic model for galaxy and dark matter clustering," Mon. Not. Roy. Astron. Soc. **318**, 203 (2000) [arXiv:astro-ph/0001493]. 10, 77

[60] J. M. Bardeen, J. R. Bond, N. Kaiser and A. S. Szalay, "The Statistics Of Peaks Of Gaussian Random Fields," Astrophys. J. **304** (1986) 15. 11

[61] J. Dunkley *et al.* [WMAP Collaboration], "Five-Year Wilkinson Microwave Anisotropy Probe (WMAP) Observations: Likelihoods and Parameters from the WMAP data," arXiv:0803.0586 [astro-ph]. 11

[62] S. M. Carroll, W. H. Press and E. L. Turner, "The Cosmological constant," Ann. Rev. Astron. Astrophys. **30** (1992) 499. 11

[63] A. M. Green, S. Hofmann and D. J. Schwarz, "The first WIMPy halos," JCAP **0508**, 003 (2005). 12, 77

[64] A. Loeb and M. Zaldarriaga, Phys. Rev. D **71**, 103520 (2005) [arXiv:astro-ph/0504112]. 12

[65] E. Bertschinger, Phys. Rev. D **74**, 063509 (2006) [arXiv:astro-ph/0607319]. 12

[66] S. Profumo, K. Sigurdson and M. Kamionkowski, Phys. Rev. Lett. **97**, 031301 (2006) [arXiv:astro-ph/0603373]. 12

[67] L. Gao, S. D. M. White, A. Jenkins, F. Stoehr and V. Springel, "The subhalo populations of LCDM dark halos," Mon. Not. Roy. Astron. Soc. **355** (2004) 819. 12, 13, 77

[68] J. Diemand, M. Kuhlen, P. Madau, M. Zemp, B. Moore, D. Potter and J. Stadel, "Clumps and streams in the local dark matter distribution," arXiv:0805.1244 [astro-ph]. v, 12, 13, 77

[69] B. Moore, S. Ghigna, F. Governato, G. Lake, T. Quinn, J. Stadel and P. Tozzi, "Dark Matter Substructure Within Galactic Halos," Astrophys. J. **524** (1999) L19. 12, 77

[70] A. A. Klypin, A. V. Kravtsov, O. Valenzuela and F. Prada, "Where are the missing galactic satellites?," Astrophys. J. **522**, 82 (1999) [arXiv:astro-ph/9901240]. 12

[71] A. R. Zentner and J. S. Bullock, "Halo Substructure And The Power Spectrum," Astrophys. J. **598**, 49 (2003) [arXiv:astro-ph/0304292]. 12, 77

[72] M. Kamionkowski and A. R. Liddle, "The dearth of halo dwarf galaxies: is there power on short scales?," Phys. Rev. Lett. **84**, 4525 (2000) [arXiv:astro-ph/9911103]. 12

[73] P. Colin, V. Avila-Reese and O. Valenzuela, "Substructure and halo density profiles in a Warm Dark Matter Cosmology," Astrophys. J. **542**, 622 (2000) [arXiv:astro-ph/0004115]. 12

[74] P. Bode, J. P. Ostriker and N. Turok, "Halo Formation in Warm Dark Matter Models," Astrophys. J. **556**, 93 (2001) [arXiv:astro-ph/0010389]. 12

[75] P. Colin, O. Valenzuela and V. Avila-Reese, "On the Structure of Dark Matter Halos at the Damping Scale of the Power Spectrum with and without Relict Velocities," Astrophys. J. **673**, 203 (2008) [arXiv:0709.4027 [astro-ph]]. 12

[76] A. V. Kravtsov, "Dark matter substructure and dwarf galactic satellites," arXiv:0906.3295 [astro-ph.CO]. 12

[77] E. A. Baltz and L. Wai, "Diffuse inverse Compton and synchrotron emission from dark matter annihilations in galactic satellites," Phys. Rev. D **70**, 023512 (2004) [arXiv:astro-ph/0403528]. 13, 37

[78] J. Diemand, M. Kuhlen and P. Madau, Astrophys. J. **657**, 262 (2007) [arXiv:astro-ph/0611370]. 13

[79] J. M. Cline, A. C. Vincent and W. Xue, "Leptons from Dark Matter Annihilation in Milky Way Subhalos," Phys. Rev. D **81**, 083512 (2010) [arXiv:1001.5399 [astro-ph.CO]]. 13, 98

[80] L. Pieri, G. Bertone and E. Branchini, Mon. Not. Roy. Astron. Soc. **384**, 1627 (2008) [arXiv:0706.2101 [astro-ph]]. 13

[81] M. Kamionkowski, S. M. Koushiappas and M. Kuhlen, Phys. Rev. D **81**, 043532 (2010) [arXiv:1001.3144 [astro-ph.GA]]. 13

[82] J. M. Siegal-Gaskins, "Revealing dark matter substructure with anisotropies in the diffuse gamma-ray background," arXiv:0807.1328 [astro-ph]. 14, 89, 97

[83] T. Bringmann, "Particle Models and the Small-Scale Structure of Dark Matter," New J. Phys. **11**, 105027 (2009) [arXiv:0903.0189 [astro-ph.CO]]. 16

[84] X. l. Chen, M. Kamionkowski and X. m. Zhang, "Kinetic decoupling of neutralino dark matter," Phys. Rev. D **64**, 021302 (2001). 16, 77

[85] W. Buchmuller, L. Covi, K. Hamaguchi, A. Ibarra and T. Yanagida, "Gravitino dark matter in R-parity breaking vacua," JHEP **0703**, 037 (2007) [arXiv:hep-ph/0702184]. 16, 64

[86] A. Boyarsky, O. Ruchayskiy and M. Shaposhnikov, "The role of sterile neutrinos in cosmology and astrophysics," Ann. Rev. Nucl. Part. Sci. **59** (2009) 191 [arXiv:0901.0011 [hep-ph]]. 16

[87] C. R. Chen, F. Takahashi and T. T. Yanagida, "Gamma rays and positrons from a decaying hidden gauge boson," Phys. Lett. B **671**, 71 (2009) [arXiv:0809.0792 [hep-ph]]. 16, 64

[88] A. Ibarra, A. Ringwald, D. Tran and C. Weniger, "Cosmic Rays from Leptophilic Dark Matter Decay via Kinetic Mixing," arXiv:0903.3625 [hep-ph]. 16, 65

[89] A. Arvanitaki, S. Dimopoulos, S. Dubovsky, P. W. Graham, R. Harnik and S. Rajendran, "Astrophysical Probes of Unification," arXiv:0812.2075 [hep-ph]. 16, 66

[90] National Radio Astronomy Observatory, http://www.cv.nrao.edu/course/astr534/images/atmos windows.gif v, 18

[91] M. G. Hauser and E. Dwek, "The Cosmic Infrared Background: Measurements and Implications," Ann. Rev. Astron. Astrophys. **39**, 249 (2001) [arXiv:astro-ph/0105539]. v, 19

[92] R. J. Wilman *et al.*, "A semi-empirical simulation of the extragalactic radio continuum sky for next generation radio telescopes," arXiv:0805.3413 [astro-ph]. 19

[93] G. F. Smoot, "Synchrotron Radiation as CMB Foreground," arXiv:astro-ph/9902201. 19, 79

[94] C. Bennett *et al.* [WMAP Collaboration], "First Year Wilkinson Microwave Anisotropy Probe (WMAP) Observations: Foreground Emission," Astrophys. J. Suppl. **148**, 97 (2003) [arXiv:astro-ph/0302208]. vi, 19, 20

[95] A. de Oliveira-Costa, M. Tegmark, B. M. Gaensler, J. Jonas, T. L. Landecker and P. Reich, "A model of diffuse Galactic Radio Emission from 10 MHz to 100 GHz," arXiv:0802.1525 [astro-ph]. 20

[96] D. P. Finkbeiner, "WMAP microwave emission interpreted as dark matter annihilation in the inner Galaxy," arXiv:astro-ph/0409027. 20, 21

[97] D. P. Finkbeiner, "Microwave ISM Emission Observed by WMAP," Astrophys. J. **614**, 186 (2004) [arXiv:astro-ph/0311547]. 20

[98] D. P. Finkbeiner, G. I. Langston and A. H. Minter, "Microwave ISM Emission in the Green Bank Galactic Plane Survey: Evidence for Spinning Dust," Astrophys. J. **617**, 350 (2004) [arXiv:astro-ph/0408292]. 20

[99] D. T. Cumberbatch, J. Zuntz, H. K. K. Eriksen and J. Silk, "Can the WMAP Haze really be a signature of annihilating neutralino dark matter?," arXiv:0902.0039 [astro-ph.GA]. 21

[100] http://www.lofar.org 21, 105

[101] C. A. Jackson, "Deep Radio Continuum Studies with the SKA: Evolution of Radio AGN Populations," New Astron. Rev. **48**, 1187 (2004) [arXiv:astro-ph/0409180]. 21, 85, 105

[102] Third Orbiting Solar Observatory, http://heasarc.gsfc.nasa.gov/docs/heasarc/missions/oso3.htm 22

[103] The second Small Astronomy Satellite, http://heasarc.gsfc.nasa.gov/docs/sas2/sas2.html. 22

[104] COS-B, http://sci.esa.int/science-e/www/area/index.cfm?fareaid=34. 22

[105] http://heasarc.gsfc.nasa.gov/docs/cgro/cgro.html. 22

[106] Aharonian F. A., "Very High Energy Cosmic Gamma radiation", World Scientific Publishing Co., Singapore, (2004). 22

[107] K. S. Cheng and G. E. Romero, editors, "Cosmic Gamma-Ray Sources", volume 304 of Astrophysics and Space Science Library, Oct.2004. 23

[108] T. C. Weekes, "Very high energy gamma-ray astronomy", 2003. 23

[109] E. Lorenz [MAGIC Collaboration], "Status of the 17-m MAGIC telescope," New Astron. Rev. **48** (2004) 339. 24

[110] J. A. Hinton [The HESS Collaboration], "The status of the HESS project," New Astron. Rev. **48**, 331 (2004) [arXiv:astro-ph/0403052]. 24

[111] T. C. Weekes *et al.*, "VERITAS: the Very Energetic Radiation Imaging Telescope Array System," Astropart. Phys. **17**, 221 (2002) [arXiv:astro-ph/0108478]. 24

[112] R. Enomoto *et al.* [CANGAROO Collaboration], "Design study of CANGAROO-III, stereoscopic imaging atmospheric Cherenkov telescopes for sub-TeV gamma-ray detection," Astropart. Phys. **16**, 235 (2002) [arXiv:astro-ph/0107578]. 24

[113] M. Tavani *et al.*, "The AGILE Mission," Astron. Astrophys. **502**, 995 (2009) [arXiv:0807.4254 [astro-ph]]. 24

[114] Gehrels N. and Michelson P., "GLAST: the next-generation high energy gamma-ray astronomy mission", Astropart. Phys. **11**, 277 (1999). 24

[115] W. B. Atwood *et al.* [LAT Collaboration], "The Large Area Telescope on the Fermi Gamma-ray Space Telescope Mission," Astrophys. J. **697**, 1071 (2009) [arXiv:0902.1089 [astro-ph.IM]]. 24

[116] A. A. Abdo *et al.* [Fermi LAT Collaboration], "Fermi Large Area Telescope Measurements of the Diffuse Gamma-Ray Emission at Intermediate Galactic Latitudes," Phys. Rev. Lett. **103**, 251101 (2009) [arXiv:0912.0973 [astro-ph.HE]]. 25

[117] P. Sreekumar *et al.* [EGRET Collaboration], "EGRET observations of the extragalactic gamma ray emission," Astrophys. J. **494**, 523 (1998) [arXiv:astro-ph/9709257]. vi, 25, 26, 77

[118] A. W. Strong, I. V. Moskalenko and O. Reimer, "A new determination of the extragalactic diffuse gamma-ray background from EGRET data," Astrophys. J. **613**, 956 (2004) [arXiv:astro-ph/0405441]. vi, 25, 26, 77

[119] A. A. Abdo *et al.* [The Fermi-LAT collaboration], "The Spectrum of the Isotropic Diffuse Gamma-Ray Emission Derived From First-Year Fermi Large Area Telescope Data," Phys. Rev. Lett. **104**, 101101 (2010) [arXiv:1002.3603 [astro-ph.HE]]. vi, 25, 26

[120] T. L. Collaboration, "Fermi Large Area Telescope First Source Catalog," Astrophys. J. Suppl. **188**, 405 (2010) [arXiv:1002.2280 [astro-ph.HE]]. vi, 26

[121] Gast, H., Olzem, J. and Schael, S., "Indirect dark matter search: Cosmic positron fraction measurement from 1 GeV to 50 GeV with AMS-01", Proc. XLIst Rencontres de Moriond, Electroweak Interactions and Unified Theories, 421-428 (2006). vi, 27

[122] Muller, D. and K. K. Tang, K. K., "Cosmic-ray positrons from 10 to 20 GeV - A balloon-borne measurement using the geomagnetic east-west asymmetry", Astrophys. J. **312**, 183-194 (1987). vi, 27

[123] Golden, R. L. et al. , "Observations of cosmic-ray electrons and positrons using an imaging calorimeter," Astrophys. J. **436**, 769-775 (1994). vi, 27

[124] S. W. Barwick *et al.* [HEAT Collaboration], "Measurements of the cosmic-ray positron fraction from 1-GeV to 50-GeV," Astrophys. J. **482**, L191 (1997) [arXiv:astro-ph/9703192]. vi, 27, 77

[125] Boezio, M. et al., "The cosmic-ray electron and positron spectra measured at 1 AU during solar minimum activity", Astrophys. J. **532**, 653-669 (2000). vi, 27

[126] Alcaraz, J. et al., "Leptons in near earth orbit", Phys. Lett. B **484**, 10-22 (2000). vi, 27

[127] J. J. Beatty *et al.*, "New measurement of the cosmic-ray positron fraction from 5-GeV to 15-GeV," Phys. Rev. Lett. **93**, 241102 (2004) [arXiv:astro-ph/0412230]. vi, 27

[128] Clem, J. and Evenson, P. , "Cosmic ray positron fraction observations during the A-magnetic solar minimum", Proc. 30th ICRC, Merida (2007). vi, 27

[129] M. Boezio *et al.* [WiZard/CAPRICE Collaboration], "The cosmic-ray anti-proton flux between 3-GeV and 49-GeV," Astrophys. J. **561**, 787 (2001) [arXiv:astro-ph/0103513]. vi, 27, 28

[130] A. S. Beach *et al.*, "Measurement of the cosmic-ray antiproton to proton abundance ratio between 4-GeV and 50-GeV," Phys. Rev. Lett. **87**, 271101 (2001) [arXiv:astro-ph/0111094]. vi, 27, 28

[131] M. Hof *et al.*, "Measurement of cosmic-ray antiprotons from 3.7-GeV to 19-GeV," Astrophys. J. **467**, L33 (1996). vi, 27, 28

[132] J. W. Mitchell *et al.*, "Measurement of 0.25-GeV to 3.2-GeV anti-protons in the cosmic radiation," Phys. Rev. Lett. **76**, 3057 (1996). vi, 28

[133] M. Boezio *et al.* [WIZARD Collaboration], "The cosmic-ray antiproton flux between 0.62-GeV and 3.19-GeV measured near solar minimum activity," Astrophys. J. **487**, 415 (1997). vi, 28

[134] Y. Asaoka *et al.*, "Measurements of cosmic-ray low-energy antiproton and proton spectra in a transient period of the solar field reversal," Phys. Rev. Lett. **88**, 051101 (2002) [arXiv:astro-ph/0109007]. vi, 28

[135] T. Hams et al., in Proc. 30th Int. Cosmic Ray Conf. (Merida). vi, 28

[136] S. Torii *et al.* [PPB-BETS Collaboration], "High-energy electron observations by PPB-BETS flight in Antarctica," arXiv:0809.0760 [astro-ph]. 28

[137] H. Yuksel, M. D. Kistler and T. Stanev, "TeV Gamma Rays from Geminga and the Origin of the GeV Positron Excess," arXiv:0810.2784 [astro-ph]. 28

[138] T. Kobayashi, Y. Komori, K. Yoshida and J. Nishimura, "The most likely sources of high energy cosmic-ray electrons in supernova remnants," Astrophys. J. **601**, 340 (2004) [arXiv:astro-ph/0308470]. 28

[139] I. Cholis, L. Goodenough and N. Weiner, "High Energy Positrons and the WMAP Haze from Exciting Dark Matter," arXiv:0802.2922 [astro-ph]. 28

[140] I. Cholis, L. Goodenough, D. Hooper, M. Simet and N. Weiner, "High Energy Positrons From Annihilating Dark Matter," arXiv:0809.1683 [hep-ph]. 28

[141] N. Arkani-Hamed, D. P. Finkbeiner, T. Slatyer and N. Weiner, "A Theory of Dark Matter," Phys. Rev. D **79**, 015014 (2009) [arXiv:0810.0713 [hep-ph]]. 28

[142] P. f. Yin, Q. Yuan, J. Liu, J. Zhang, X. j. Bi and S. h. Zhu, "PAMELA data and leptonically decaying dark matter," Phys. Rev. D **79**, 023512 (2009) [arXiv:0811.0176 [hep-ph]]. 28

[143] K. Hamaguchi, E. Nakamura, S. Shirai and T. T. Yanagida, "Decaying Dark Matter Baryons in a Composite Messenger Model," arXiv:0811.0737 [hep-ph]. 28

[144] C. R. Chen, K. Hamaguchi, M. M. Nojiri, F. Takahashi and S. Torii, "Dark Matter Model Selection and the ATIC/PPB-BETS anomaly," arXiv:0812.4200 [astro-ph]. 28

[145] J. Zhang, X. J. Bi, J. Liu, S. M. Liu, P. f. Yin, Q. Yuan and S. H. Zhu, "Discriminate different scenarios to account for the PAMELA and ATIC data by synchrotron and IC radiation," arXiv:0812.0522 [astro-ph]. 28

[146] V. Barger, W. Y. Keung, D. Marfatia and G. Shaughnessy, "PAMELA and dark matter," arXiv:0809.0162 [hep-ph].

[147] R. Harnik and G. D. Kribs, "An Effective Theory of Dirac Dark Matter," arXiv:0810.5557 [hep-ph]. 28

[148] A. E. Nelson and C. Spitzer, "Slightly Non-Minimal Dark Matter in PAMELA and ATIC," arXiv:0810.5167 [hep-ph]. 28

28

[149] H. Yuksel, S. Horiuchi, J. F. Beacom and S. Ando, "Neutrino Constraints on the Dark Matter Total Annihilation Cross Section," Phys. Rev. D **76**, 123506 (2007) [arXiv:0707.0196 [astro-ph]]. 104

[150] G. D. Mack, T. D. Jacques, J. F. Beacom, N. F. Bell and H. Yuksel, "Conservative Constraints on Dark Matter Annihilation into Gamma Rays," arXiv:0803.0157 [astro-ph]. 104

[151] L. Bergstrom, T. Bringmann and J. Edsjo, "New Positron Spectral Features from Supersymmetric Dark Matter - a Way to Explain the PAMELA Data?," Phys. Rev. D **78** (2008) 103520 [arXiv:0808.3725 [astro-ph]]. 28, 66

[152] M. Cirelli, M. Kadastik, M. Raidal and A. Strumia, "Model-independent implications of the e+, e-, anti-proton cosmic ray spectra on properties of Dark Matter," Nucl. Phys. B **813**, 1 (2009) [arXiv:0809.2409 [hep-ph]]. 28, 92

[153] Ginzburg V. L. and S. I. Syrovatskii, Proiskhozhdenie kosmicheskikh luchei (The Origin of Cosmic Rays), Moscow, USSR Academy of Sciences, 1963, (Pergamon), 1964 29

[154] R. Schlickeiser, *Cosmic Ray Astrophysics* (2002) (Berlin: Springer) 29

[155] D. Maurin, R. Taillet, F. Donato, P. Salati, A. Barrau and G. Boudoul, "Galactic cosmic ray nuclei as a tool for astroparticle physics," arXiv:astro-ph/0212111. vi, 30

[156] D. Maurin, F. Donato, R. Taillet and P. Salati, "Cosmic Rays below Z=30 in a diffusion model: new constraints on propagation parameters," Astrophys. J. **555**, 585 (2001) [arXiv:astro-ph/0101231]. 30, 37

[157] Seo, E. S. and Ptuskin, V. S., "Stochastic reacceleration of cosmic rays in the interstellar medium," Astrophys. J. **431**, 705S (1994) 30

[158] D. Maurin, R. Taillet and F. Donato, "New results on source and diffusion spectral features of Galactic cosmic rays: I- B/C ratio," Astron. Astrophys. **394**, 1039 (2002) [arXiv:astro-ph/0206286]. 31

[159] A. W. Strong and I. V. Moskalenko, "Propagation of cosmic-ray nucleons in the Galaxy," Astrophys. J. **509**, 212 (1998) [arXiv:astro-ph/9807150]. vi, 31, 36, 44, 56, 92

[160] F. Donato, D. Maurin, P. Salati, A. Barrau, G. Boudoul and R. Taillet, "Antiprotons from spallation of cosmic rays on interstellar matter," Astrophys. J. **563**, 172 (2001) [arXiv:astro-ph/0103150]. 31

[161] F. Donato, N. Fornengo, D. Maurin and P. Salati, "Antiprotons in cosmic rays from neutralino annihilation," Phys. Rev. D **69**, 063501 (2004) [arXiv:astro-ph/0306207]. 31, 56

[162] G. Di Bernardo, C. Evoli, D. Gaggero, D. Grasso and L. Maccione, "Unified interpretation of cosmic-ray nuclei and antiproton recent measurements," arXiv:0909.4548 [astro-ph.HE]. 31

[163] I. Gebauer, "Uncertainties of the antiproton flux from Dark Matter annihilation in comparison to the EGRET excess of diffuse gamma rays," arXiv:0710.4966 [astro-ph]. 31

[164] I. Gebauer, "Dark Matter Annihilation in the light of EGRET, HEAT, WMAP, INTEGRAL and ROSAT," arXiv:0811.2767 [astro-ph]. 31

[165] W. de Boer, "Indirect Dark Matter Signals from EGRET and PAMELA compared," arXiv:0901.2941 [hep-ph]. 31

[166] E. A. Baltz and J. Edsjo, "Positron propagation and fluxes from neutralino annihilation in the halo," Phys. Rev. D **59**, 023511 (1999) [arXiv:astro-ph/9808243]. 32, 40, 51

[167] Rand, R. J., & Lyne, A. G., "New Rotation Measures of Distant Pulsars in the Inner Galaxy and Magnetic Field Reversals," Mon. Not. Roy. Astron. Soc. **268**, 497R (1994). 33

[168] J. L. Han, R. N. Manchester, A. G. Lyne, G. J. Qiao and W. van Straten, "Pulsar rotation measures and the large-scale structure of Galactic magnetic field," Astrophys. J. **642**, 868 (2006) [arXiv:astro-ph/0601357]. 33

[169] Heiles, C., Koo, B.-C., Levenson, N. A., & Reach, W. T., "Radio Recombination Lines from Inner Galaxy Diffuse Gas. I. High-Sensitivity Observations: He +/H + and Carbon," Astrophys. J. **462**, 326 (1996). 33, 34

[170] Mathewson, D. S., & Ford, V. L. 1970, "Polarization observations of 1800 stars," Mem. R. Astron. Soc. **74**, 139 (1970). 33

[171] A. W. Strong, I. V. Moskalenko and O. Reimer, "Diffuse continuum gamma rays from the Galaxy," Astrophys. J. **537**, 763 (2000) [Erratum-ibid. **541**, 1109 (2000)] [arXiv:astro-ph/9811296]. 34, 57, 62

[172] F. Melia, Astrophys. J. **387**, L25. 34, 57

[173] Gordon, M. A., & Burton, W. B., "Carbon monoxide in the Galaxy. I - The radial distribution of CO, H2, and nucleons," Astrophys. J. **208**, 346 (1976) 35

[174] Cox, P., Krügel, E., & Mezger, P. G., "Principal heating sources of dust in the galactic disk," Astron. Astrophys. **115**, 380 (1986) 35

[175] Bronfman, L., et al. "A CO survey of the southern Milky Way - The mean radial distribution of molecular clouds within the solar circle," Astrophys. J. **324**, 248 (1988) 35

[176] Cordes, J. M., et al., "The Galactic distribution of free electrons," 1991, Nature, **354**, 121 35

[177] Reynolds, R. J., "The column density and scale height of free electrons in the galactic disk," Astrophys. J. **339**, L29 (1989) 35

[178] Grevesse, N., Noels, A. & Sauval A. J. 1996, in ASP Conf. Ser 99, "Cosmic Abundances," ed. S. S. Holt & G. Sonneborn (San Francisco: ASP), 117 35

[179] T. Delahaye, F. Donato, N. Fornengo, J. Lavalle, R. Lineros, P. Salati and R. Taillet, "Galactic secondary positron flux at the Earth," arXiv:0809.5268 [astro-ph]. 37, 91

[180] T. Delahaye, J. Lavalle, R. Lineros, F. Donato and N. Fornengo, "Galactic electrons and positrons at the Earth:new estimate of the primary and secondary fluxes," arXiv:1002.1910 [astro-ph.HE]. 37, 92

[181] T. Delahaye, R. Lineros, F. Donato, N. Fornengo and P. Salati, "Positrons from dark matter annihilation in the galactic halo: theoretical uncertainties," Phys. Rev. D **77**, 063527 (2008) [arXiv:0712.2312 [astro-ph]]. 37

[182] Haslam, C. G. T., Salter, C. J., Stoffel, H., & Wilson, W. E. "A 408 MHz all-sky continuum survey. II - The atlas of contour maps," Astron. Astrophys.S. **47**, 1 (1982) vi, 39, 45

[183] Reich, P.,Testori, J. C and Reich, W., "A radio continuum survey of the southern sky at 1420 MHz. The atlas of contour maps," Astron. Astrophys.S. **376**, 861 (2001) vi, 39, 45

[184] A. de Oliveira-Costa and M. Tegmark, "CMB multipole measurements in the presence of foregrounds," Phys. Rev. D **74**, 023005 (2006) [arXiv:astro-ph/0603369]. vi, 39, 45

[185] J. J. Connell, Astrophys. J. Lett. **501**, L59 (1998). 40

[186] I. V. Moskalenko and A. W. Strong, "Production and propagation of cosmic-ray positrons and electrons," Astrophys. J. **493**, 694 (1998) [arXiv:astro-ph/9710124]. 40, 44, 51

[187] A. Ibarra and D. Tran, "Antimatter Signatures of Gravitino Dark Matter Decay," JCAP **0807**, 002 (2008) [arXiv:0804.4596 [astro-ph]]. 40

[188] G. Ghisellini, P. W. Guilbert, R. Svensson, "The synchrotron boiler," Astrophys. J. **334**, L5-L8 (1988). 41

[189] Rybicki G.B., Lightman A.P., Radiative Processes in Astrophysics, 1979, John Wiley & Sons. 42, 74

[190] O. Petruk, "Approximation for radiation power of electrons due to inverse-Compton process in the black-body photon field," arXiv:0807.1969 [astro-ph]. 42

[191] E. Borriello, A. Cuoco and G. Miele, "Radio constraints on dark matter annihilation in the galactic halo and its substructures," Phys. Rev. D **79**, 023518 (2009) [arXiv:0809.2990 [astro-ph]]. 45

[192] K. Ishiwata, S. Matsumoto and T. Moroi, "Cosmic Gamma-ray from Inverse Compton Process in Unstable Dark Matter Scenario," Phys. Lett. B **679** (2009) 1 [arXiv:0905.4593 [astro-ph.CO]]; 54, 55

[193] A. Ibarra, D. Tran and C. Weniger, "Detecting Gamma-Ray Anisotropies from Decaying Dark Matter: Prospects for Fermi LAT," arXiv:0909.3514 [hep-ph]. 54, 55, 57

[194] M. Cirelli and P. Panci, "Inverse Compton constraints on the Dark Matter e+e- excesses," Nucl. Phys. B **821** (2009) 399 [arXiv:0904.3830 [astro-ph.CO]]; 54, 92

[195] S. Profumo and T. E. Jeltema, "Extragalactic Inverse Compton Light from Dark Matter Annihilation and the Pamela Positron Excess," JCAP **0907** (2009) 020 [arXiv:0906.0001 [astro-ph.CO]]. 54, 55

[196] G. R. Blumenthal and R. J. Gould, Reviews of Modern Physics **42**, 237 (1970). 54

[197] F. W. Stecker, M. A. Malkan and S. T. Scully, "Intergalactic Photon Spectra from the Far IR to the UV Lyman Limit for $0 < z < 6$ and the Optical Depth of the Universe to High Energy Gamma-Rays," Astrophys. J. **648** (2006) 774 [arXiv:astro-ph/0510449]; 55

[198] S. Di Falco [AMS-02 Collaboration], "Indirect dark matter search with AMS-02," arXiv:astro-ph/0607100. 56, 104

[199] L. Pieri, J. Lavalle, G. Bertone and E. Branchini, "Implications of High-Resolution Simulations on Indirect Dark Matter Searches," arXiv:0908.0195 [astro-ph.HE]. 56

[200] Heiles, Carl, "The Local Direction and Curvature of the Galactic Magnetic Field Derived from Starlight Polarization", Astrophys. J. **462**, 316 (1996). 57, 104

[201] Talk by M. Ackermann at FERMI Symposium Oct 2009. 57, 59, 69

[202] M. Papucci and A. Strumia, "Robust implications on Dark Matter from the first FERMI sky gamma map," arXiv:0912.0742 [hep-ph]. 58, 66, 68

[203] J. Redondo and M. Postma, "Massive hidden photons as lukewarm dark matter," JCAP **0902**, 005 (2009) [arXiv:0811.0326 [hep-ph]]. 64

[204] E. Nardi, F. Sannino and A. Strumia, "Decaying Dark Matter can explain the electron/positron excesses," JCAP **0901**, 043 (2009) [arXiv:0811.4153 [hep-ph]]. 64

[205] A. Ibarra and D. Tran, "Decaying Dark Matter and the PAMELA Anomaly," JCAP **0902**, 021 (2009) [arXiv:0811.1555 [hep-ph]]. 64

[206] B. Holdom, "Two U(1)'S And Epsilon Charge Shifts," Phys. Lett. B **166**, 196 (1986). 64

[207] K. R. Dienes, C. F. Kolda and J. March-Russell, "Kinetic mixing and the supersymmetric gauge hierarchy," Nucl. Phys. B **492**, 104 (1997) [arXiv:hep-ph/9610479]. 64

[208] S. A. Abel and B. W. Schofield, "Brane-antibrane kinetic mixing, millicharged particles and SUSY breaking," Nucl. Phys. B **685**, 150 (2004) [arXiv:hep-th/0311051]. 64

[209] S. A. Abel, J. Jaeckel, V. V. Khoze and A. Ringwald, "Illuminating the hidden sector of string theory by shining light through a magnetic field," Phys. Lett. B **666**, 66 (2008) [arXiv:hep-ph/0608248]. 64

[210] S. A. Abel, M. D. Goodsell, J. Jaeckel, V. V. Khoze and A. Ringwald, "Kinetic Mixing of the Photon with Hidden U(1)s in String Phenomenology," JHEP **0807**, 124 (2008) [arXiv:0803.1449 [hep-ph]]. 64

[211] F. Takayama and M. Yamaguchi, "Gravitino dark matter without R-parity," Phys. Lett. B **485**, 388 (2000) [arXiv:hep-ph/0005214]. 64

[212] A. Ibarra, A. Ringwald and C. Weniger, "Hidden gauginos of an unbroken U(1): Cosmological constraints and phenomenological prospects," JCAP **0901**, 003 (2009) [arXiv:0809.3196 [hep-ph]]. 65

[213] T. Sjostrand, S. Mrenna and P. Skands, "PYTHIA 6.4 Physics and Manual," JHEP **0605**, 026 (2006) [arXiv:hep-ph/0603175]. 65

[214] S. Shirai, F. Takahashi and T. T. Yanagida, "Decaying Hidden Gaugino as a Source of PAMELA/ATIC Anomalies," arXiv:0902.4770 [hep-ph]. 66

[215] A. Arvanitaki, S. Dimopoulos, S. Dubovsky, P. W. Graham, R. Harnik and S. Rajendran, "Decaying Dark Matter as a Probe of Unification and TeV Spectroscopy," arXiv:0904.2789 [hep-ph]. 66

[216] K. Ishiwata, S. Matsumoto and T. Moroi, "High Energy Cosmic Rays from Decaying Supersymmetric Dark Matter," arXiv:0903.0242 [hep-ph]. 66

[217] S. Shirai, F. Takahashi and T. T. Yanagida, "R-violating Decay of Wino Dark Matter and electron/positron Excesses in the PAMELA/Fermi Experiments," arXiv:0905.0388 [hep-ph]. 66

[218] S. L. Chen, R. N. Mohapatra, S. Nussinov and Y. Zhang, "R-Parity Breaking via Type II Seesaw, Decaying Gravitino Dark Matter and PAMELA Positron Excess," arXiv:0903.2562 [hep-ph]. 66

[219] L. Bergstrom, T. Bringmann, M. Eriksson and M. Gustafsson, "Gamma rays from Kaluza-Klein dark matter," Phys. Rev. Lett. **94** (2005) 131301 [arXiv:astro-ph/0410359]. 66

[220] C. R. Chen, S. K. Mandal and F. Takahashi, "Gamma-ray Constraints on Hadronic and Leptonic Activities of Decaying Dark Matter," arXiv:0910.2639 [hep-ph]. 66

[221] M. Cirelli, P. Panci and P. D. Serpico, "Diffuse gamma ray constraints on annihilating or decaying Dark Matter after Fermi," arXiv:0912.0663 [astro-ph.CO]. 66, 69

[222] T. Sjostrand, P. Eden, C. Friberg, L. Lonnblad, G. Miu, S. Mrenna and E. Norrbin, "High-energy physics event generation with PYTHIA 6.1," Comput. Phys. Commun. **135**, 238 (2001) [arXiv:hep-ph/0010017]. 66

[223] D. Grasso *et al.* [FERMI-LAT Collaboration], "On possible interpretations of the high energy electron-positron spectrum measured by the Fermi Large Area Telescope," Astropart. Phys. **32** (2009) 140 [arXiv:0905.0636 [astro-ph.HE]]. 67

[224] A. Ibarra, D. Tran and C. Weniger, "Decaying Dark Matter in Light of the PAMELA and Fermi LAT Data," arXiv:0906.1571 [hep-ph]. ix, 68

[225] S. Ando, E. Komatsu, T. Narumoto and T. Totani, "Dark matter annihilation or unresolved astrophysical sources? Anisotropy probe of the origin of cosmic gamma-ray background," Phys. Rev. D **75**, 063519 (2007) [arXiv:astro-ph/0612467]. 72

[226] H. J. Mo, Y. P. Jing and S. D. M. White, "The Correlation Function of Clusters of Galaxies and the Amplitude of Mass Fluctuations in the Universe," Mon. Not. Roy. Astron. Soc. **282**, 1096 (1996) [arXiv:astro-ph/9602052]. 73

[227] Kaiser, N., Astrophys. J. **388**, 272 (1992) 75

[228] S. Ando and E. Komatsu, "Anisotropy of the cosmic gamma-ray background from dark matter Phys. Rev. D **73**, 023521 (2006) [arXiv:astro-ph/0512217]. 76

[229] S. Hofmann, D. J. Schwarz and H. Stoecker, "Damping scales of neutralino cold dark matter," Phys. Rev. D **64**, 083507 (2001). 77

[230] P. P. Kronberg, "Extragalactic magnetic fields," Rept. Prog. Phys. **57**, 325 (1994). 77

[231] G. Tormen, A. Diaferio and D. Syer, Mon. Not. Roy. Astron. Soc. **299**, 728 (1998). 77

[232] A. A. Klypin, S. Gottlober and A. V. Kravtsov, "Galaxies in N-body Simulations: overcoming the overmerging problem," Astrophys. J. **516**, 530 (1999). 77

[233] S. Ghigna, B. Moore, F. Governato, G. Lake, T. Quinn and J. Stadel, "Density profiles and substructure of dark matter halos: converging results at ultra-high numerical resolution," Astrophys. J. **544**, 616 (2000). 77

[234] V. Springel, S. D. M. White, G. Tormen and G. Kauffmann, "Populating a cluster of galaxies - I. Results at z=0," Mon. Not. Roy. Astron. Soc. **328**, 726 (2001). 77

[235] G. De Lucia *et al.*, "Substructures in Cold Dark Matter Halos," Mon. Not. Roy. Astron. Soc. **348**, 333 (2004). 77

[236] L. Shaw, J. Weller, J. P. Ostriker and P. Bode, "Statistics of physical properties of dark matter clusters," Astrophys. J. **646**, 815 (2006). 77

[237] A. Helmi, S. D. M. White and V. Springel, "The phase-space structure of a dark-matter halo: Implications for dark-matter direct detection experiments," Phys. Rev. D **66**, 063502 (2002). 77

[238] X. J. Bi, "Gamma rays from the neutralino dark matter annihilations in the Milky Way substructures," Nucl. Phys. B **741**, 83 (2006) [arXiv:astro-ph/0510714]. 77

[239] Q. Yuan and X. J. Bi, "The Galactic positron flux and dark matter substructures," JCAP **0705**, 001 (2007) [arXiv:astro-ph/0611872]. 77

[240] J. Lavalle, Q. Yuan, D. Maurin and X. J. Bi, "Full Calculation of Clumpiness Boost factors for Antimatter Cosmic Rays in the light of ΛCDM N-body simulation results," arXiv:0709.3634 [astro-ph]. 77

[241] S. Coutu *et al.*, "Positron Measurements With The Heat-Pbar Instrument," *Prepared for 27th International Cosmic Ray Conference (ICRC 2001), Hamburg, Germany, 7-15 Aug 2001* 77

[242] R. J. Protheroe and P. L. Biermann, "A new estimate of the extragalactic radio background and implications for ultra-high-energy gamma ray propagation," Astropart. Phys. **6**, 45 (1996) [Erratum-ibid. **7**, 181 (1997)] [arXiv:astro-ph/9605119]. 78

[243] E. Waxman and A. Loeb, "Fluctuations in the Radio Background from Intergalactic Synchrotron Emission," Astrophys. J. **545**, L11 (2000) [arXiv:astro-ph/0007049]. 78, 79

[244] U. Keshet, E. Waxman and A. Loeb, "Imprint of Intergalactic Shocks on the Low-Frequency Radio Sky," Astrophys. J. **617**, 281 (2004) [arXiv:astro-ph/0402320]. ix, x, 78, 79, 86, 87

[245] J. C. Mather, D. J. Fixsen, R. A. Shafer, C. Mosier and D. T. Wilkinson, "Calibrator Design for the COBE Far Infrared Absolute Spectrophotometer (FIRAS)," Astrophys. J. **512**, 511 (1999) [arXiv:astro-ph/9810373]. 80, 109

[246] L. Spinoglio, M. A. Malkan, B. Rush, L. Carrasco and E. Recillas-Cruz, "Multiwavelength energy distributions and bolometric luminosities of the 12 micron galaxy sample," Astrophys. J. **453**, 616 (1995) [arXiv:astro-ph/9506139]. 84, 85

[247] M. Tegmark and G. Efstathiou, "A method for subtracting foregrounds from multi-frequency CMB sky maps," arXiv:astro-ph/9507009. 86

[248] M. Tegmark, D. J. Eisenstein, W. Hu and A. de Oliveira-Costa, "Foregrounds and Forecasts for the Cosmic Microwave Background," Astrophys. J. **530**, 133 (2000) [arXiv:astro-ph/9905257]. 86, 109

[249] L. La Porta, C. Burigana, W. Reich and P. Reich, "The impact of Galactic synchrotron emission on CMB anisotropy measurements. I. Angular power spectrum analysis of total intensity all-sky surveys," arXiv:0801.0547. 86

[250] G. Giardino, A. J. Banday, P. Fosalba, K. M. Gorski, J. L. Jonas, W. O'Mullane and J. Tauber, "The angular power spectrum of radio emission at 2.3 GHz," arXiv:astro-ph/0103233. 86, 109

[251] R. A. Sunyaev and Y. B. Zeldovich, "Small scale fluctuations of relic radiation," Astrophys. Space Sci. **7**, 3 (1970). 86

[252] Persi. F. M., Cen, R., Ostriker, J. P., Astrophys. J. **442**, 1 (1995) 86

[253] J. J. Condon, Ap. J. **338**, 13 (1989). x, 89

[254] D. Hooper, G. Zaharijas, D. P. Finkbeiner and G. Dobler, "Prospects For Detecting Dark Matter With GLAST In Light Of The WMAP Haze," arXiv:0709.3114 [astro-ph]. 89

[255] P. Grajek, G. Kane, D. J. Phalen, A. Pierce and S. Watson, "Neutralino Dark Matter from Indirect Detection Revisited," arXiv:0807.1508 [hep-ph]. 89

[256] T. A. Porter, I. V. Moskalenko and A. W. Strong, "Inverse Compton emission from galactic supernova remnants: Effect of the interstellar radiation field," Astrophys. J. **648**, L29 (2006) [arXiv:astro-ph/0607344]. 92

[257] K. M. Gorski, E. Hivon, A. J. Banday, B. D. Wandelt, F. K. Hansen, M. Reinecke and M. Bartelman, "HEALPix – a Framework for High Resolution Discretization, and Fast Analysis of Data Distributed on the Sphere," Astrophys. J. **622**, 759 (2005) [arXiv:astro-ph/0409513]. 92

[258] M. Perelstein and B. Shakya, "Comment on Calculation of Positron Flux from Galactic Dark Matter," arXiv:1002.4588 [astro-ph.HE]. 98

[259] X. L. Chen, "Angular power spectrum of the galactic synchrotron radiation," arXiv:astro-ph/0409733. 104

[260] S. De Lope Amigo, W. Y. Cheung, Z. Huang and S. P. Ng, "Cosmological Constraints on Decaying Dark Matter," arXiv:0812.4016 [hep-ph]. 105

[261] L. Zhang, X. L. Chen, Y. A. Lei and Z. G. Si, "The impacts of dark matter particle annihilation on recombination and the anisotropies of the cosmic microwave background," Phys. Rev. D **74**, 103519 (2006) [arXiv:astro-ph/0603425]. 105

[262] S. R. Furlanetto, S. P. Oh and E. Pierpaoli, "The Effects of Dark Matter Decay and Annihilation on the High-Redshift 21 cm Background," Phys. Rev. D **74**, 103502 (2006) [arXiv:astro-ph/0608385]. 105

[263] M. Valdes, A. Ferrara, M. Mapelli and E. Ripamonti, "Constraining DM through 21 cm observations," Mon. Not. Roy. Astron. Soc. **377**, 245 (2007) [arXiv:astro-ph/0701301]. 105

# Acknowledgements

I would like to express my deepest gratitude to Prof. Günter Sigl for encouraging me and enthusiastic supervision. He gave me the confidence and support to begin my studies. His wide knowledge and logical way of thinking have been of great value for me. I appreciate all his contributions of time, ideas, and funding to make my Ph.D. experience productive and stimulating.

My gratitude also goes to all my collaborators for lots of interesting and useful discussions. Without the particular efforts of Luca Maccione, Christoph Weniger, Javier Redondo, Francesco Miniati, most of these projects would not have come to fruition.

I also would like to express my thanks to all the other colleagues. In particular, I would like to thank Bringmann Torsten, Mirizzi Alessandro, Tomas Bayo Ricard, Kulbartz Jörg and van den Aarssen Laura for their friendship and support.

Last, but not least, I would like to thank my parents and friends for all their continuous support. To my parents, I would like to say, "I'm proud to be your son".